
Simulation of Coded Mask Imaging

Diplomarbeit aus der Physik
vorgelegt von

Mirjam Oertel

Bamberg, 11.07.2013



Dr. Karl Remeis Sternwarte Bamberg
Astronomisches Institut der
Friedrich-Alexander-Universität Erlangen-Nürnberg



Betreuer: Prof. Dr. Jörn Wilms

Contents

Zusammenfassung	1
Abstract	2
1. The difficulty of detecting high energy X-rays	3
1.1. Mechanisms of X-ray production	3
1.2. Astrophysical X-ray sources	5
1.3. Detection techniques	9
2. Coded mask systems	14
2.1. Detection principle	14
2.1.1. Characteristic quantities	15
2.1.2. Mask patterns	17
2.1.3. Position sensitive detection plane	18
2.2. Image reconstruction theory	21
2.2.1. Concepts of different methods	21
2.2.2. Balanced cross correlation	23
2.3. Former and future missions	25
3. MIRAX	27
3.1. Mission overview	27
3.2. Scientific motivation	29
3.3. Detector setup	30
4. Software simulation	32
4.1. Simulation chain	32
4.1.1. Photon generation	32
4.1.2. Imaging	35
4.1.3. Detection	37
4.1.4. Reconstruction	39
4.2. Implementation of the MIRAX-HXI	44
4.3. Results	50
5. Outlook	58
A. Overview of used functions	60
B. Example code	62
Acknowledgments	67
List of Figures	68

List of Tables	70
References	71
Declaration	73

Zusammenfassung

Die Technik des ‘Coded Mask Imaging’ bietet in der Röntgenastronomie, im Vergleich zu den herkömmlichen direkt abbildenden Techniken viele Möglichkeiten und Vorteile, vor allem im Bereich der Detektion sehr hoch energetischer Photonen. Es muss jedoch auch deutlich mehr Rechenaufwand betrieben werden, um ein Bild der beobachteten Quellverteilung zu erhalten, da die einfallenden Photonen zuerst mittels einer Maske, die aus durchlässigen und blockierenden Elementen besteht, kodiert werden und anschließend, nach dem Detektionsprozess wieder dekodiert werden müssen.

Das Hauptanliegen der vorliegenden Arbeit ist es, ein Softwarepaket vorzustellen, das die verschiedenen Schritte der Kodierung und Dekodierung eines Coded Mask Instruments simuliert und den Fokus auf die Bildrekonstruktion aus dem aufgenommenen mehrfach überlagerten Schattenwurf der Maske legt.

Um die Notwendigkeit eines solchen Algorithmus zu verdeutlichen, werden zuerst die Mechanismen, die Röntgenphotonen produzieren, diskutiert und anschließend wird ein Überblick über ihre Entstehungsgebiete im Weltall gegeben. Außerdem werden die Funktionsprinzipien von herkömmlichen Röntgenteleskopen und von Coded Mask Systemen erklärt und hinsichtlich ihrer Anwendungsgebiete verglichen.

Den Anstoß zu diesem Projekt hat die geplante brasilianische Weltraummission *LATTES* gegeben, deren Coded Mask Teleskop, der Monitor e Imageador de RAios-X, oder kurz ‘MIRAX’, im Vorfeld studiert werden soll. Das dritte Kapitel widmet sich dieser Mission und im vierten Kapitel, das die einzelnen Simulationseinheiten im Detail erläutert, befasst sich ein ganzer Unterabschnitt mit der Integration dieses speziellen Instruments in die Simulation. Es werden erste Eindrücke dessen vermittelt, was MIRAX beobachten wird und das Prinzip der Bildrekonstruktion wird genau analysiert.

Die dargestellte Simulationssoftware dient als Grundlage für die Entwicklung einer ausgefeilteren Bildrekonstruktion und für die Integration eines passgenaueren Modells des MIRAX Teleskops. Die nötigen Verbesserungen und nächsten Schritte werden im letzten Kapitel vorgestellt.

Abstract

Coded mask imaging is a technique providing vast possibilities and advantages in X-ray astronomy, compared to direct imaging telescopes, when dealing with high energy photons. But it also requires some extra computational effort to obtain a sky image, since it encodes the infalling photons with a mask pattern, made up of transparent and opaque elements and therefore involves an appropriate decoding process after the detection.

The subject of this thesis is to present a software simulation package, which realizes the different steps in the encoding and decoding procedure of coded mask imaging and which focuses on the process of reconstructing a sky image from the detected shadowgram.

In order to motivate the necessity of such an algorithm, first the mechanisms that create X-ray photons are discussed, and then the environments, they can be found in space are overviewed. Further, conventional X-ray telescopes as well as the principle of coded mask imaging are explained, and their fields of application are compared.

The initiation to this project arose from the upcoming Brazilian space mission *LATTES*, whose coded mask telescope, the Monitor e Imageador de RAios-X or ‘MIRAX’ shall be studied in advance. The third chapter is dedicated to that mission, and in the fourth chapter, which describes the simulation pipeline in detail, a whole section explains the implementation of that specific instrument. First impressions, of what MIRAX will be able to see, are given and the image reconstruction module is analyzed explicitly.

The presented simulation software serves as basis for developing a more sophisticated image reconstruction and for implementing a more elaborate setup of the MIRAX telescope. The suggested improvements and next steps are outlined in the last chapter.

Chapter 1

The difficulty of detecting high energy X-rays

With the beginning of X-ray astronomy in the early 1960s a new window to the investigation of various phenomena in our Universe has been opened. Until then the Sun was the only known extraterrestrial X-ray source, but it should not sit in that lonely position for much longer. In 1962, with the launch of an Aerobee rocket payloaded with Geiger counters, the first extraterrestrial X-ray source Scorpius X-1 was discovered (Giacconi et al., 1962) and several other missions should follow soon. During the 1970s X-ray astronomy developed at a fast pace using balloon-borne experiments as well as satellites. As technology advanced, new methods for detecting X-ray sources were developed, and existing ones were improved, leading to ~ 1 million¹ discovered sources until today which means both, a lot of question marks addressing astrophysical processes disappeared and a lot of new ones were set.

The following sections explain the mechanisms behind cosmic X-ray generation and give an overview of the environments X-rays originate from and the methods used to detect them.

1.1. Mechanisms of X-ray production

X-rays belong to the short wavelength or high energy domain of the electromagnetic spectrum, ranging from $\lambda \sim 10$ to 0.01 nm or $E \sim 0.1$ to 100 keV. They are divided into the so called soft ($E \lesssim 10$ keV) and hard X-ray part ($E \gtrsim 10$ keV) referring to their increase in energy (Kartunnen et al., 2000).

The mechanisms that lead to the release of cosmic X-rays can roughly be sorted into two categories due to the type of binding that the involved electrons experience. These are either free or bound to their atoms².

Excitation

For environments where electrons appear in bound systems the only way to produce X-ray emission is to excite them from their ground state to a more energetic ‘excited’ state. Since electrons can only occupy certain discrete energy levels³ depending on the element under consideration, excitation can only occur if the electron gains at least the minimum amount

¹from: http://heasarc.gsfc.nasa.gov/docs/heasarc/headates/how_many_xray.html

²see: http://imagine.gsfc.nasa.gov/docs/science/how_12/xray_generation_el.html

³see quantum mechanics textbook such as: Nolting (2004) or Cohen-Tannoudji et al. (2007)

of energy needed to jump to a higher level by either absorption of a trespassing photon or by collision with other atoms or particles. The electron will soon fall back to its initial energy shell or the gap is filled with a electron from another shell. Either way, a photon corresponding to the energy difference between these two states will be emitted.

The fact that there are many different elements, each with different energy levels, implies that there is a large number of different possible emission lines. To emit X-rays the atom has to be big enough to generate energy gaps between initial and excited states that lie in the X-ray regime. Therefore X-ray emission starts with carbon and can often be found with elements like oxygen and iron.

Interactions due to free electrons can form X-rays in three different ways, listed below.

Inverse Compton scattering

For an electron meeting a high energetic photon the usual process goes like this: the photon transfers part of its energy to the electron producing a fast electron and a lower energetic photon. This is called Compton effect. In X-ray astronomy the inverse process is of importance, meaning a low energy photon (e.g., from the cosmic microwave background or from stars, see Sec. 1.2) scatters with a fast relativistic electron (e.g., from active galactic nuclei, see Sec. 1.2), thereby transferring energy and releasing X-ray photons (Gruppen, 2005).

Bremsstrahlung

If electrons, or charged particles in general, are accelerated or deflected in the Coulomb field of other charged particles like ions or nuclei, their acceleration causes the radiation of the so called 'bremsstrahlung', which often lies in the X-ray and γ -ray domain. Bremsstrahlung occurs for instance in hot gases because of the random thermal motion or when charged particles hit an obstacle. The probability Φ for the emission of bremsstrahlung depends on the charges of incoming (z) and hit (Z) particles, as well as the incoming particles energy E , and it decreases with the square of its mass m (Gruppen, 2005):

$$\Phi \sim \frac{z^2 Z^2 E}{m^2}. \quad (1.1)$$

That is why bremsstrahlung preferably is emitted by electrons, since their mass is very small, corresponding to a higher probability of occurrence.

Synchrotron radiation

Synchrotron radiation is much like bremsstrahlung, but with magnetic fields. The force onto charged particles in magnetic fields is always perpendicular to its direction and to the direction of motion, which causes relativistic electrons moving in a magnetic field to spiral around the field axis. That, being an accelerated motion, will emit electromagnetic waves.

The extremely high temperatures in many cosmic objects lead to a further important mechanism that generates X-rays in optically thick media⁴:

⁴Electromagnetic waves traveling through matter will decrease in intensity by $I = I_0 \cdot e^{-\alpha \Delta z}$, where α is the absorption coefficient and Δz the thickness of the layer. $\alpha \Delta z$ is called optical depth τ , and media with $\tau \gg 1$ are optically thick, those with $\tau \ll 1$ are optically thin (Demtröder, 2006). Since optically thick gases emit nearly as much radiation as they absorb, they can be approximately treated as blackbodies (Gruppen, 2005).

Blackbody radiation

A blackbody is an ideal object which absorbs radiation of all wavelengths completely. It also emits the same amount of radiation with a spectral distribution depending on its temperature and described by Planck's law (Planck, 1901; Demtröder, 2005):

$$\rho(\nu, T) = \frac{8\pi h}{c^3} \frac{\nu^3 d\nu}{e^{h\nu/(kT)} - 1}, \quad (1.2)$$

implying that the spectral radiation density ρ increases with temperature and the maximum is shifted to higher frequencies or lower wavelength. As an approximation for high frequencies ($h\nu \gg kT$) one can use Wien's displacement law to determine the position of the peak (Wien, 1896):

$$\frac{\nu_{\max}}{T} = 2.82 \frac{k}{h}. \quad (1.3)$$

The total amount of radiation emitted by a blackbody is given by Stefan Boltzmann's law:

$$S = \sigma T^4. \quad (1.4)$$

For temperatures present in the Sun's chromosphere ($T \sim 6000$ K) the emission maximum lies in the area of visible light ($\lambda_{\max} \sim 480$ nm), but for objects with temperatures above $T \sim 10^6$ K the maximum corresponds to X-ray wavelength.

In general various combinations of the mechanisms described above contribute to the X-ray spectrum of a particular source, determining its individual shape. One possibility to classify the contributing effects is, to divide them into 'thermal' and 'non-thermal' processes, where the term 'thermal' refers to electrons which follow a Maxwellian energy distribution. The most important thermal processes are continuum (bremsstrahlung) and line emission (atomic level transitions) from optical thin media and blackbody radiation from optical thick ones.

Non-thermal processes are found, e.g., with electrons occurring in beams that mainly trigger Synchrotron radiation or inverse Compton scattering (Mewe et al., 1999).

1.2. Astrophysical X-ray sources

X-ray emission can be found in nearly all astrophysical environments. Therefore this section will give a short insight to the variety of X-ray sources to emphasize the importance of conducting further research with new telescopes and satellites in this field.

In our solar system the **Sun** is the most prominent X-ray emitter. It took some other ten years since the first suggestion in 1938 that the Sun could possibly emit X-rays, till 1949, when weak X-ray emission in the hot upper layers of its atmosphere finally was confirmed. Up to the 1990s only three other such objects in the solar system were known, the Earth, the Moon and Jupiter, and it was just in recent time when it was discovered that even **planets**, **comets** and almost every other object in our nearest neighborhood is a source for X-ray emission (Leverington, 2000; Bhardwaj et al., 2007).

To present a rough categorization, one can sort all X-ray sources into galactic and extra-galactic ones, like shown in Fig. 4.26.

During star formation **normal stars** show X-ray emission mainly from accretion or magnetic coronal flares. This strong emission from pre-main sequence stars tends to decrease as

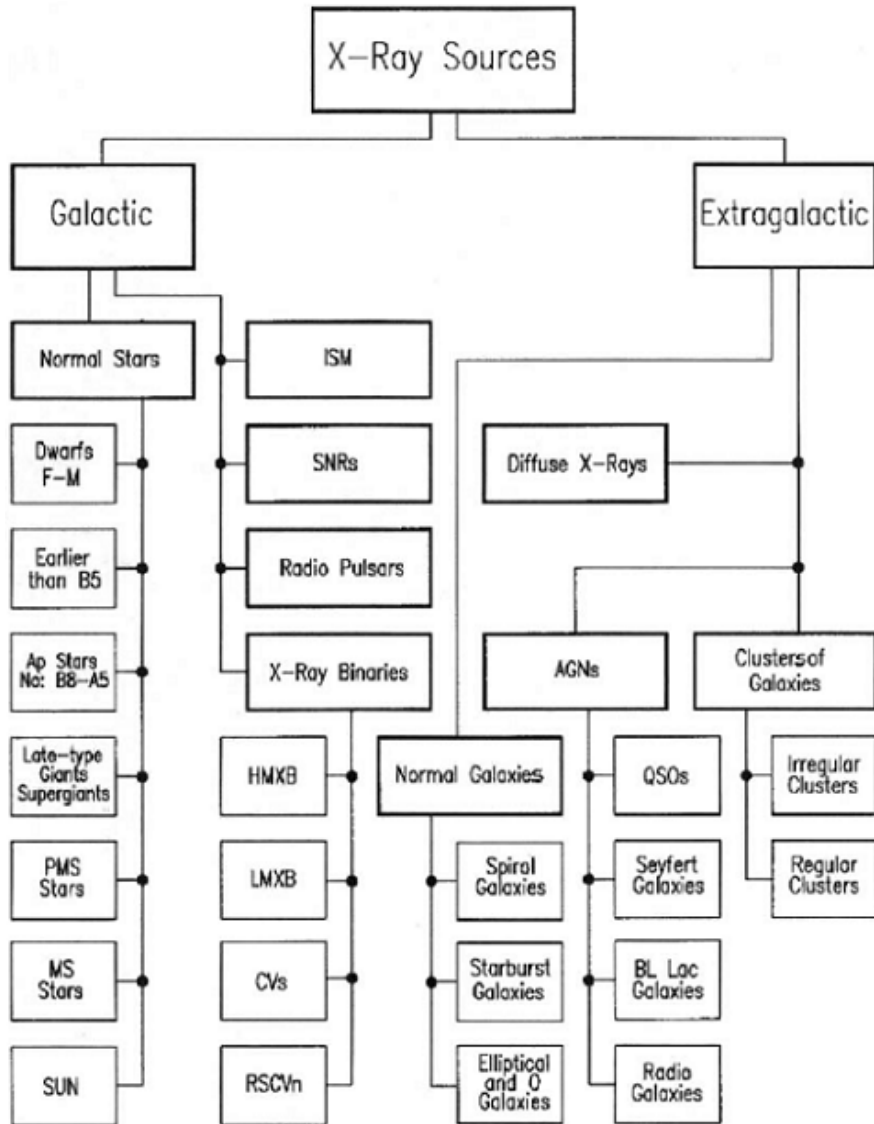


Figure 1.1: X-ray sources divided into galactic and extragalactic origin (taken from Giovannelli & Sabau-Graziati, 2004). Galactic sources contain the sub-classes normal stars, Inter-Stellar Medium (ISM), Super Nova Remnants (SNRs), radio pulsars and X-ray binaries. Extragalactic sources count main contributions from normal galaxies, galaxy-clusters, Active Galactic Nuclei (AGNs) and diffuse background emission.

the star grows older, and the star’s hot corona will persist as its main X-ray source (see Fig. 1.2). Stars that are still surrounded by a circumstellar disk, also show fluorescent emission, where fast electrons hit the weakly ionized or neutral disk material, leading to the ejection of electrons accompanied by fluorescent transitions (Giovannelli & Sabau-Graziati, 2004; Güdel & Naze, 2009).

Brown dwarfs belong to the faintest extrasolar X-ray sources and therefore had to wait until 1998 to be confirmed as X-ray emitters (Comeron et al., 1998). They are zwitter-like objects, often referred to as ‘failed stars’, with masses too low to start a nuclear reaction as a star, but also too high to be a planet. They lack a central nuclear energy source and can only produce their dim X-ray emission by a strong magnetic field, which occurs, if their convective motion is supplemented with a rapid rotation.

When a massive star has exhausted all of its fuel, it is at the end of its life and will explode as a **supernova** (SN), through a collapse of its core. It then builds a remnant (neutron star or black hole), depending on its initial mass, in a very rapid process (~ 1 sec) and blows away its outer shells by the release of a thermonuclear shock wave that also fuses lighter particles

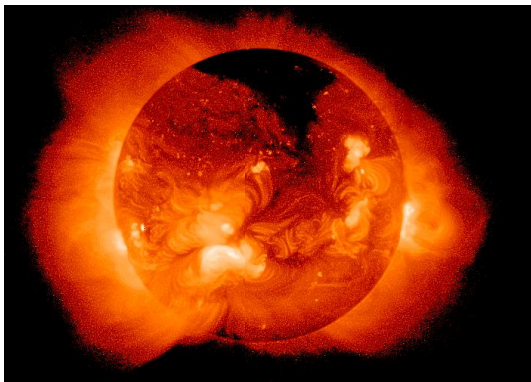


Figure 1.2: The Sun’s hot corona shows bright regions in X-rays that are mainly controlled by its magnetic field. The underlying surface only reaches temperatures of ~ 6000 K, which is not sufficient for strong X-ray emission and therefore appears to be dark (credits: http://solarscience.msfc.nasa.gov/images/Yohkoh_920508.jpg).

into heavier ones (Type II; Ib, Ic). If a white dwarf has accreted enough matter to cross the Chandrasekhar-Limit of $1.44 M_{\odot}$, it will end in a sudden thermonuclear explosion, leaving no remnant (Type Ia). In either way a shock wave will crash into the circumstellar gas, releasing X-rays due to highly accelerated charged particles.

The remnant of the SN-explosion will collapse further to form a **neutron star** (NS), if the mass crossed the Chandrasekhar-Limit (otherwise it will just leave a slowly cooling white dwarf⁵). Since the angular momentum was preserved while its radius shrank enormously, the NS will rotate very rapidly (several hundred times per second)⁶. Further, its magnetic field will become very strong due to compression during the explosion. NSs can produce ‘pulsars’, when they release very high energetic particles in a narrow beam that follows the magnetic field, and as the NS rotates, that particle cone gives off pulses like a rotating lighthouse beam (depending on the line of sight). NSs can either be powered by rotation or by accretion. The former ones produce their X-ray pulses by an outflow of high energy particles, or in the extreme case of very rapidly rotating NSs with very strong magnetic fields (10^{14} G), the so called ‘magnetars’, also by starquakes that may occur on their surfaces, producing X-ray outbursts. The latter ones belong to binary systems (see below), with X-ray emission due to strongly accelerated infalling material that concentrates on the poles and pulses in and out of view.

If the SN remnant exceeds a certain mass limit, the Oppenheimer-Volkov mass, which lies somewhere between $1.5-3 M_{\odot}$, no pressure can prevent it from collapsing to a **black hole**, an object with infinite density, which not even light can escape from. BHs in binary systems emit accretion powered X-rays that do not pulse like NSs, because the lack of regular magnetic poles, but they do somewhat flicker (Kartunnen et al., 2000).

Among the brightest X-ray sources in our galaxy one can find **binary systems**, which contain one compact object (e.g., NS or BH) and one normal companion, close to each other. Binary Systems were the first extrasolar X-ray emitters to be detected by Giacconi et al. (1962) with the famous source Scorpius X-1. Their radiation is fueled by the infalling material onto the compact star, where the particles are highly accelerated by its strong gravity. They can be sub-divided into High Mass X-ray Binaries (HMXBs), Low Mass X-ray Binaries (LMXBs) and Cataclysmic Variables (CVs). HMXBs contain a compact object and a high mass primary star⁷ ($M \gg 1 M_{\odot}$), that dominates the radiated emission. The minor

⁵White dwarfs below $1.44 M_{\odot}$ are prevented from collapsing further by classical degenerate electron pressure.

The even denser NSs resist gravity with the pressure of a relativistic degenerate neutron gas.

⁶Its rotation period will decrease over time, because the NSs’ angular momentum is going to decrease by diverse emission mechanisms.

⁷It is common to name the higher mass object in a binary system ‘primary star’.

X-ray emission is produced by stellar winds that transfer the mass between the two objects. LMXBs have a primary compact object and a low mass, late type companion ($M \ll 1 M_{\odot}$) which loses matter from its Roche-lobe⁸, transferring it through the inner Lagrangian point⁹, where it then accretes onto the compact object, following the law of conservation of angular momentum. In CVs the companion is also a low mass, late type star, but the compact object is a white dwarf. Mass transfer either happens by Roche-lobe overflow, thus also building an accretion disc, or through accretion columns at the dwarf's magnetic poles or by some intermediate form (Giovannelli & Sabau-Graziati, 1993, 2004).

On even bigger scales, whole **galaxies**, containing some hundred billion stars and loads of other gravitationally bound material, emit in the X-ray regime due to their components described above and due to extremely heated gas. If two galaxies are grazing each other or even colliding, starburst activity can be triggered. Shock waves will force dust clouds to collapse and build new stars, which will be extremely massive and hence short-living, and eventually give rise to more shock waves and star production as they end up as SNe. All those processes can be studied in X-ray wavelength and give an insight to the hot and violent past of the universe, when everything was packed more closely together.

Galaxies can be combined to **clusters**, containing at least ~ 50 individual members. They show X-ray emission from hot gas, filling the space inbetween them, which has quite likely been ejected from their galaxies into the cluster.

If a galaxy is extremely bright and of unusual activity within its inner region, it is classed among the **Active Galactic Nuclei** (AGNs). AGNs possess a super massive BH (SMBH) at their core, which releases X-rays from infalling extremely heated material, as well as jets blasting away from it. There are many different manifestations of AGNs, including the so called Quasi-Stellar Objects (QSOs or quasars). Most quasars are point-like sources with a high redshift. Thus they are very old objects with extremely large luminosities concentrated in a very small region of their host galaxy. In fact they are the most intense X-ray sources ever discovered, with some of them even visible at distances of 12 billion light years¹⁰ (Kartunnen et al., 2000; Giovannelli & Sabau-Graziati, 2004).

The **Cosmic X-ray Background** (CXB) has been a subject of discussion since its discovery in 1962 (Giacconi et al., 1962; see Fig. 1.3, left side). Following missions subsequently resolved it to emission from discrete extragalactic point sources, mainly comprised of AGNs as shown in Fig. 1.3 on the right side. In that context *ROSAT* provided a huge progress, by resolving $\sim 80\%$ of the CXB at energies around 0.5 – 2 keV into discrete sources (Hasinger et al., 1998), but harder energies had to wait for *Chandra* and *XMM-Newton* to assign $\sim 60\%$ of the 5 – 10 keV-background to distinct sources (Giacconi et al., 2002; Worsley et al., 2005).

Looking back on that quite impressive variety of all kinds of X-ray emitting sources, present during different stages in the evolution of our universe, underlines the need of advanced detector systems to study X-ray emission.

⁸A Roche-lobe is the area between the two components in a binary system, where gravity is balanced. For a LMXB the Roche-lobe lies within the companion star and for HMXB it contains the companion.

⁹Lagrange points are locations within a two body system where their combined gravitational force is of the same size as a third's body centripetal force (which is depending on its mass, velocity and orbit), which is therefore fixed in exactly that spot.

¹⁰taken from: http://chandra.harvard.edu/xray_sources/quasars.html.

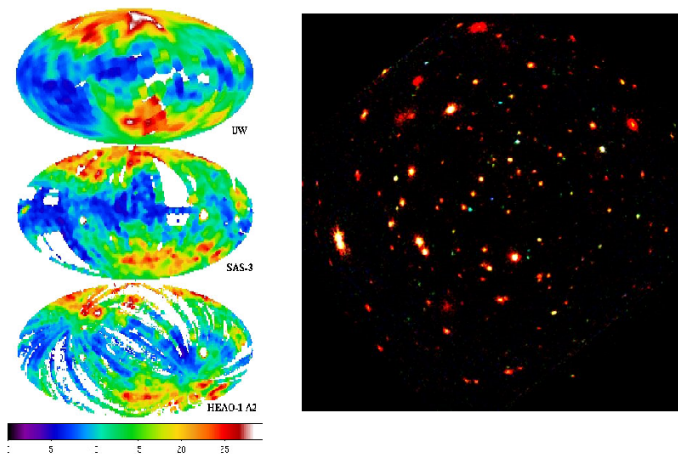


Figure 1.3: left: All-sky maps of the diffuse unresolved background in soft X-rays, right: CXB resolved into individual faint sources, by *XMM-Newton* (Hasinger et al., 1998; credits: left: http://imagine.gsfc.nasa.gov/docs/science/know_l2/diffuse_background.html, right: <http://apod.nasa.gov/apod/ap001109.html>)

1.3. Detection techniques

For the study of astrophysical X-ray sources, one has to face a lot of difficulties. The trouble gets even worse if the objects of desire are emitting hard X-rays. Nevertheless there is always a practicable solution, which often implies the need for some compromise.

Place of operation

Earth' atmosphere sets the first restriction to the operation of X-ray devices. It is only completely transparent for wavelength above 1 mm, which is the radio regime, and for the small part of the visible band (400–800 nm)¹¹. There are some minor windows in the infrared, but for X-rays (and γ -rays) one has to go up to higher altitudes (see Fig. 1.4). Some hard X-rays can be observed with high-altitude balloons, for less energetic radiation rockets are needed already and for the soft X-ray regime one has to use satellites. To avoid all the atmospheric disturbances and restrictions, Earth orbiting satellites are the solution of choice. This poses some technical difficulties, as it limits the weight and size of detectors, which have to be brought to space by rockets. The limited size may conflict with the detector's sensitivity and the detector also has to withstand the launch and the operation in the environment of outer space.

Further, the possible orbits where X-ray satellites function normally, are restricted to certain areas, because the Earth is enclosed in the so called 'van Allen radiation belts', where high energy particles are trapped in its magnetic field. So satellites orbit preferably below these regions to avoid disruptive background (see also Sec. 3.1; Giacconi et al., 1968; Charles & Seward, 1995).

Properties of X-rays

Certain X-ray inherent properties make them difficult to detect. These are:

- The amount of emitted photons can be less than 1 per day for weak sources (Schwartz, 2011).
- Their fluxes are very weak compared to the ever-present background fluxes.
- They do not refract or reflect easily, which makes the focussing of photons very difficult at high energies.

¹¹... which is exactly the waveband, the human eyes work on.

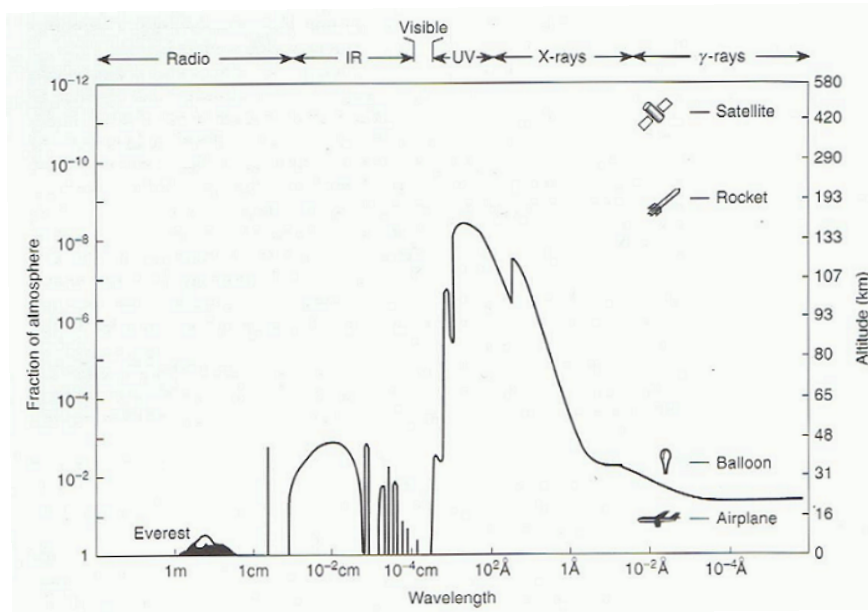


Figure 1.4: Absorption of electromagnetic radiation by Earth's atmosphere. The solid line displays the altitude by which half of the radiation has already been absorbed. Below that, almost all of it vanishes. Balloon-borne experiments can be used to study γ -rays, but for the X-ray and UV-region satellites are necessary (Charles & Seward, 1995).

The latter one arises from their short wavelength, which means quantum-physically spoken, they behave more like particles, than radiation of longer wavelength and have a much higher penetration power¹², thus normal optics cannot be used (Caroli et al., 1987; Groeneveld, 1999).

In the following a brief insight into the various kinds of X-ray detection techniques, and how they try to overcome the issues above, is presented. A conventional X-ray telescope comprises two essential elements, namely the optics, where the incoming radiation is somehow concentrated, and the detector, where it is then harvested. The optics accounts for the very few and weak fluxes of emitted photons, as it collects them. A very basic design for a collecting instrument is constituted by a simple mechanical collimator, which only gathers photons from a certain narrow angular region within the telescope's pointing to keep off radiation from other sources¹³. In early X-ray astronomy, as simple versions of Geiger or proportional counters (see: detectors, below) were equipped with honeycomb collimators, they suffered from low sensitivity and angular resolution because of the restricted FOV induced by collimation. Therefore they were only applied for strong sources, but the many weak ones called for another technology, pooled as the direct imaging or

Focussing techniques:

An imaging telescope provides a much better sensitivity, because the incident X-rays from a wider FOV are focussed onto a small part of the detection plane, while the background radiation is distributed uniformly. Hence also weaker sources are detectable. In the X-ray regime, imaging telescopes cannot be build with mirrors based on normal reflection, like they are for visible light, because for wavelength less than 1 nm, the radiation will scatter randomly¹⁴. The technique of 'grazing incidence reflection' circumvents that, by bundling the

¹²depending on the penetrated matter and the X-ray energies

¹³There are also several techniques to hold off cosmic ray particles, see e. g. Charles & Seward (1995) for further details.

¹⁴The typical distances between atoms are almost of the same order as X-ray wavelength, so the mirrors surface appears to be rough for them and they scatter in random directions (Kutner, 2003).

incident radiation in such a manner that they are aligned in a very narrow region ($1^\circ - 2^\circ$), almost parallel to the telescope's mirrors (Charles & Seward, 1995; Kutner, 2003).

X-ray optics: grazing incidence reflection: For very small grazing angles, even X-rays possess the ability to reflect. The critical angle ϕ_c for that grazing is derived from total external reflection, where a photon is incident on a medium, whose index of refraction is given by $n = 1 - \delta + i\beta$. The optical constants δ and β are $\ll 1$ for X-rays and proportional to λ^2 , where λ is the wavelength. The relation between incident and reflected angles is stated by Snell's law as follows:

$$\cos(\phi_r) = \frac{\cos(\phi_i)}{1 - \delta}. \quad (1.5)$$

The requirement for total reflection is then that no real solution for the reflected angle exists, which leads to the critical incident angle ϕ_c for X-ray grazing, above which total external reflection cannot occur and only refraction is possible¹⁵:

$$\phi_c = \sqrt{2\delta}. \quad (1.6)$$

For energies, away from absorption behavior of the reflecting material, $\sqrt{\delta} \propto \sqrt{N_e}/E$, with N_e being the electron density and therefore increasing with the atomic number Z . Hence the critical angle decreases with increasing energy like

$$\phi_c \propto \frac{\sqrt{Z}}{E}. \quad (1.7)$$

Materials with a high atomic number Z therefore provide larger critical angles and thus iridium, platinum or gold are commonly used (Schwartz, 2011).

X-ray detectors: proportional counters: Proportional counters consist of a chamber, filled with gas, where the incoming radiation ionises atoms, thereby creating free primary electrons due to the photoelectric effect, which themselves may release further secondary electrons, if the incident photons transferred enough energy. These electrons are then amplified by creating an avalanche, when moving towards the high-voltage anodes, where they are detected. The window where the radiation enters has to be on the one hand, strong enough to keep the gas contained and on the other hand, thin enough to let X-rays of all wavelength transmit. The detected signal is (in contrast to the in many ways similar Geiger counters) proportional to the photon's initial energy, which gave the detector its name.

X-ray detectors: scintillation counters: Proportional counters are only effective up to 10 keV because the gas has too less mass to stop photons at higher energies. Therefore scintillation counters use crystals that absorb the photons up to some MeV and re-emit parts of their energy as a flash of light, which then is detected by a photomultiplier. Often two different crystals are placed together in a so called 'phosphor sandwich', or short 'phoswich', one of them for X-ray detection and one for background exclusion. The emerging flash of light will then need different time-intervals until it is detected, depending on the place of its origin, which can thus be determined. If it occurred in both, it is a contribution from high energy background particles (e.g., cosmic rays), which can penetrate both crystals, and if it only occurred in the crystal used for background exclusion, it most possibly may have been

¹⁵For x-rays: $\delta > 0$. The maximum of $\cos(\phi_r)$ is 1, which leads to $\cos(\phi_c) = 1 - \delta$. Using the Taylor-approximation for small angles: $\cos(\phi_c) \approx 1 - \phi_c^2/2$, yielding: $\phi_c^2/2 = \delta$, or $\phi_c = \sqrt{2\delta}$.

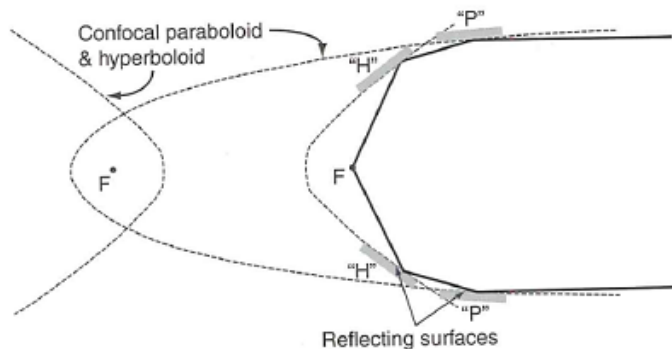


Figure 1.5: Configuration of hyperbolic and parabolic surfaces to build a Wolter type I mirror. The incoming X-rays are reflected at the concave parabola first and then off the hyperbola, in order to be focussed effectively. The first reflection focusses the radiation towards the left focus F , which at the same time is one focus of the hyperboloid, to which's second focus the radiation is then directed. The bold line shows a path of incident radiation that is bundled by that principle. (credits: Schwartz, 2011, p.12, Fig. 1.3)

a X-ray photon incident from the side or bottom (Charles & Seward, 1995; Kutner, 2003; Edgar, 2011).

X-ray detectors: Microchannel plates: Microchannel plates offer a high angular resolution, but to the extend of a relatively bad energy resolution. They combine many small tubes near each other to plates or even pairs of plates, exposed to an external field of high voltage. Incident radiation then creates photoelectrons, which in turn produces a avalanche in the hit tube and a electron-signal at its other end, which provides the impact position with very high accuracy. Unfortunately almost all information of the incident photon's energy is lost during that process, but they come up with the asset of not needing any consumables or cooling mechanisms.

X-ray detectors: Microcalorimeters: If X-rays collide with absorbing material, its temperature will rise. Microcalorimeters apply this principle by measuring the increase of temperature corresponding to a very tiny volume of material, which gives a precise energy resolution, but does require extensive cooling (Edgar, 2011).¹⁶

Technically, direct imaging telescopes utilize grazing incidence, by using a combination of paraboloid and hyperboloid surfaces inside a cone that gets slowly constricted, as first suggested by Wolter (1952), obtaining a resolution of a few arcsec and a field of view $\approx 1^\circ$ (see Fig. 1.5). The detectable energies range up to 10 keV and with multilayer optics even up to 100 keV. Nevertheless, many effects impede the use of X-ray reflection such as the preparation of the mirror's surface, unwanted scattering that scales with the square of the considered energies, or the finite size of the reflecting layers, which further have to be deposited on a substrate, requiring some binding layers and are subject to contamination. Thus the big disadvantage comes from the rather complex production process and the difficulty to collect and focus a large amount of photons.

Multiplexing techniques

Multiplexing techniques do not require focussing, as all others mentioned above do. The twist is that the direction of the incoming photons is encoded before they hit the detector, which means, they have to be decoded afterwards. This requires a lot of computational effort. Further, for focussing techniques only photons in a small part of the detector contribute to

¹⁶CCDs, which are missing in the enumeration above, will be described in detail in chapter 2.1.3.

noise, whereas for multiplexing every non-source photon, detected over the whole detection plane, contributes, resulting in a poorer sensitivity. Nevertheless they enable imaging even at hard X-rays and with a wider field of view. They can conveniently be divided into two subclasses, the first of which is called ‘temporal multiplexing’, where a scanning collimator is rotating over the detector and the counts of a point source are collected. The region of maximum of that counts represents the source’s position. They do not need a position sensitive detector (PSD), but the downside to them is, they are insensitive to variations of the source’s intensity on timescales shorter than the rotation period of the collimator.

The second class, the so called ‘spatial multiplexing’ comprises the coded aperture imaging techniques with their PSD, which shall be discussed in detail in the following chapter (Caroli et al., 1987; in’t Zand, 1992).

Chapter 2

Coded mask systems

2.1. Detection principle

A coded mask telescope consists basically of the Position Sensitive Detection plane (PSD) and a mask pattern, placed in some distance above it. The mask itself can be thought of as a combination of several single pinholes to build a pattern of pixels that either transmit the source's radiation (transparent pixels) or block it (opaque pixels). It therefore utilizes the ideal direct-imaging properties of pinhole cameras¹, but overcomes their ineffectiveness for weak sources due to their small throughput. There are several methods to construct mask patterns, all with different inherent properties (see Sec. 2.1.2).

The source fluxes arriving at the aperture of a coded mask telescope will be spatially modulated, producing many overlapping images in the recorded picture. This can be visualized as follows: For one single point source, the recorded distribution would equal the mask pattern exactly, but for several of them or for extended complex sources, the sum of many single overlapping distributions builds the recorded shadowgram (Fig. 2.1). The stated encoding

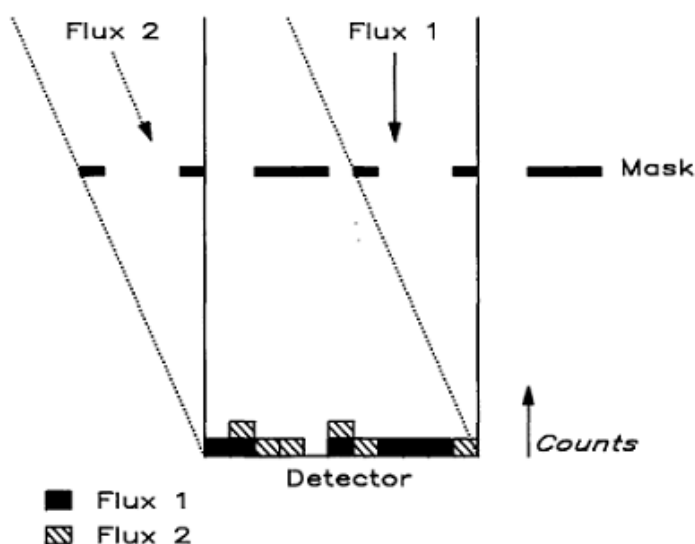


Figure 2.1: Detection principle of a coded mask system. The incoming radiation is spatially modulated by the mask pattern and then recorded as combined events from different sources. To be able to determine the contributing source's directions, a proper decoding is necessary (credits: Caroli et al., 1987, p.351, Fig. 2.1).

¹Pinhole cameras are in principle made of a box with a small hole that captures an inverted image of the viewed scene. The smaller the hole gets, the sharper the resulting image will be, but to the expense of sensitivity. Their ACF (Sec. 2.1.1) comprises a single peak with flat side-lobes, making them ideal imaging systems (in't Zand, 1992).

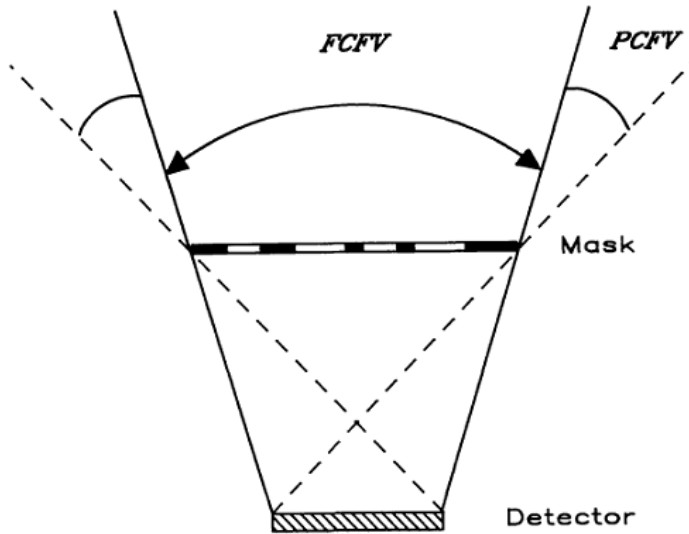


Figure 2.2: Illustration of FCFOV and PCFOV (here: FCFV and PCFV). It's obvious that their respective values are determined by the geometry of the system (credits: Caroli et al., 1987, p.352, Fig. 2.2).

process requires an appropriate decoding procedure in order to obtain a habitual sky image, which is where the downside of coded mask imaging, namely the large computational effort, comes in (Fenimore, 1980; Fenimore & Cannon, 1981; Caroli et al., 1987; in't Zand, 1992). The detected fluxes corresponding to transparent mask pixels comprise information about the source's intensities together with the background signal, whereas opaque areas only provide background fluxes. The so called Field Of View (FOV) equals the area from which the telescope is able to detect photons with its current pointing. It can be sub-divided into the Fully Coded FOV (FCFOV), where the incoming radiation is completely modulated by the mask, and the Partially Coded FOV (PCFOV), where only some fraction of the signal is viewed by the aperture and hence modulated (Fig. 2.2). The respective angles for both, the FCFOV and the PCFOV, depend on the telescopes geometry, in other words, on the dimensions of mask and PSD as well as on their separation (Caroli et al., 1987; Goldwurm et al., 2003).

In general there are three commonly used arrangements of aperture and PSD-plane. Firstly, mask and PSD can have equal dimensions, which implies that all sources emerge in the PCFOV except those exactly appearing in the on-axis direction. Secondly, the PSD could be larger than the mask-plane, which results in a somewhat wider FCFOV. Thirdly, and most preferably, the mask can be significantly larger than the detection-plane, leading likewise to a wider FCFOV, but additionally reduces financial as well as technical effort (Caroli et al., 1987; Groeneveld, 1999).

2.1.1. Characteristic quantities

The following quantities are introduced to be able to study a coded mask telescope's imaging properties more precisely.

Angular resolution

The system's angular resolution is defined as the angle Θ that one hole in the aperture-plane subtends at the detection-plane at distance D :

$$\Theta = \arctan\left(\frac{\text{mask pixel}}{D}\right)$$

Sensitive area

The system’s sensitive area comprises all transparent mask pixels, which contribute to the events received in the detection-plane. Thus for optimizing the sensitive area, the mask has at least to be equal in size as the detector.

To increase the angular resolution, one could either increase the number of aperture pixels, thus decrease their dimensions, or choose a larger mask-detector separation. To keep the sensitive area constant at the same time, the number of transparent pixels has to be increased accordingly, or in other words, the **open fraction** (OF^2) has to be kept unchanged (Goldwurm et al., 2001, 2003).

System Point Spread Function (SPSF)

For coded mask telescopes, the SPSF is used to study the quality of choice of the mask pattern M and the corresponding decoding array G^3 . It is defined as the correlation of M with G and represents the response to a point source in the reconstructed image: $SPSF = M \star G$. In general, the SPSF does not equal a δ -function, which means, a point in the source distribution will be broadened over more than one pixel in the reconstructed image, or in other words, the SPSF consists of a central peak, which matches the point source, surrounded by spurious side-lobes, the so called artifacts. Further, for complex extended sources, the presence of such side-lobes introduce some cross-talk effect between the single point-like sources, thereby adding to the image’s deterioration (Fig. 2.3).

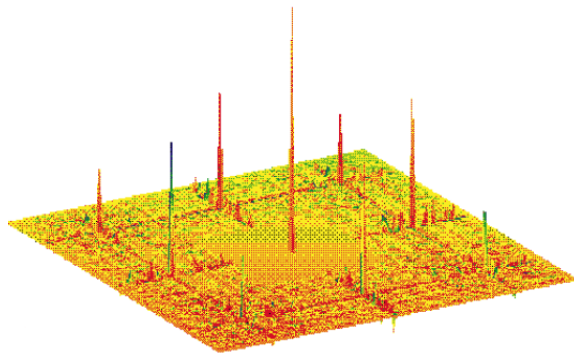


Figure 2.3.: Example of a SPSF with side-lobes that appear as artifacts. The main peak in the middle corresponds to the point in the source distribution and is surrounded by several smaller false ghost-peaks (Goldwurm et al., 2003, p.225, Fig.3).

To analyse the mask’s intrinsic properties, one can also use the **Autocorrelation Function (ACF)**, which simply is defined as the correlation of the mask pattern M with itself (Caroli et al., 1987).

Modulation Transfer Function (MTF)

With the MTF one can gather information about the imaging performance of the telescope, which in general depends on the ability, to reconstruct the intensity as well as the spatial distribution of the source fluxes correctly. The MTF shows the transmission strength in the spatial frequency domain and is defined as the fourier transforms of the correlation of M and G . Again, a well chosen mask pattern and decoding array, minimizes degradation and guarantees that the intensity of all transmitted frequencies is constant. So, a flat MTF would serve best, but in real systems, the finite sized mask pixels and noise contribution conflicts

²The open fraction is the amount of transparent pixels in relation to all pixels. Its typical value ranges around ~ 0.5 .

³The decoding array is derived in a particular manner from the mask pattern and, as its name suggests, needed for the decoding process during the image reconstruction, if cross correlation is used (see section 2.2.2). Since this thesis focuses on the use of correlation methods, all the characteristic properties are introduced with respect to them.

with that requirement. The MTF also gives the possibility to account for further physical effects, like influences of the mask material (Fenimore, 1980; Caroli et al., 1987).

Signal to Noise Ratio (SNR)

One further characteristic quantity to evaluate the system's quality, is provided by the SNR, which comprises the minimum flux level that can still be detected by the instrument. Its theoretical value is stated as the expected source intensity per pixel S_{ij} divided by the respective noise term σ_{ij} , where the variance of the noise is given by:

$$\sigma_{ij}^2 = \sigma_{ij}^2(S_{ij}) + \sigma_{ij}^2(\mathbf{S}) + \sigma_{ij}^2(\mathbf{B}). \quad (2.1)$$

The first term describes statistical variations due to the object itself in the (i,j)th-direction, the second comprises statistical effects due to all other objects within the FOV as well as systematics due to the SPSF side-lobe induced cross-talk, and the last one is dedicated to the total background (Caroli et al., 1987).

2.1.2. Mask patterns

Aperture patterns have to be chosen in such a manner that each detected source inside the FOV casts a very unique shadowgram, meaning, the source's direction can be designated unambiguously. Therefore, if the mask consists of an arrangement of basic patterns, one row and one column must be excluded to avoid that two sources from different directions can produce the same recorded distribution. In general, a well chosen pattern that is adapted to the detector and its field of application, speeds up the reconstruction process and reduces its complexity (Caroli et al., 1987; Groeneveld, 1999; Goldwurm et al., 2003).

To produce a sufficient mask pattern, many different and partially rather complex procedures have been suggested, which shall not be reviewed in detail here (see, e.g., Busboom et al., 1998; Gunson & Polychronopoulos, 1976; Groeneveld, 1999). Instead an overview of patterns, categorized due to their imaging capabilities will be presented without being completely comprehensive.

Imaging with artifacts

The Fresnel zone plate shall be mentioned here, despite the fact that it is rather used for tomographic imaging, than for high energy astronomy, because it has been the very first realization of a coded aperture pattern. Its transmission varies continuously like $\sim \cos(r^2)$, which is practically realised by an arrangement of concentric annuli that alternate in their permeability. Its ACF is corrupted by concentric lobes due to the finite values of both, the transmission function and the aperture dimensions (Barrett & DeMeester, 1974; Caroli et al., 1987; Mertz & Young, 1961).

Random patterns can be thought of as extensions of the former mentioned pinhole cameras (section 2.1) that keep their good resolution, while their sensitivity is increased due to the use of many such 'pinholes' as pixels in a random distribution of opaque and transparent elements. In principle, random patterns of arbitrary dimensions and open fraction can be used, but their exact arrangement may be optimized with respect to their tendency to produce artifacts (Caroli et al., 1987).

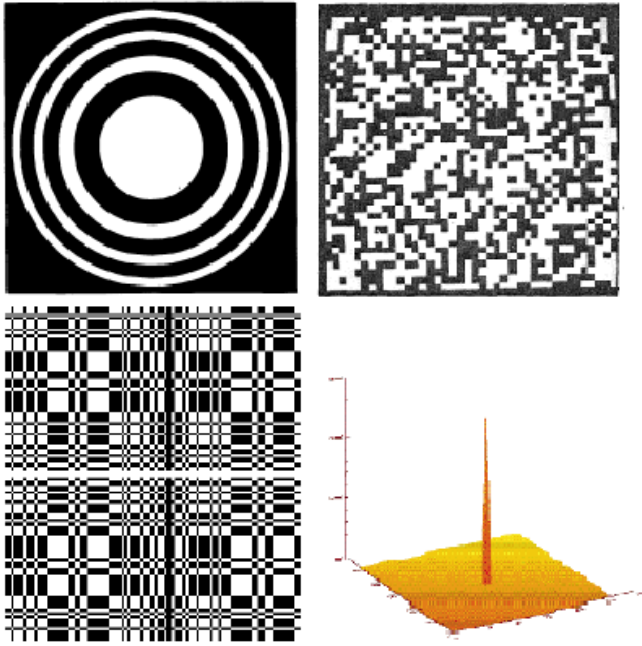


Figure 2.4: Mask patterns with different inherent imaging properties. Top left: fresnel zone plate with alternating transparent and opaque annuli. Top right: 40x40 random pattern. Bottom: Modified URA (MURA) as used for IBIS on *INTEGRAL* with its side-lobe free, δ -like ACF. MURAs also have ideal imaging characteristics, but are derived in a different way, than URAs, as proposed by Gottesman & Fenimore (1989). They also differ in size and symmetry, which leaves the choice of pattern to the application. (credits: Top left: Caroli et al., 1987, p.363, Fig.3.1; Top right: Fenimore & Cannon, 1978, p.341, Fig.5; Goldwurm et al., 2003, p.224, Fig.2)

Nearly perfect imaging

The basic idea behind the so called Non-Redundant Arrays (NRAs) is that the vector spacing between any transparent pixels must not be present more than once within the whole mask-plane, which leads to ideal imaging characteristics, as long as the object's extension is smaller than half the maximal spacing between two holes. Thus for a large FOV, huge mask dimensions are necessary, and further the open fraction and hence the instrument's sensitivity is severely limited, which makes NRAs no practical option for high energy astronomy (Golay, 1971; Fenimore & Cannon, 1978; Caroli et al., 1987).

Optimum systems

Patterns derived from cyclic difference sets⁴ as proposed by Fenimore & Cannon (1978), possess the property of being almost artifact-free, since they combine the flat side-lobe characteristic of the NRAs with the high sensitivity of random patterns. The occurrence of the vector spacing between transparent pixels is a certain constant value, which gives them ideal imaging characteristics and also their name: Uniformly Redundant Arrays (URAs). URAs are content with smaller detection-planes compared to random patterns, and they do not suffer from inherent noise, which restricts the SNR in the random array case. Their artifact-free nature remains as long as sources are within the FCFOV, whereas in the PCFOV the SPSF possesses spurious lobes as shown in Fig. 2.3 and the sensitivity declines (Goldwurm et al., 2003).

2.1.3. Position sensitive detection plane

In X-ray astronomy the Position Sensitive Detection plane (PSD⁵) has to resolve each photon's impact position as well as its energy. This is quite different from the detection mechanism in

⁴See Busboom et al. (1998), p.106, def. 2.9 and references therein, for mathematical description.

⁵The information provided in this section was taken from the very good and comprehensive Grant (2011).

the optical range, where the single photon's energies are too small to be detected individually and a bigger amount of photons has to be collected over longer time intervals, which may even need some amplification afterwards. For that purpose usually a Charge-Coupled Device (CCD) is used, which captivates by its high sensitivity and its linear response to the input signal, meaning the detected intensity is always proportional to the initial input energies. A different kind of choice for a PSD, the so called Cadmium Zinc Telluride (CZT) detectors are reviewed in chapter 3.3.

CCDs

Since their invention in 1969 (Boyle & Smith, 1970), they have found wide application, for instance in almost all digital cameras, and they were first used in space for the observation of a SN in 1987. CCDs utilize a semiconductor substrate to create electron-hole pairs by the photoelectric effect⁶, which build the basis of the detected signal.

Function principle: The impinging photons are absorbed with a certain probability whilst traveling through the substrate, which's inverse gives the attenuation length. This average penetration length a photon can travel before being absorbed by the material is depicted in Fig. 2.5, which also shows the typical energy range a CCD works best in for X-rays, of about 0.1 – 10 keV. Photons of other energies may be absorbed too early in the surface or even pass the whole substrate without being recognized. The number of generated electrons N_e within the active region has the following linear dependency on the initial X-ray's energy E_x :

$$N_e = \frac{E_x}{W}. \quad (2.2)$$

Typical values for the work function W in silicon are very small, so a huge number of electrons may be released, which have to be stored immediately, since this charge cloud would otherwise partially recombine, or drift from its spot of creation. The collective element in a CCD can either be a Metal-Oxide-Semiconductor (MOS)⁷, which shall not be reviewed in detail here, or a p-n junction, which is doped with materials of either three valence electrons (p-type) or five (n-type)⁸. A depletion region will form at the junction due to recombination of electrons and holes, which can be further extended by an appropriate applied voltage and serves as the interaction ground for the incoming radiation. Above the junction usually three gates confine the dimensions of the CCD's pixels. The storage of the generated electrons is achieved by a positive voltage at the middle gate creating a potential well to its neighbors and a separation of the perpendicular region by stripes of insulators (see Fig. 2.5). In order to transfer the charge to a read-out electronics and empty the potential wells, a higher voltage is used in certain time intervals at all the neighboring pixels, which forces the charge cloud to move pixelwise. At the end of all the columns, the collected charges can either be read out simultaneously, or all the charges may further be moved in the perpendicular direction and read out collectively.

⁶A metal surface absorbs the energy of incident photons ($E = h\nu$), which leads to the ejection of electrons that have smaller kinetic energies, because each electron has to use up a work function W depending on the surface material. Therefore its maximum kinetic energy can be written as $E_{\text{kin,max}} = h\nu - W$ and may be further reduced by collisions (Einstein, 1905).

⁷Its basic parts are an insulator inbetween a metal gate and a p-type semiconductor. It can analogously build out a depletion region and store electrons in potential wells but to the extense of lost trapped charges. This can be circumvented by an additional n-type layer.

⁸Boron is usually used for the p-types and phosphorus for n-types. The 'p' refers to its positive character

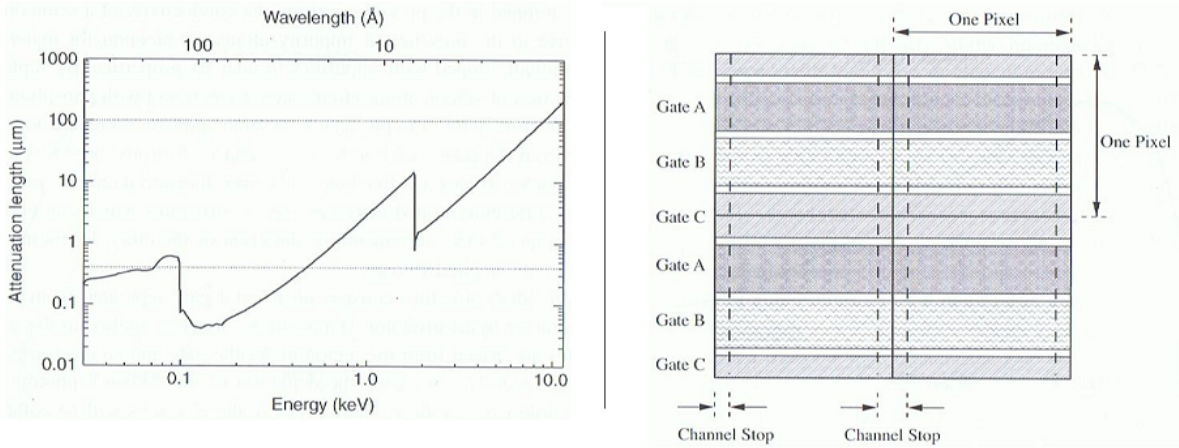


Figure 2.5.: Left: Attenuation length for X-rays in a CCD in dependence of their energies and wavelength. The bold line depicts the mean path-length a photon may travel, before it is absorbed by the material. The lighter dotted lines mark the energy-range CCDs work best in. Right: Formation of the pixelated structure in a CCD with the three gates confining one direction and the channel stops the other. (credits: Grant, 2011, Left: p. 41, Fig. 3.1; Right: p. 44, Fig. 3.3)

Characteristic quantities: QUANTUM EFFICIENCY (QE): The QE takes into account that some photons are absorbed unwantedly in the wrong so called 'dead layers' made up of e.g. the gates or channel stops, and some of those reaching the detection plane are not absorbed within it, though they are wanted to. The QE is derived by multiplying the transmission through each dead layer separately, which behaves like $e^{-\mu_i t_i}$ for the i -th layer, and then also the absorption in the photo-sensitive region:

$$\text{QE} = \prod_i e^{-\mu_i t_i} (1 - e^{-\mu_{Si} t_{Si}}), \quad (2.3)$$

where the μ_i denote the absorption coefficients of the respective media and the t_i their thicknesses.

SPECTRAL RESOLUTION: The spectral resolution, or also called, the Full Width at Half-Maximum (FWHM) comprises variance-terms of the readout noise as well as of secondary ionisation processes:

$$\text{FWHM} \propto \sqrt{\sigma_e^2 + \sigma_{\text{read}}^2}, \quad (2.4)$$

and is at its best value for low readout noise levels, as well as efficient charge collection and transfer mechanisms.

LOW-ENERGY EFFICIENCY: The gates at the front side of a CCD and the filters used to block parasitic optical radiation also build an obstacle for low-energy photons. Therefore 'back-illuminated' CCDs may be used, in which the substrate is swapped with the blocking structures. Thus on the surface only a very thin dead layer is left and low-energy radiation can hit unscreened, but on the downside, also the resolution and noise contribution may worsen.

Practical operation: In practice there are a lot of effects and detector features that have to be considered, in order to analyse and understand the data sent from a satellite

due to supernumerary free holes and 'n' the opposite way.

fully, or to perform simulations employing a realistic detector setup. For instance, the charge does not necessarily need to be contained within one CCD-pixel, it may split over two or even multiple pixels, which then leads to an increased noise level, since the noise of more than one pixel is included in the restoration of the incident energy and thus also the spectral resolution deteriorates. Further defect ‘hot pixels’ may produce signal events without actually detecting radiation, which is even more disturbing in view of the usually very strongly limited telemetry bandwidth. Also photons impacting in a narrow region may be confused with being a single event, if their delay is smaller than the device’s readout time. The environment may additionally influence or harm the CCD’s performance, by contaminating its surface or damage it through radiation or micrometeoroids. Eventually the cosmic particle background’s contribution has to be considered, which may look like fake X-ray events (see Cha. 5).

2.2. Image reconstruction theory

As already said, coded aperture imaging involves two steps: the encoding of the incident radiation by the aperture, and the decoding of the detected events by a computer algorithm that is well adjusted to the respective imaging system and desired results. The detected intensity distribution $D(\vec{x})$ is derived, in the ideal case, simply as the correlation of the mask pattern $M(\vec{x})$ with the actual sky image $S(\vec{x})$, whilst in the real case, one has also to account for the background contribution $B(\vec{x})$, as well as a signal independent noise term $N(\vec{x})$ induced by the detector. The background array $B(\vec{x})$ comprises all photons, which are too weak to be detected individually, or can not be associated with a source directly. Since $B(\vec{x})$ appertains to the original sky signal, it is also modulated by the aperture. The noise array $N(\vec{x})$ has its origin in intrinsic influences of the detector system and is hence not coded by the aperture. This situation can be summarized in the **coding equation** as follows, where \star denotes the correlation operator:

$$D(\vec{x}) = (S(\vec{x}) + B(\vec{x})) \star M(\vec{x}) + N(\vec{x}). \quad (2.5)$$

Or, in its discrete formulation:

$$D_{jk} = \sum_l \sum_i (S_{li} + B_{li}) M_{j+l, k+i} + N_{jk}, \quad (2.6)$$

where the summations should go up to infinity, but are practically limited by the finite FOV.

In principle, one can consider whichever physical effect within $B(\vec{x})$ and $N(\vec{x})$, such as signal-intrinsic Poissonian noise, or the influence of the detectors finite spatial and temporal resolution. Thus, the better these effects are understood and modeled, the better the results of the reconstruction will be (Fenimore & Cannon, 1981; Caroli et al., 1987; Gottesman & Fenimore, 1989; Groeneveld, 1999; Goldwurm et al., 2003).

2.2.1. Concepts of different methods

There are several approaches conceivable to obtain an estimate $S'(\vec{x})$ of the sky image, which shall be reviewed in the following. Backprojection, inversion and correlation methods can be considered as to be ‘linear’, in the sense that they are based on a linear combination of the data to get an intensity estimate for each pixel. Non-linear techniques account for the non-Gaussian, but Poissonian properties of noise, which is especially important, if only a small amount of photons is detected per pixel (Skinner, 2003).

Non-linear methods

Maximum Likelihood (ML) as proposed by Skinner & Nottingham (1993) is best suited for cases where the positions of a small amount of weak sources are already known, and the objective is to either extract more sophisticated information, e. g. light curves or spectral distributions, or to be able to subtract their impact on the image reconstruction and therefore also remove coding noise associated with them. It determines the probabilities for combinations of different source intensities that could in principle build the observed fluxes and then chooses whichever matches with the highest probability. ML can be applied to non-optimum systems.

Another iterative method was introduced by Willingale (1981) to X-ray astronomy, the Maximum Entropy Method (MEM). It is based on the definition of an entropy function, which is then maximized in order to find the intensity distribution, which again fits the observed data best. Iterative methods can produce better results than linear methods in some cases, but they do require more computational effort, which makes them impractical for complex systems (Ballesteros et al., 1997).

Backprojection

This method traces the trajectory of each photon back onto a projected map of the aperture in the sky. In principle all regions, the photon could originate from are tagged (hence it is sometimes referred to as ‘photon-tagging’), and the spots which are tagged the most, state the source’s positions. Photons that must have traveled through opaque pixels are assigned to the background. Its application is mainly for small numbers⁹ of detected photons, since it may save some computational time with respect to correlation methods described below (in’t Zand, 1992; Groeneveld, 1999; Skinner, 2003).

Inversion

Equation 2.6 can also be formulated as a system of linear equations, as follows:

$$\vec{d} = W\vec{s} + \vec{n}, \quad (2.7)$$

where \vec{s} contains both, the contribution from the source’s intensities as well as the background part. The matrix \vec{W} is derived from the aperture $M(\vec{x})$ in a way that each row of it, is associated with the respective entries of \vec{s} , that determine the measured signal in the corresponding pixel of the detector and each column represents the part of the aperture, which is coded by the respective source element. The former matrices $D(\vec{x})$, $M(\vec{x})$ and $N(\vec{x})$ are reordered in a certain way to form the vectors in equation 2.7. If \vec{W} is a square, non-singular matrix, it can be inverted in order to solve equation 2.7 for an estimation of the source’s intensities \vec{s}' :

$$\vec{s}' = W^{-1}\vec{d} = \vec{s} + W^{-1}\vec{n}. \quad (2.8)$$

This methods downsides are that firstly \vec{W} has to be invertible and further, if it is almost singular, the noise can be the dominating part in the reconstructed image, since the inversion gives rise to large elements in \vec{W} . such matrices are termed to be ‘ill-conditioned’ and occur, if rows are nearly a linear combination of others, which is a quite common feature especially for random masks (Caroli et al., 1987; in’t Zand, 1992).

⁹compared to the amount of mask-pixels

Correlation methods

The most common method compares the mask pattern (or some decoding function derived from it, see section 2.2.2) with the detected distribution in order to find the best conformity, by cross-correlating both. It gives results of high quality for optimally coded systems, which employ URAs or MURAs and approximates the source's positions and intensities very good for others. This method shall be used throughout this thesis and will therefore be explained in detail in the next section and applied in chapter 4.1.4.

2.2.2. Balanced cross correlation

Cross correlation solves the coding equation 2.6 for a sky image estimate, by introducing a appropriate decoding array $G(\vec{x})$, which leads to the **decoding equation**:

$$\begin{aligned} S'(\vec{x}) &= D(\vec{x}) \star G(\vec{x}), \\ \text{or} \quad S'_{jk} &= \sum_l \sum_i D_{li} G_{j+l, k+i}. \end{aligned} \quad (2.9)$$

Inserting D gives:¹⁰

$$\begin{aligned} S' &= ((S + B) \star M + N) \star G \\ &= S \star M \star G + B \star M \star G + N \star G, \end{aligned} \quad (2.10)$$

which simplifies for the ideal case, where $M \star G$ is a δ -function, to:

$$S' = S + B + N \star G. \quad (2.11)$$

This emphasizes the need for a good choice of M and G , since equation 2.10 can then be approximated by the above form, and S' differs from S only by the $(B + N \star G)$ -term. If the mask further is derived from the same basic pattern repeated in a cyclic configuration and the noise term follows a smooth distribution, that term does not vary much and can hence be subtracted. But even for those cyclic correlations, artifacts will occur for all shifts that are non integer multiples of the cycle period. These 'ghosts' correspond to repetitions of the real signal peak and occur at multiple offsets from it that have their minimum angle defined by the size and distance of the basic pattern from the detection plane. To prevent that, often collimators constrain the incoming fluxes to smaller angles and they also avoid the contribution from aperture edges to the coding, which could add to ghosting for far off-axis sources. But the use of collimators also worsens the SNR, besides they can increase the background influence and require sophisticated manufacturing techniques for high energy applications (Caroli et al., 1987; Skinner & Nottingham, 1993).

Fenimore & Cannon (1981) introduced a way to derive the decoding array G , which automatically smoothens out the side-lobe values of the SPSF, meaning any d.c. background will be removed. This balanced correlation is achieved by employing some negative values in G to balance the positive terms in M , as follows:

$$G_{jk} = \begin{cases} 1, & \text{if } M_{jk} = 1 \\ \frac{\text{OF}}{\text{OF}-1}, & \text{if } M_{jk} = 0. \end{cases} \quad (2.12)$$

¹⁰For simplicity the spatial dependency $D(\vec{x})$ is omitted hereafter.

For a typical value of the Open Fraction (OF) of 50% opaque mask elements are thus weighted with a negative factor of -1 . The weighting term w for G is derived by using the balancing requirement that the sum over all aperture elements vanishes:

$$\sum_i a_i \stackrel{!}{=} 0 \Rightarrow \text{OP} + \text{CP} \cdot w \stackrel{!}{=} 0, \quad (2.13)$$

with OP and CP denoting the amount of open and closed pixels respectively. Solving this for w , replacing the closed pixels via the number of all pixels (N) and finally inserting the open fraction $\text{OF} = \text{OP}/\text{N}$, leads to:

$$w = \frac{-\text{OP}}{\text{N} - \text{OP}} \Rightarrow w = \frac{\text{OP}}{\text{OP} - \text{OP}/\text{OF}} = \frac{\text{OF}}{\text{OF} - 1}. \quad (2.14)$$

Another possible choice for G is to weight the opaque pixels with the average value λ of the ACF's side-lobes, like:

$$G_{jk} = \begin{cases} 1, & \text{if } M_{jk} = 1 \\ \frac{-\lambda}{\text{OP} - \lambda}, & \text{if } M_{jk} = 0. \end{cases} \quad (2.15)$$

EXCURSION: convolution vs. correlation

Since these two terms are getting mixed up quite often, even in specialized literature, they will be distinguished mathematically hereafter. Their computation will be explained and depicted graphically afterwards, because having a clear idea about what correlation really does, is essential for the performance of the reconstruction algorithm in chapter 4.1.4. Both of them are used to compare two signals and determine the similarity between the first one, and a (time-) shifted version of the second.¹¹

Table 2.1.: Mathematical formulation of convolution and correlation in one dimension. They are usually discerned with the different 'star-symbols'. The integration goes up to infinity in both directions. The capital functions denote their respective fourier transforms in frequency domain. For correlation a more general formulation would have been: $F(\nu)H(-\nu)$, but since often the functions are real: $H(-\nu) = H(\nu)^*$.

convolution	correlation
$\text{conv}(f, h) = f \star h = \int f(\tau)h(t - \tau)d\tau$ $= F(\nu)H(\nu)$	$\text{corr}(f, h) = f \star h = \int f(\tau)h(t + \tau)d\tau$ $= F(\nu)H(\nu)^*$
discrete:	
$(f \star h)_j = \sum_i f_i h_{i-j}$	$(f \star h)_j = \sum_i f_i h_{i+j}$
	ACF: correlation with itself
	$g \star g = G(\nu)G(\nu)^* = G(\nu) ^2$

Both can be pictured as a combination of a signal- (the detected photon distribution, in our case) and a response-function (the decoding array), where the response (also termed 'kernel')

¹¹The two functions to be compared will be formulated with a time dependency, since that is the way they are mostly used (digital signal processing). All the above can be transferred easily to the 2-dimensional case.

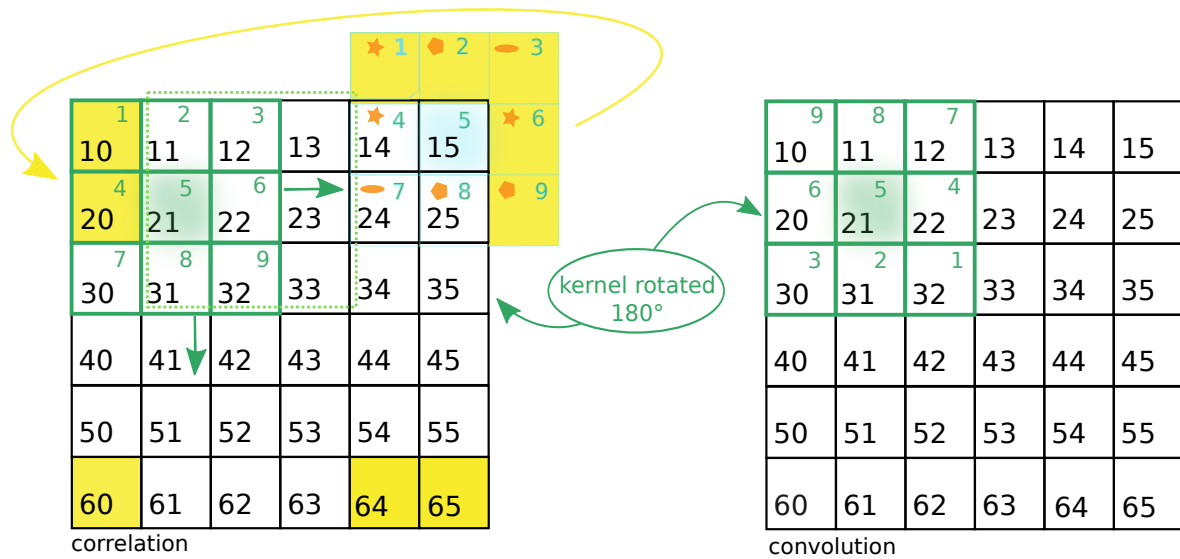


Figure 2.6.: Correlation/convolution of two arbitrary chosen arrays. The smaller green array depicts the kernel, as it is moved over the signal representation. The light-green element in its middle marks the element of the new array that would obtain the value 1131 ($1 \cdot 10 + 2 \cdot 11 + 3 \cdot 12 + 4 \cdot 20 \dots$) in the shown case. The yellow-colored regions outside the signal's borders need padding, so they are either filled up with near elements mirrored across the borders, as indicated by the orange symbols, or the also yellow marked entries from the opposite sides are used.

smears out the signal in a certain way. Or, the other way round, they describe the amount of overlap as the response is shifted over the signal. They only differ by their '-' or '+' sign respectively, which equals a 180° -rotation of the kernel. It also means, convolution and correlation are the same, if the kernel is symmetrical. So, what one really gets out of a correlation/convolution of two arrays is a new array whose entries describe the strength of correlation in that spot (in our case: high value entries indicate the position of a source). To determine the array elements, the correlation does exactly what is described by above formulas, it places the kernel above the signal, multiplies all the corresponding entries element-wise, adds up these products, and saves the number as the new result-entry. Then the kernel is moved one pixel forward and the procedure repeats itself.

When the kernel slides over the borders, it encounters a problem, as illustrated by the yellow-shaded regions in Fig. 2.6. The values outside the borders have to be padded, which is usually done by filling them with the array mirrored across the borders, or sometimes the array wraps around and uses the entries on the opposite side.

2.3. Former and future missions

Since the first suggestion by Mertz & Young (1961) to employ coded mask systems in astronomy to study high energy phenomena, and their first tentative steps using a mask design as proposed by Gunson & Polychronopoulos (1976) on a rocket in 1976 (SL 1501), coded mask telescopes have been subject to various follow-up missions, and more recent successes with such systems are overviewed briefly in this section.¹²

¹²See: http://astrophysics.gsfc.nasa.gov/cai/coded_inss.html for a more extensive list.

INTEGRAL: The INTERnational Gamma-Ray Astrophysics Laboratory (*INTEGRAL*) was launched by the European Space Agency (ESA) in 2002 and includes three coded aperture telescopes, which are the SPectrometer on Integral (SPI), the Imager on Board the Integral Satellite (IBIS) and Joint European X-Ray Monitor (JEM-X). SPI uses Germanium detectors for spectral purposes in the 20 keV – 8 MeV-domain and JEM-X supports the two main instruments with a gas chamber detector in the 3 – 35 keV-regime. The IBIS utilizes a MURA-mask (see Fig. 2.4, bottom) above a CdZn-PSD and obtains high resolution images over a range of 15 keV – 10 MeV. In more than 10 years by now, *INTEGRAL* completed our knowledge of high energetic processes by mapping the galactic plane in γ -rays, resolving the galactic center’s diffuse emission and locating a huge quantity of different sources (Goldwurm et al., 2003; Winkler et al., 2011)¹³.

BAT on *Swift*: The Burst Alert Telescope (BAT) on the *Swift*-satellite started operation in 2004 and still is in orbit, although it was originally planned for 7 years. It’s main objective is to study Gamma Ray Bursts (GRBs), which are among the most violent and intense processes known. On average these outbursts are very brief in duration, from a few msec to a few 100 msec. The BAT is one of three instruments on *Swift*, which cooperate to gain new insights in the mechanisms behind GRBs and work in the X-ray and optical/UV-domain. BAT itself studies the hard X-ray and γ -ray wavelength within a large FOV and to high sensitivity using a random patterned coded mask and a CZT detection plane (see Fig. 2.7). It can operate in two different modes, a burst mode to determine the burst’s positions, and a survey mode to conduct hard X-ray surveys. The survey mode is equipped with a burst alert system (hence the telescope’s name) to identify GRBs timely and switch to the photon-by-photon burst mode. *Swift* has been very successful so far, in fact it performed the most comprehensive GRB studies ever. For example, it found the most distant object at a redshift of 8.3, confirming GRBs as very early-universe objects. BAT already found more than 400 AGNs amongst its around 100 new discovered sources per year, and it conducted the deepest hard X-ray survey to date (Krimm, 2003; Markwardt & Gehrels, 2004; Barthelmy et al., 2005)¹⁴.

ProtoEXIST: *ProtoEXIST1/2* are balloon-borne experiments, for testing purposes of the advanced CZT-detector setup for the proposed High Energy Telescope (HET)¹⁵ that will be part of the Energetic X-ray Imaging Survey Telescope (*EXIST*). It is not yet clear, if *EXIST* is going to fly, but nevertheless significant progress is being made in developing the CZT-detectors for such a mission, which is also quite relevant for the MIRAX mission described in the next chapter.

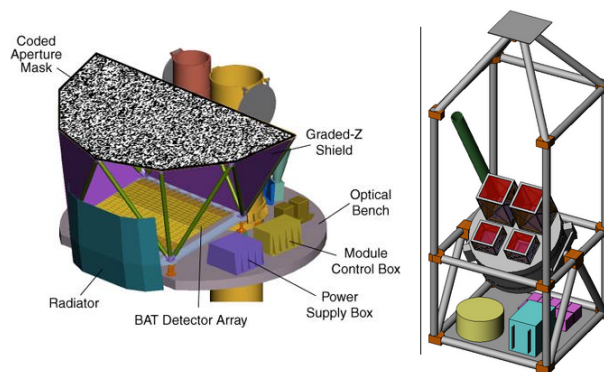


Figure 2.7.: Left: Illustration of the coded mask instrument BAT. Right: *ProtoEXIST* balloon gondola with its four coded mask telescopes. Credits: Left: http://swift.gsfc.nasa.gov/docs/swift/about_swift/bat_desc.html, Right: <http://hea-www.harvard.edu/ProtoEXIST/instrument.html>

¹³And: <http://science1.nasa.gov/missions/integral/>, <http://sci.esa.int/integral>.

¹⁴And: <http://swift.gsfc.nasa.gov/docs/swift>

¹⁵as described by Hong et al. (2010)

Chapter 3

MIRAX

The simulations (see chapter 4) presented in this thesis were done to do preliminary studies for the Hard X-ray Imager of the ‘MIRAX’-mission, which will be part of Brazil’s first program involving space based scientific studies. There will be contributions from the Smithsonian Astrophysical Observatory (SAO), the Universities of California, San Diego and Berkeley (UCSD and UCB), the Massachusetts and the California Institute of Technology (MIT and CalTech) and the NASA Goddard Space Flight Center (GSFC), and on the German side from the Erlangen Centre for Astroparticle Physics (ECAP) and the Institute for Astronomy and Astrophysics Tübingen (IAAT).

All the information provided below was taken from the proposal presented to NASA by Grindlay (2011) if not stated otherwise and may not be in its final version.

3.1. Mission overview

The Monitor e Imageador de RAios-X (MIRAX) will be the first astrophysical space mission of the Brazilian Space Agency (AEB) onboard the *Lattes* satellite which will be launched in 2017 (Castro et al., 2012). It will conduct a hard X-ray survey (5 – 200 keV) of the southern Galactic plane and the Galactic bulge, with 15 scans per day of its inner part and also cover a large region of the extragalactic sky. It will operate in a low inclination orbit such that the influence of parasitic radiation like the South Atlantic Anomaly (SAA¹) or the radiation belts will be less severe compared to BAT on *Swift* or to IBIS on *INTEGRAL*.

With its emphasis on the higher count rates at 5–15 keV it covers a sensitivity region which has not been covered by other hard X-ray surveys before². MIRAX will be pointing 25° off the south of zenith in order to maximize the coverage of the central Galactic plane. Fig. 3.1 illustrates the sky coverage and sensitivity for 1 year of scanning. An angular resolution³ of 5.5′ and an energy resolution of 2–3 keV enable very unique imaging possibilities and spectral studies with a position accuracy of ~ 1 arcmin. Its event mode telemetry with a resolution from milliseconds to years allows timing studies of wide scope.

¹The SAA is a region in Earth’s orbit where the Earth’s magnetic field is at a minimum, enabling high energetic particles from the lower Van Allen belt to cross this region, thereby exposing satellites to a somewhat increased radiation (Fürst et al., 2009).

²for comparison: hard X-ray survey of *INTEGRAL*: 17 – 60 keV

³which is 2.5 – 4 times better compared to IBIS or BAT

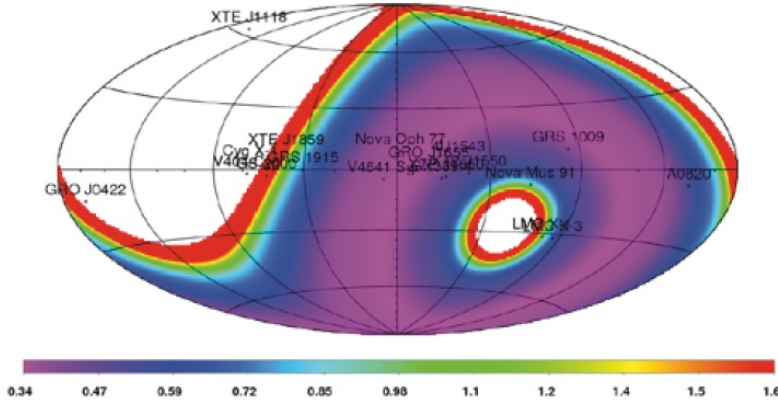


Figure 3.1: Sensitivity map for a period of 1 year of scanning with exposure from 5 – 150 keV. The scaling is in mCrab and reaches from high fluxes in red (1.6 mCrab) to lower fluxes in violet (0.34 mCrab).

MIRAX will be orbiting in a altitude of 650 km in a near equatorial region with an inclination of 15°. It will scan continuously during its 4 year operation time and send the data back to Earth once every 97 min orbit to its Brazilian ground station during a window of 15 min.

The *Lattes* spacecraft will be brought to space on a Taurus class commercial vehicle and will carry two experiments, namely the MIRAX-HXI and the EQUARS which will consist of some Earth observing instruments. The nadir-pointed low-Earth orbit and its inclination meet the requirements of EQUARS, and the off-axis mounting of MIRAX, with respect to the spacecrafts pointing towards the zenith, is imposed by the HXI. The EQUARS instrument will be mounted below the HXI and both will have their viewing directions opposite to each other (Fig. 3.2).

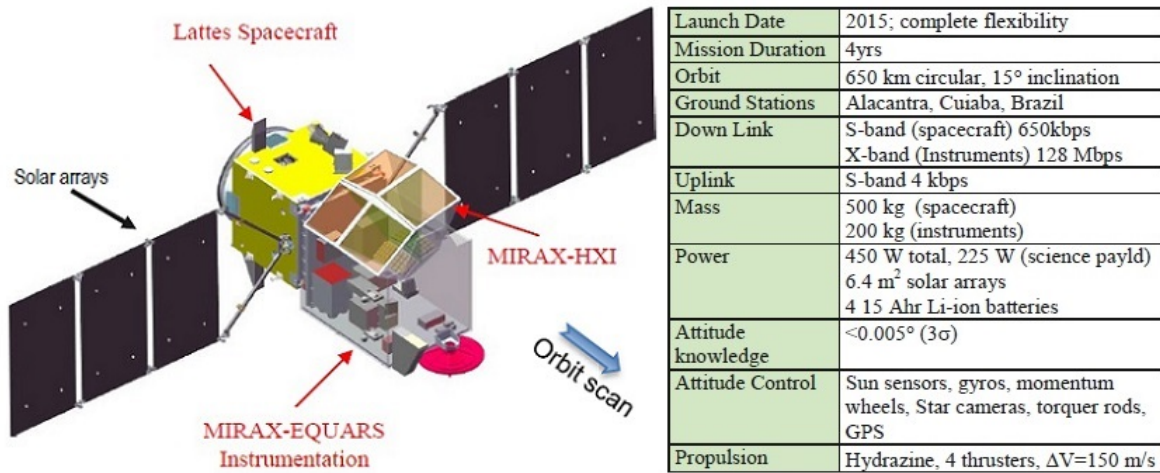


Figure 3.2.: Left: The Lattes spacecraft with its two instruments mounted in opposite directions. Right: The spacecraft characteristics as proposed (note: the launch date has already been deferred to 2017).

MIRAX does not only provide unprecedented possibilities in timing studies and very unique imaging characteristics, it also overcomes *INTEGRAL*'s disadvantage of irregular pointed observations by conducting the very **first scanning survey** of the southern Galactic plane and Galactic bulge **with coded aperture imaging**.

3.2. Scientific motivation

MIRAX will have its focus on studying SN Remnants (SNRs) and BHs in Giant Molecular Clouds (GMCs), the population of compact objects in the Bulge and southern Galactic plane, the accretion mechanisms onto NSs and the jets from BHs as well as magnetars, AGNs and short GRBs. The major science objectives are displayed in Table 3.1.

Table 3.1.: Overview of MIRAX’s science objectives. The advanced *LIGO*, mentioned in the last row, will be a observatory, able to detect NS-NS binary systems up to 445 Mpc (operation start ~2014). For more information see <https://www.advancedligo.mit.edu/>.

goals	science objectives	MIRAX contribution
hard X-ray survey of the Galactic bulge and southern Galactic plane	population of compact objects in surveyed regions	clarify origin of ~half of <i>INTEGRAL</i> ’s newly found sources and discovery of new ones by using its continuous cadence to differ between NSs and BHs
	investigate accretion of matter onto NS’s poles	analysis of e.g. cyclotron lines to develop and probe models of such extreme conditions; monitor > 100 mCrab outbursts and fainter
	more detailed knowledge of SNRs and isolated BHs in GMCs	discovery of more SNRs and pulsar wind nebulae and search for (intermediate mass)BHs in dense regions near the spiral arms
time domain astrophysics of high energy	analyse relativistic jets from accretion onto compact objects	complementing combination with radio surveys to cast a glance at the onset of BH transient outbursts
	study X-ray bursts from NSs	better understanding of NS crusts and burst recurrence times by detecting ~ 8000 bursts and 20 superbursts
	monitor the few known magnetars and discover new ones	study behavior of soft gamma-ray repeaters and giant flares
	detailed investigation of AGN variability mechanisms	monitor radio-loud seyferts to further constrain disk/jet relations; observe blazar flares
short GRBs	observations with MIRAX-HXI will complement those of advanced <i>LIGO</i>	test theory of NS-NS and NS-BH binaries, which would produce gravitational waves and electromagnentic radiation, as they merge

This states only a short excerpt of what MIRAX will be able to detect. Its quite unique detector setup (see Sec. 3.3) will not only expand our knowledge of already well-studied sources, but also extend our horizon to new ones.

3.3. Detector setup

The Hard X-ray Imager (HXI) consists of four individual telescopes arranged in a 2×2 -array to enlarge the FOV and keep the cosmic X-ray background component (CMB) on a minimum level. This modular approach also provides a variety of descope options, if needed.

Each of its sub-telescopes is canted 13° away from the center of the FOV and includes a Tungsten coded mask with random pattern and a open fraction of 40% located 0.7 m above the detection plane. The single telescopes have a FCFOV of $25^\circ \times 25^\circ$ each, leading to a combined FCFOV of $50^\circ \times 50^\circ$ of the whole HXI and a PCFOV of $70^\circ \times 70^\circ$.

Several **shielding layers** surround the HXI and each of the four sub-telescopes. The shielding consists of four sub-layers made of aluminum (Al), copper (Cu), tin (Sn) and lead (Pb), arranged in that order from the inside to the outside. It further comprises two sections in terms of vertical distances, where the individual layers have different thicknesses with the lower section reaching up to 43 cm above the detection plane. Fig. 3.3 shows the four sub-telescopes assembling the HXI and specifies the individual shielding layers.

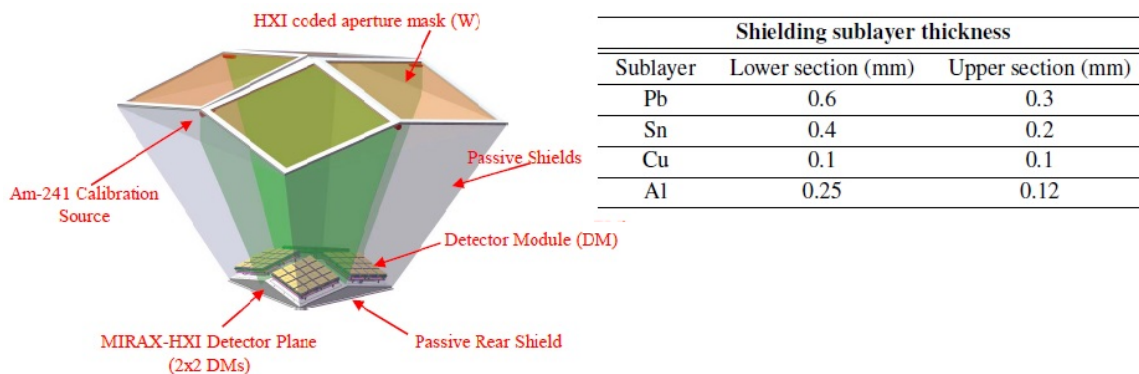


Figure 3.3.: Left: Arrangement of components within the HXI. Right: Thicknesses for the respective shielding layers taken from Castro et al. (2012).

The position sensitive **detection plane** of each sub-telescope is called Detector Module (DM) and its most basic component is a Detector Crystal Unit (DCU). A 2×2 -array of such DCUs make up a Detector Crystal Array (DCA), and four of which are mounted on an event logic board to build a Quad Detector Module (QDM). Finally a DM comprises a 2×2 -array of QDMs corresponding to 64 DCUs (see Fig. 3.4).

The currently most sophisticated material for high energy radiation detectors is Cadmium Zinc Telluride (CZT) which was also used for *NuSTAR* (Rana et al., 2009) or BAT on *Swift* (Barthelmy et al., 2005). CZT-detectors are semiconductors, so they behave much like CCDs, except that they are not read out by transferring charge along columns, but rather by reading out each pixel individually. It further is a material with a high atomic number, providing very good photo efficiency, and its relatively wide band gap avoids extensive cooling, which not only saves money in terms of mass payload, but also potentially increases the missions lifetime, by reducing the amount of required consumables that would otherwise have been needed for cooling. It also shows very good resolution for spectroscopy and positioning purposes and possesses a high sensitivity and good imaging characteristics in general (see for instance Ramsey (2001) or Garson et al. (2006) for more details) and further a much better QE compared to CCDs due to its higher cross-section.

Each DCU will be made of square CZT-pixels with a side length of 0.6 mm and whole DCU dimensions of $19.5 \times 19.5 \times 5.0$ mm. The gap between neighboring DCUs in a 2×2 -array will

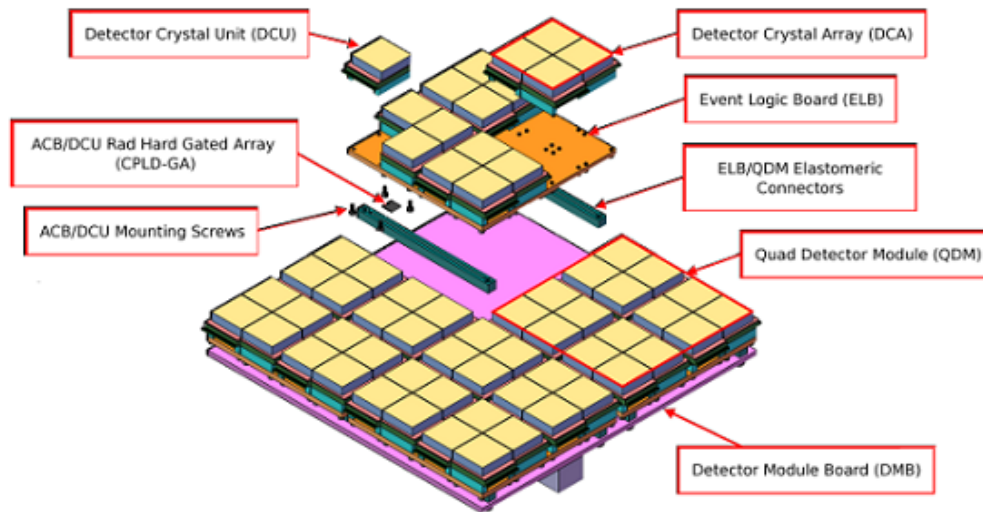


Figure 3.4.: Partitioning of one DM into its sub-modules: DCUs, DCAs and QDMs

be 0.4 mm wide, and the gap between two DCAs will have a size of 6.2 mm.

Throughout the calibration procedure on ground, first each DCU will be calibrated and screened, and then again after the assembly, each of the DMs will be calibrated by three radioactive sources. In space an americium-source provides photons to be able to crosscheck the gain and offset values of all DMs during the mission.

The transparent pixels of the **aperture** pattern will be created by a chemical etching process with a basic grid size of 1.1 mm squares. It will have a thickness of 0.3 mm and overall dimensions of 48.6 cm \times 48.6 cm, leading to a total of 195 000 mask pixels, where 25 000 of which are lying within the detector region. This relatively high amount of aperture pixels favors a random pattern as the pattern of choice, permitting a dynamic range⁴ of ~ 400 . The around 9 times larger coding area of the mask, compared to the detection plane, also meets the requirement of the $25^\circ \times 25^\circ$ -sized FCFOV of each sub-telescope. Furthermore, coding noise will not be posing a problem, and systematic noise will be averaged out due to the continuous scanning mode operation, leading to a sensitivity nearly limited like Poisson-noise. The material used for the aperture plane will be Tungsten, which allows the manufacturing of very fine pixelated patterns⁵ and serves as a overall efficient X-ray modulator due to its inherent atomic structure⁶. The opaque aperture pixels will only have a throughput of less than 10% at energies below 140 keV.

The data collected by the HXI will be sent from MIRAX down to the Brazilian ground station as event mode telemetry packets, meaning that each event will be recorded and sent with its individual pixel position, photon energy, detected depth and time. It then will be forwarded to the MIRAX Missions and Control Center (MOCC) where it is distributed to the MIRAX Science Operations Center (SOC) sites to be archived and made public.

⁴The dynamic range is the ratio of the brightest to the faintest features in an image. Typical values for graphic displays are ~ 300 up to ~ 1000 and for the human eye around 10 000 (from: http://www.communicatingastronomy.org/cap2007/talks/071010_01/HurtDynamicRange.pdf)

⁵Such fine pixelization has already been used for the *ProtoEXIST1* balloon borne experiment as described by Allen et al. (2010).

⁶Tungsten has high values for atomic number, density and tensile strength.

Chapter 4

Software simulation

In the following, the implementation of a software simulation package for coded mask imaging will be described that builds the main concern of this thesis. It is completely based on modules C. Schmid of the Dr. Karl Remeis Observatory (Bamberg) had already developed and therefore uses the SIXTE-environment as described by Schmid (2012). The major challenge was to refine the modules to adapt them for the MIRAX-HXI (see Sec. 4.2) and to extend the cross-correlating based reconstruction to a faster approach using the fast fourier transform (see Sec. 4.1.4).

The software was completely written in C and uses the standardised Flexible Image Transport System (FITS¹) data format, which was especially developed for the storage of scientific data in astronomy and is widely used. Each module is supplied with the required input files and data, by using the Parameter Interface Library (PIL²) and its par-files, which can be changed easily and contain all the information accessible for each module.

It is thought to serve for feasibility studies for MIRAX, and hence will be refined over time, but it can also be used for other coded mask systems, since most of the necessary detector specifications are kept variable.

4.1. Simulation chain

The principal software simulation chain comprises four sub-modules as depicted in figure 4.1. Each module produces a list, i.e. a FITS file that functions as input for the succeeding program-module, starting with the respective X-ray source catalog and going over the generated photon-, impact- and event-list. The final result is a sky image, as the implemented detector would see it.

4.1.1. Photon generation

The photon generation module was originally developed for simulating input data in view of software tests (Schmid, 2008) in advance of the eROSITA³ satellite mission and it was completely adopted for this simulation. It supplies the succeeding modules with a sample of individual photons that possess realistic physical properties and are based on real measured

¹see <http://heasarc.gsfc.nasa.gov/docs/heasarc/fits.html> for more information

²<http://heasarc.gsfc.nasa.gov/lheasoft/headas/pil/>

³extended ROentgen Survey with an Imaging Telescope Array

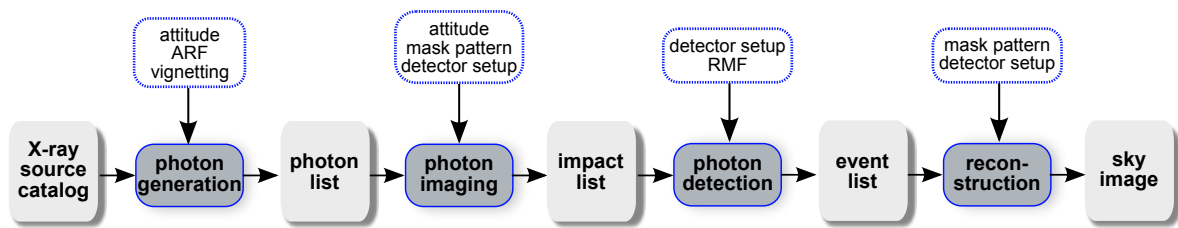


Figure 4.1.: Software simulation pipeline: program-modules are color-coded with a darker background inbetween the respective in-/output lists. The detector-specific input variables are labeled above.

source distributions. The input source catalog utilizes the SIMPUT⁴ data format, in which detailed information on spectral shapes, lightcurves, spatial source dimensions and other characteristics is provided in a standardized way.

Only photons from those sources are selected that are within or near the FOV according to the telescope’s attitude, and a circular shaped mask and detection plane. This approach saves a lot of computational time, if the considered telescope has a very narrow FOV. For MIRAX with its very wide FOV excess photons are generated due to its smaller square shaped configuration, which are then rejected in the imaging module. Further, only those photons are passed on to the photon imaging that still reach the mask plane, after the vignetting has been regarded.

Vignetting

The vignetting describes the effect that the effective area decreases for larger off-axis angles. Thus far off-axis photons are more likely not reaching the mask plane than those nearer the on-axis direction, where all incoming photons are selected to enter the mask plane.⁵ Additionally the number of photons is also reduced by the Ancillary Response File (ARF⁶), which accounts for the following effects:

ARF

In general the ARF considers detector inherent efficiency restrictions. Any used detector will vary in its sensitivity for different energy regions, which can be described as a response matrix with entries that may regard any detector specific sensitivity dependency. Also the transmission of the detector window or of filters and vignetting effects (not so for the HXI; vignetting is implemented separately) may be included. The ARF utilizes the QE as described in Sec. 2.1.3 based on an approximation of a 5 mm CZT-layer, corresponding to the height of one detector pixel. More detailed information on dead layers e.g. from the detector window are not yet included, but will be as soon as they are available. The effective area used for the computation of the ARF (see Fig. 4.2) is comprised by the amount of all transparent mask pixels, which equals 40% of the overall mask plane for MIRAX.

⁴For definition of the SIMPUT-format see: <http://hea-www.harvard.edu/HEASARC/formats/simput-1.0.0.pdf>

⁵The vignetting effect is also present in other types of X-ray telescopes, e. g. those based on grazing incidence. Shin & Sakurai (2003) give an example for modeling and studying vignetting for a soft X-ray telescope.

⁶The definition of the ARF follows the document: http://heasarc.nasa.gov/docs/heasarc/caldb/docs/memos/cal_gen_92_002/cal_gen_92_002.pdf.

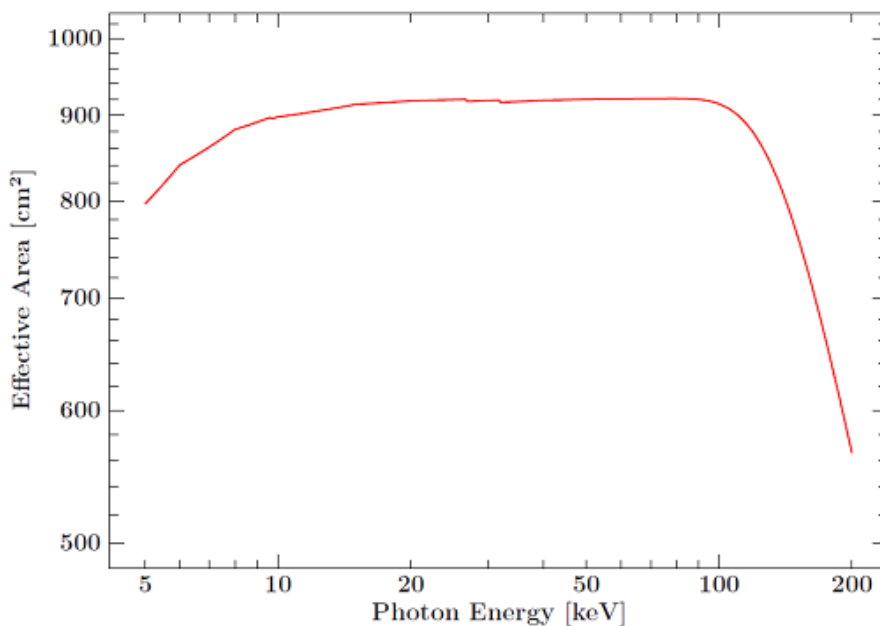


Figure 4.2.: ARF as used for MIRAX’s energy range with contributions from absorption in the CZT-material. At low energies X-rays can not penetrate deep enough to be absorbed within the material and at high energies their absorption length increases strongly, hence the decline in the ARF. (Credits: C. Schmid)

Although the effects described by the ARF would, from the logical order of the detection mechanism point of view, contribute far later in the simulation process, they are already included in the photon generation, since the fewer photons the algorithm has to process, the faster it gets. The photon generation module produces a output photon list as depicted in Fig. 4.3 with information on the arrival time and direction of origin given as declination (DEC) and right ascension (RA) of each photon, and also on its energy as derived from its source’s initial spectrum and the instrument’s effective area.

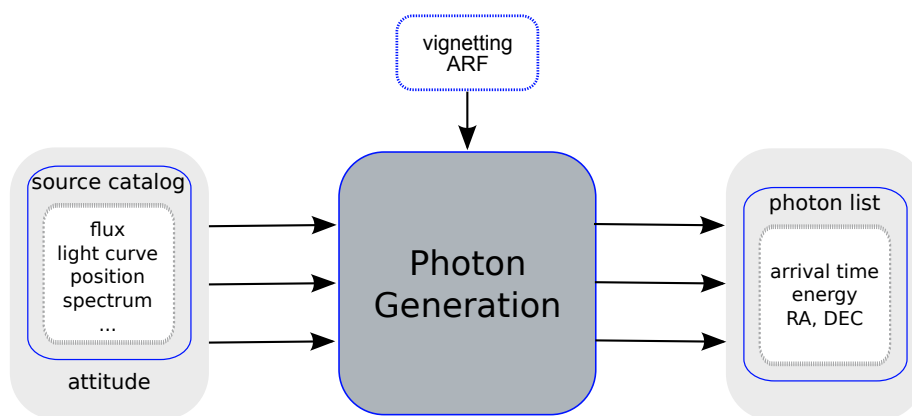


Figure 4.3.: Schematic illustration of input and output data of the photon generation module. The output list contains values for the arrival time, energy and direction of origin of each individual photon and serves as input for the imaging module.

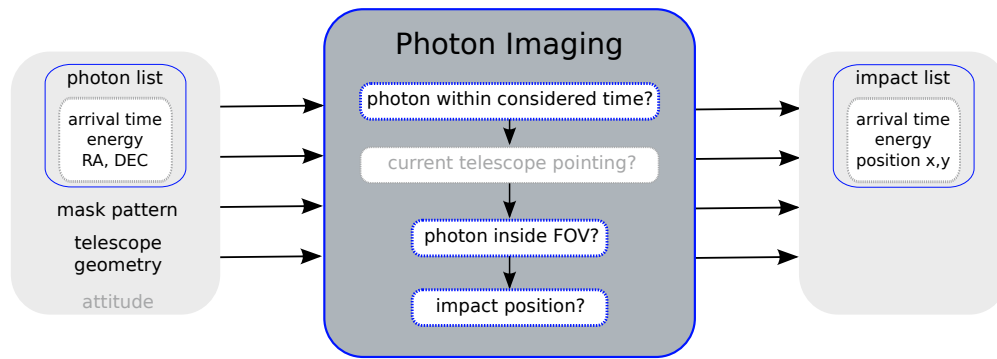


Figure 4.4.: Schematic illustration of input and output data of the imaging module. The lighter shaded attitude indicates that this module can already handle attitude-files, but for the whole simulation it is not yet implemented. Each photon has to follow the depicted steps and may eventually be registered with arrival time, energy and position at the detection plan in meters.

4.1.2. Imaging

The imaging module was slightly modified and extended in order to meet the requirements for the MIRAX-HXI. The changes comprise mainly the determination of the exact FOV, the implication that all photons travel through transparent mask pixels and the exclusion of those photons that would miss the detection plane and hit the detectors walls. The main imaging steps are shown in Fig. 4.4 together with the input and output information. The attitude-file is depicted in pale gray, since the imaging module can already work with attitude-files, but the reconstruction so far only uses pointed observations (see chapter 5). For a pointed observation, the RA and DEC values are provided by the user in the par-file. The program then determines an unit vector in pointing direction and spherical coordinates as follows:

$$\vec{n}z = \begin{pmatrix} \cos(\delta) \cos(\alpha) \\ \cos(\delta) \sin(\alpha) \\ \sin(\delta) \end{pmatrix},$$

where α and δ denote the right ascension and declination respectively and with $\vec{n}z$ the other two perpendicular directions $\vec{n}x$, $\vec{n}y$ of the telescope coordinate system are set. If an attitude-file is specified by the user, the coordinate system is determined for all its entries and if, during the imaging process, telescope coordinates are needed that are not explicitly given by the file, they are interpolated accordingly in between the two nearest pointings.

The simulation handles each photon individually, starting with the verification that the current photon lies within the requested exposure time interval. The photon's next obstacle is the telescope's FOV, which is given by the maximum possible angle due to the mask and detector dimensions ($\text{mask}_x \times \text{mask}_y$ and $\text{det}_x \times \text{det}_y$) and their separation, as illustrated in red in Fig. 4.5. The angle ϕ is simply determined by using the tangent and applying Pythagoras' theorem:

$$\begin{aligned} \tan(\phi) &= \frac{a}{d} \\ &= \frac{\sqrt{\left(\frac{\text{mask}_x}{2} + \frac{\text{det}_x}{2}\right)^2 + \left(\frac{\text{mask}_y}{2} + \frac{\text{det}_y}{2}\right)^2}}{d} \\ &= \frac{1}{2d} \sqrt{(\text{mask}_x + \text{det}_x)^2 + (\text{mask}_y + \text{det}_y)^2}, \end{aligned}$$

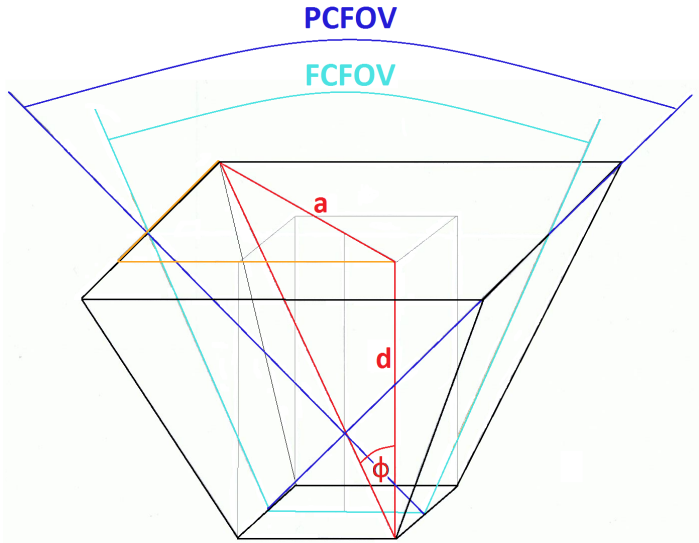


Figure 4.5: Illustration of the maximum angle allowed for incoming photons. Right formula can easily be obtained by using the red and orange triangles. The blue lines show again the definition of the FCFOV and the PCFOV.

where d denotes the mask-detector separation and the indices x and y the respective width and depth. Therefore ϕ reduces for square mask and detector configurations to⁷:

$$\phi = \arctan\left(\frac{\sqrt{2}}{2d}(\text{mask} + \text{det})\right). \quad (4.1)$$

After neglecting those photons, which do not fulfill Eq. 4.1, each photon has to enter the mask plane and as stated before (Sec. 4.1.1), all photons are passing transparent pixels, which are selected randomly. As soon as the photon has been associated with a mask pixel, its current position is determined from:

$$(\text{mask pixel} - \text{reference pixel} + 0.5 + \text{random number}) \cdot \text{pixel width} + \text{value of reference pixel}.$$

The reference pixel is the origin of the coordinate system, which corresponds to the center of the mask plane to be able to align it perpendicularly above the center of the detection plane (as illustrated in Fig. 4.5). The 0.5 accounts for the fact that the reference pixel value is given with respect to its middle in the FITS-file⁸, so to shift to its left border one has to add 0.5. The adding of a random number ranging from 0 to 1 then distributes the passage of the photon randomly within the respective pixel (see Fig. 4.6) and the following multiplication with the width of one pixel leads to the position in meters, which can range from $-\frac{\text{mask}}{2}$ to $\frac{\text{mask}}{2}$ due to the choice of origin. The photon's trajectory is then projected downwards to the detection plane, by applying the vector addition:

$$\overrightarrow{\text{pixel}}_{\text{det}} = \overrightarrow{\text{pixel}}_{\text{mask}} - d \cdot \overrightarrow{\text{pho.dir}} = \overrightarrow{\text{pixel}}_{\text{mask}} - d \cdot r \begin{pmatrix} \cos(\alpha) \\ \sin(\alpha) \end{pmatrix}, \quad (4.2)$$

⁷Throughout the simulation, the more general formulation is used, so it could also be applied to rectangular configurations.

⁸The first pixel in the FITS-file is assigned to the number '1', where its left border starts with 0.5, its middle is indicated with 1 and its right border corresponds to 1.5. The program refers to the first pixel with the value '0', and has hence to be shifted.

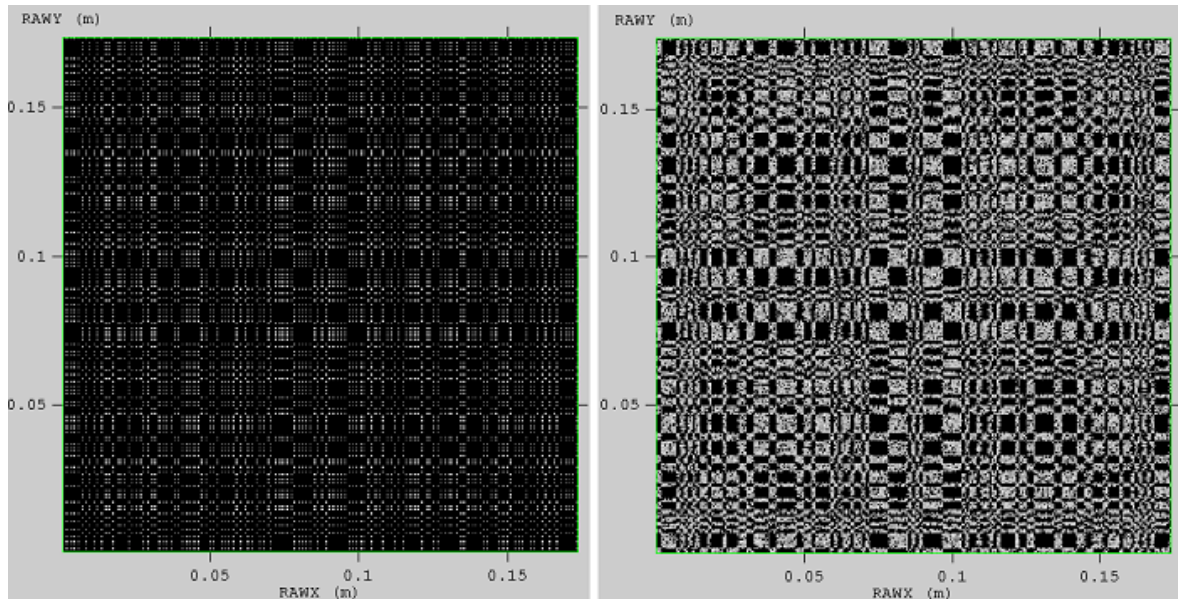


Figure 4.6.: Comparison between impacts that only hit the center of the respective mask pixel (left side) and a random distribution on the right. The x and y axes denote the impact position in meters at the detection plane as given in the impact list. For this illustration a MURA mask, with only one source centered above it, has been used.

where $\overrightarrow{\text{pho_dir}}$ describes the photon-direction in polar coordinates and is determined with respect to the telescope's \vec{n}_x and \vec{n}_y axes. Its magnitude r comprises the angle α within the mask plane.

Arrived at the detection plane, the coordinate system is shifted to one of the corners in order to get only positive values for the photons position, which are then compared to the overall detector dimensions to exclude those that would not hit the detector, but are absorbed before by its walls.

4.1.3. Detection

The purpose of the detection module is to assign each photon's impact position to a valid pixel within the detection plane. The former version was modified in order to mirror MIRA-X's CZT-detection plane with its gaps due to the manufacturing process inbetween the arrangement of DCU's and DCA's as described in Sec. 3.3. The implementation as well as the result of that HXI specific characteristic is being reviewed in detail in Sec. 4.2. The detector setup, as mentioned in Fig. 4.7, therefore comprises the detector-width in pixels⁹, the width of one pixel as well as the values for a DCU and the gap between two DCU's and two DCA's.

RMF

The Redistribution Matrix File (RMF) labeled above the detection module in Fig. 4.7 gives the probability that photons of certain energy values are detected within a certain channel. This detected energy is not exactly the same as the photon's initial energy value, since lots of effects affect the detector's ability to detect the charge deposited by incoming radiation correctly, as already roughly outlined in Section 2.1.3. Thus the number of detected electrons

⁹which has to include the summed values of the gaps as well, although they are not really pixels;

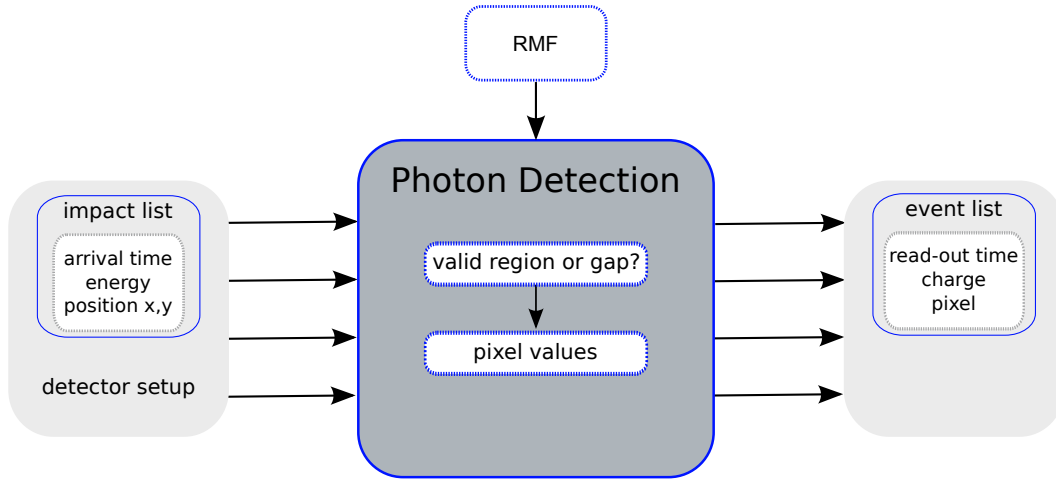


Figure 4.7.: Schematic illustration of input and output data of the detection module. The photon’s position in meters is converted to pixel coordinates, if it does not hit one of the gaps. The output event list serves as input for the reconstruction module.

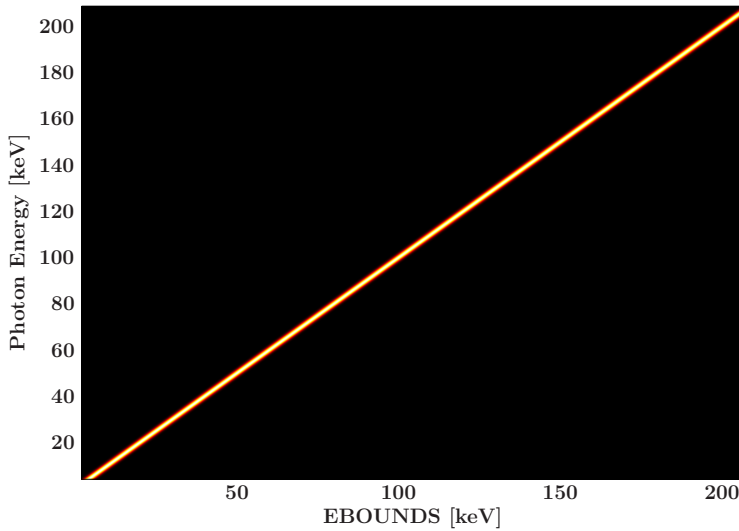


Figure 4.8: RMF as currently used for MIRAX. The y -axis denotes the photon’s initial energy and the x -axis the detected value. As the diagonal of the RMF is broadened, the value after the detection will vary within the energy resolution. With the inclusion of a more detailed model, the RMF may look more extended in some regions, e.g. for low energies due to partial absorption at the detector window and it will further include a minor diagonal corresponding to the lost escape peak photons. (Credits: C. Schmid)

may vary due to statistical fluctuations and may not equal the predicted number of generated electrons due to the photon’s energy and the needed work function (Eq. 2.2) exactly. Further photons may be partially absorbed at the detectors surface and therefore produce too less charge, or they may even lead to excitation followed by de-excitation in some detector atoms, which will also cause charge loss due to escaping photons during the transition back to a lower shell. The detector response therefore comprises continuous energy values that model the respective mechanisms and have to be redistributed to discrete channel values in the RMF, like¹⁰:

$$\text{RMF}(Ch, i) = \frac{\int_{E_{i-1}}^{E_i} R(Ch, i) dE}{E_i - E_{i-1}}. \quad (4.3)$$

¹⁰see: http://heasarc.nasa.gov/docs/heasarc/caldb/docs/memos/cal_gen_92_002/cal_gen_92_002.pdf

In the ideal case this matrix would equal the identity and all photons would be detected with their initial energy value, whilst in the real case the main diagonal is somewhat extended and shows different features. The RMF used for MIRAX right now is very basic (see Fig. 4.8), but will be extended to a more detailed and realistic version in the near future.

In order to determine the total of observed events in a certain channel Ch , one has to integrate over the RMF, representing the energy redistribution as stated above, the ARF (Sec. 2.1.3), representing the detector efficiency and the original source's spectrum S for the observing time T (Arnaud & Smith, 2011):

$$\text{Events}(Ch) = T \int \text{RMF}(Ch, E) \cdot \text{ARF}(E) \cdot S(E) dE. \quad (4.4)$$

The detector setup shall be provided via the XML-format to the module, which allows a flexible formulation of detector specific input parameters, such as the geometry of the system and parameters concerning the functionality of the detector like its read-out mode. This becomes especially important, if different types of instruments are to be managed, since it avoids the adjustments in the program code itself.

The detection process simply determines for each individual photon's impact coordinates given in meters, the respective pixel value in the detection plane. It only associates those photons with pixels that do not arrive at the position of a gap. The output is then a list of events that comprises the photon's arrival time, its charge and the respective pixel (Fig. 4.7) and will be processed further by the following reconstruction module.

4.1.4. Reconstruction

For the reconstruction module only the framework and the very basic cross correlation approach were retained. The necessary input data and the module's basic steps are shown in Fig. 4.9.

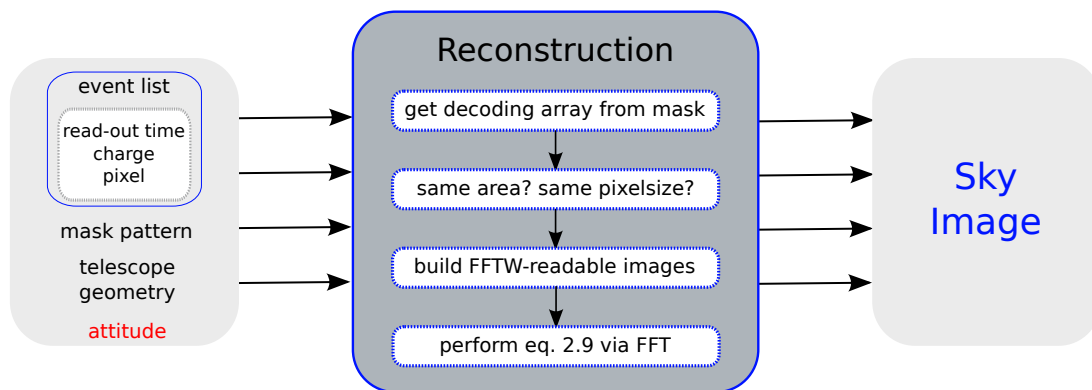


Figure 4.9.: Illustration of input data required and basic decoding steps performed in order to obtain a sky image with a source distribution as MIRAX-HXI would see it. The attitude-file is written in red, since currently only pointed observations are to be reconstructed by the implemented algorithm.

In order to obtain a sky image, the decoding equation (2.9) has to be performed, which can either be done by directly computing the summations or by employing a Fast Fourier Transform (FFT) algorithm which, as the name suggests, can save a lot of computational time. Both approaches shall be explained, but the focus is clearly with the FFT. The main

reason for keeping the time consuming summations was to be able to crosscheck the FFT with it during the development and to compare both methods for their duration.

For the direct computation of Eq. 2.9, four loops are needed all in all, where the outer two range over the dimensions of the output sky image, and the inner two consider each possible shift of the mask over the detection plane. The latter use varying values for the beginning and end of the respective loop in order to compare different parts of the decoding array, derived from the mask pattern, with the detected distribution. That is part of why this method is such time consuming, especially for larger arrays.

FFT: As stated in Table 2.1, the correlation between signals of any kind can be described in Fourier space, as the multiplication of their Fourier Transforms (FTs), with one of them complex conjugated. The Discrete FT (DFT) Y of an array X in one dimension is defined as¹¹

$$Y_k = \sum_{j=0}^{n-1} X_j e^{-2\pi i k j / n}, \quad (4.5)$$

where n denotes the length of X and i is the imaginary unit. A DFT requires a number of operations that is $\propto n^2$, which is obviously not very time-saving¹². The FFT as discovered by Cooley & Tukey (1965) makes use of redundant aspects within the DFT and can hence speed up the calculation to only $\propto n \log_2(n)$ needed operations. This goes as follows: The summations are split into their even and odd parts, which gives:

$$\begin{aligned} Y_k &= \sum_{j=0}^{\frac{n}{2}-1} X_{2j} e^{-2\pi(2j)ki/n} + \sum_{j=0}^{\frac{n}{2}-1} X_{2j+1} e^{-2\pi(2j+1)ki/n} \\ &= \sum_{j=0}^{\frac{n}{2}-1} X_{2j} e^{-\frac{2\pi i}{n/2} jk} + e^{-\frac{2\pi i}{n} k} \sum_{j=0}^{\frac{n}{2}-1} X_{2j+1} e^{-\frac{2\pi i}{n/2} jk} \\ &= A_k + \mathbf{W}^k B_k, \quad \text{where } A_k = \sum_{j=0}^{\frac{n}{2}-1} X_{2j} e^{-\frac{2\pi i}{n/2} jk}, B_k = \sum_{j=0}^{\frac{n}{2}-1} X_{2j+1} e^{-\frac{2\pi i}{n/2} jk} \text{ and } \mathbf{W}^k = e^{-\frac{2\pi i}{n} k}. \end{aligned} \quad (4.6)$$

If one then computes the same for the DFT's periodic frequencies, $Y_{k+\frac{n}{2}}$ can be written as:

$$Y_{k+\frac{n}{2}} = A_k - \mathbf{W}^k B_k. \quad (4.7)$$

Thus Y_k and $Y_{k+\frac{n}{2}}$ can be determined by calculating the A_k and B_k in $n/2$ steps each, which leads to a total of $\sim n^2/2$ calculations and is already half the number of computations as required for the bare DFT's. If the same method is used in a recursive formulation to further reduce each of the $n/2$ DFT's to be computed, the problem can subsequently be reduced to one of half the former size, given that it can be written as a power of 2 (2^n). The overall computations needed are then proportional to a number of $n \log_2(n)$. There are many different

¹¹This is, how the FFTW-library (see later) computes an 1d forward transform.

¹²The exact dependency arises by picturing a DFT as n^2 complex multiplications and $n(n-1)$ complex additions, as it can be written as a complex $n \times n$ -matrix multiplied with a complex n -dimensional vector: $Y_k = \sum_{j=0}^{n-1} X_j \cdot \mathbf{W}^{jk}$. If one uses further that $\mathbf{W} = e^{-2\pi i/n}$ has only entries of '1' in the first row and column ($e^0 = 1$) and divides the complex operations in the corresponding amount of real ones, roughly the n^2 -behavior is obtained.

algorithms available, which may use different approaches, but all somehow make use of the DFTs inherent redundancies to speed up the calculations.

To implement a FFT algorithm the FFTW-library¹³ was used. FFTW defines the 2-dimensional DFTs as

$$Y_{k_{1,2}} = \sum_{j_1=0}^{n_1-1} \sum_{j_2=0}^{n_2-1} X_{j_{1,2}} e^{-2\pi i k_1 j_1 / n_1} e^{-2\pi i k_2 j_2 / n_2}, \quad (4.8)$$

for a forward transform, and likewise:

$$Y_{k_{1,2}} = \sum_{j_1=0}^{n_1-1} \sum_{j_2=0}^{n_2-1} X_{j_{1,2}} e^{2\pi i k_1 j_1 / n_1} e^{2\pi i k_2 j_2 / n_2}, \quad (4.9)$$

for a transform backwards. Both of them correspond to unnormalized transforms (no factor in front), thus the result has to be divided by the product of the array's dimensions if it has been transformed forwards and backwards again. In order to work with FFTW the following principle steps have to be performed:

- memory-allocation for the input and output arrays
- creation of a FFTW-plan
- execution of the FFT
- deallocation of the plan and the input and output arrays

The length of the input array is arbitrary and FFTW uses the plan to determine which way represents the fastest computation. It also provides functions for handling the memory and for many different FFT applications.

Things that have to be kept in mind, when using FFTW are:

- the input array has to be given in row-major order
- normalization may be required
- padding of the input arrays may be needed

The row-major format in principle is a 1-dimensional representation of a 2-d array. A 2-d array is usually accessed by two variables x and y , like `Array[x][y]`, which can be pictured as the two indices of a matrix element or the columns and rows in a table. The row-major format simply means that the array is stored row-wise, meaning for subsequent memory locations the first index (the row) varies slowly and the second (the column) varies in a fast pace. So, an array, which was accessed like '`Array[x][y]`' had to be rearranged to be accessible like `Array[x + dimensionx · y]`.

The padding applied to the input arrays will be discussed in Section 4.2. Appendix B shows an example of how the FFT has been used in the function `FFTofArray_1d`.

Image reconstruction: The reconstruction module first derives a decoding (or reconstruction) array G after Eq. 2.14 from the mask pattern, which may have to be re-binned

¹³see <http://www.fftw.org/> for details.

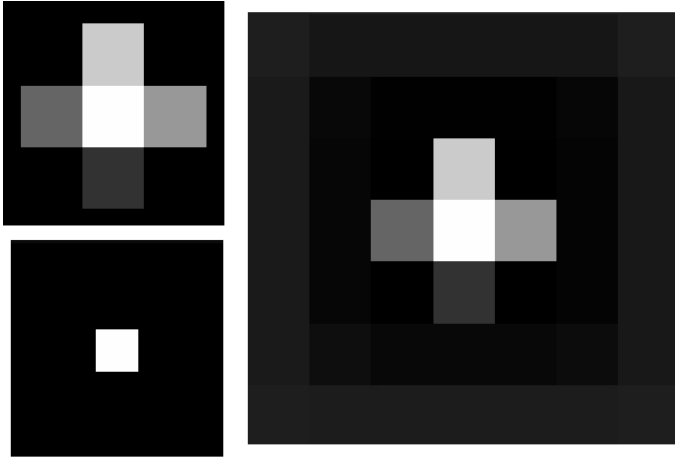


Figure 4.10: Test of intensity distribution after reconstruction. Top left: 3×3 - test event image with five different intensity values and brightest pixel in the middle. Bottom left: mask with only one transparent pixel in its center and different pixel-size than event image above. A pattern with one hole retains the input image as it functions like the simple pinhole (chapter 2.1). Right: image after reconstruction shows the same intensity distribution.

for the case of different pixelsizes of mask and detector (as is the case for the HXI; see Sec. 4.1.3). It further derives an event array E by summing all the counts per pixel that have been detected for that certain pixel and have been stored with the corresponding pixel values redundantly in the event list before. Both arrays are padded and build the basis for performing Eq. 2.9 by applying the FFT in the following way:

$$\text{Sky image} = \text{FFT}\left(\text{FFT}(E) \cdot \text{FFT}(G)^*\right)^{-1}, \quad (4.10)$$

where the outer FFT^{-1} denotes an inverse FFT and the ‘*’-symbol the complex conjugate. Eq. 4.10 is implemented in the following steps:

- get event and reconstruction array in row-major order
- apply forward transform to reconstruction array
- apply forward transform to event array
- multiply E element-wise with the complex conjugate of G
- apply backwards transform to the multiplied array
- save result as sky image and account for normalization

FFTW stores the real and imaginary part like: `Array[element][0 or 1]`, with ‘0’ corresponding to the real part and ‘1’ to the imaginary. Thus the multiplication of E and G is obtained as:

$$\begin{aligned} \text{MultipliedArray}[\text{element}][0] &= E[\text{element}][0] \cdot G[\text{element}][0] + E[\text{element}][1] \cdot G[\text{element}][1], \\ \text{MultipliedArray}[\text{element}][1] &= E[\text{element}][1] \cdot G[\text{element}][0] - E[\text{element}][0] \cdot G[\text{element}][1]. \end{aligned}$$

In order to test whether the intensities are retained correctly during the reconstruction, I used a fake 3×3 - event image with five different intensity values, and a mask with only one transparent pixel in its middle. Fig. 4.10 shows clearly that the output image has the same intensity distribution.

To be able to crosscheck the result after each step in the simulation, a number of test functions were introduced that produce FITS-files and can be used, to monitor exactly, what

happens to each pixel. The test-files include a table for each real and imaginary part produced during the reconstruction. Some of these test images are shown in Fig. 4.11 - 4.12. Six arbitrary chosen source positions given in Table 4.1, served as input and are pictured in the output image in Fig. 4.13.

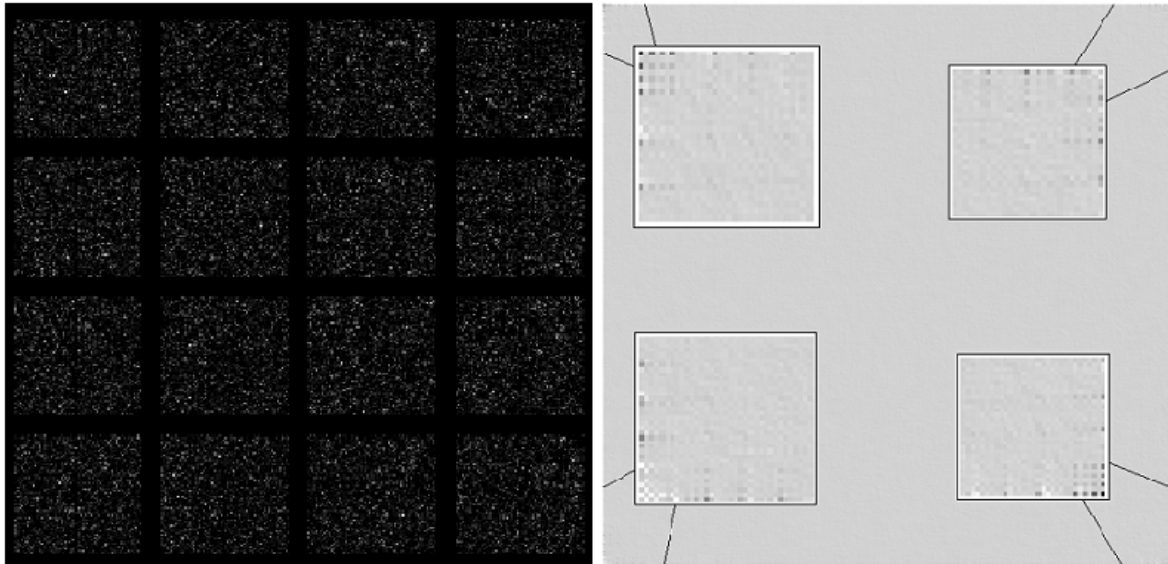


Figure 4.11.: The following figures show some example images of different stages during the reconstruction process as they were used for testing the simulation. Left: detected events, Right: fourier transform of the event distribution with features in the corners. The overall smooth background results from the rather big changes in pixel-values in the event-file, since peaks in the original image appear widespread in fourier space.

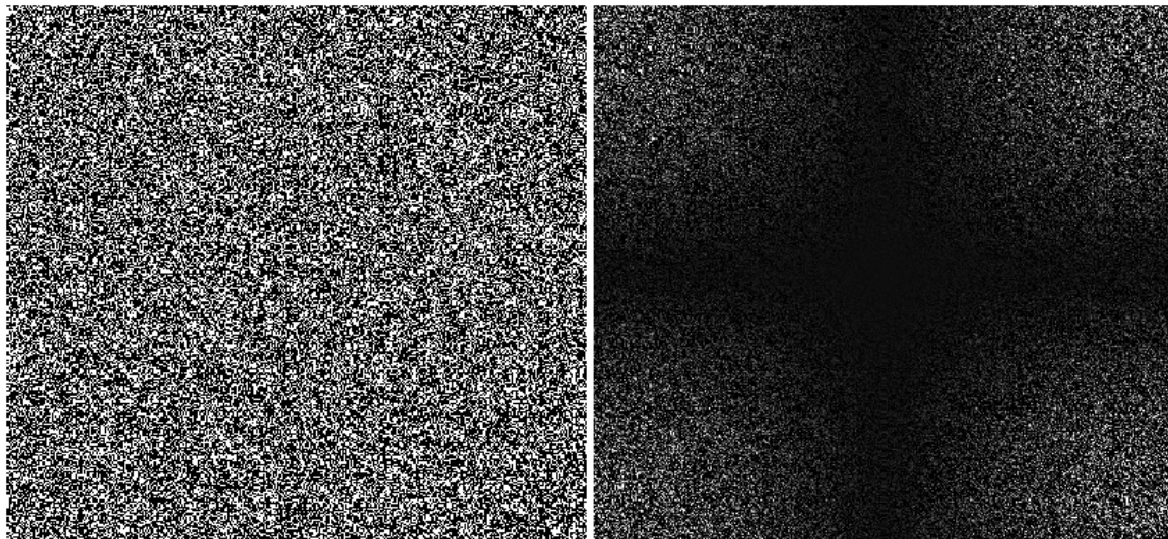


Figure 4.12.: Left: random mask pattern with 40% OF as currently used to approximate MIRAX's aperture. Right: mask pattern in fourier space. These images shall illustrate the astonishing fact that although they seem to bear no resemblance with each other at all, the mask pattern can be correlated to the detected counts as described throughout this thesis, by applying Eq. 4.10 in fourier space and the result actually is Fig. 4.13 with the six recovered source positions.

RA	DEC
-0.8	2.4
1.0	0.5
1.0	1.0
0.0	0.0
1.3	-2.0
-1.5	-2.5

Table 4.1: Arbitrary chosen source positions that were used as input of the whole simulation pipeline as a test example. Fig. 4.13 shows some of the intermediate steps during the image reconstruction and eventually (last image) recovers the stated source positions. The values are listed top to bottom when compared to the image (RA equals the x -direction and DEC the y).

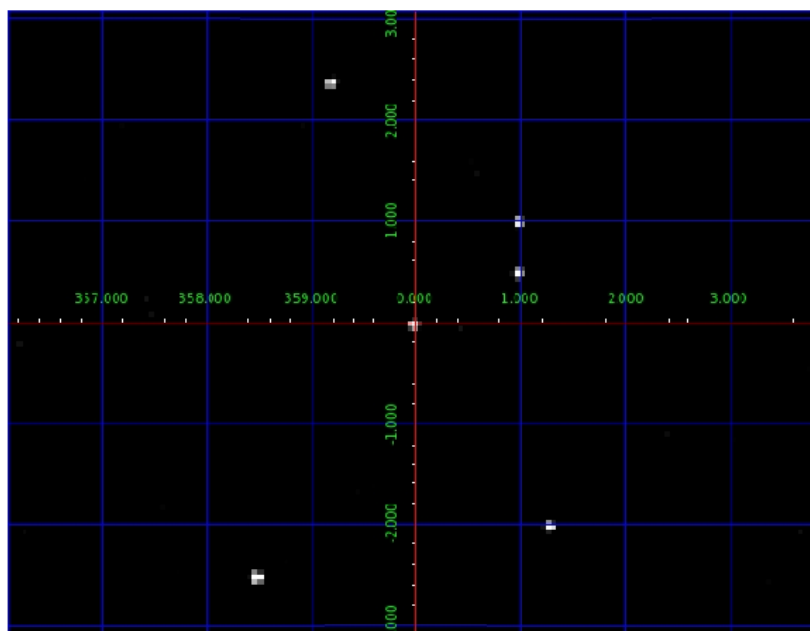


Figure 4.13.: Positions of the six sources listed in Tab. 4.1. They were obtained using the four intermediate steps given by Fig. 4.11 and 4.12.

4.2. Implementation of the MIRAX-HXI

As described in the sections before some adjustments had to be made in the simulation to account for the HXI's specific setup. Especially the detection module (Sec. 4.1.3) and the image reconstruction (Sec. 4.1.4) have been modified to fit the HXI's characteristics. These modifications shall be outlined in the following.

Detector gaps

Figure 4.14 shows a schematic arrangement of the gaps as introduced in Sec. 3.3 and mentioned in Sec. 4.1.3 between the different components in the detection plane. The simulation handles them as if they were real, but empty pixels, which means all photons hitting one of them are discarded by the function `getSquarePixel` described in Appendix B. Figure 4.15 shows the simulated output of the detection module, in which the bigger gaps are clearly visible. The small gaps can be distinguished in Fig. 4.16

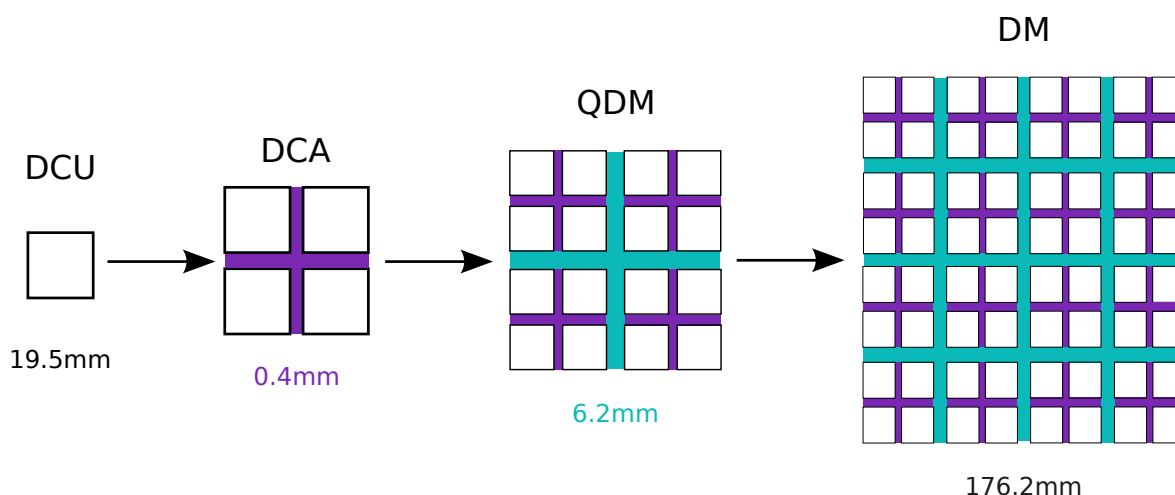


Figure 4.14.: Schematic illustration of the gaps in the detection plane. One DCU has a side-length of 19.5mm, but since one pixels side-length' is 0.6mm which would equal 32.5 pixels per DCU, the number has been reduced to 19.2mm in the simulation, which gives the exact 32 pixels.

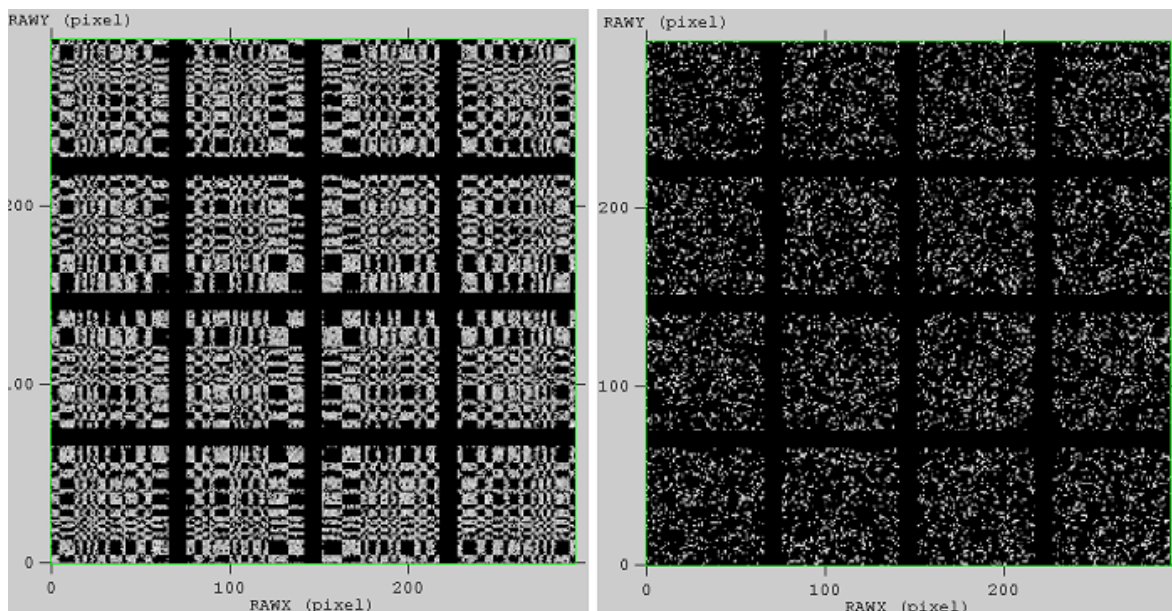


Figure 4.15.: Output of detection module with clearly visible gaps between the DCA's. Those between the DCU's cannot be distinguished, since they are smaller (0.4mm) than the size of one pixel (0.6mm) and the count rate is too low. The left side shows an example of a URA pattern with an OF of 50% and the right a random pattern with 40% transparent pixels, which explains the lower amount of observed counts.

Padding of E and G

Both arrays were padded to the next power of two, meaning they are made twice as large as before. This is achieved by copying their content into a bigger array and leaving the remaining three quarters of it set to zero. Furthermore E and G have to be placed in any

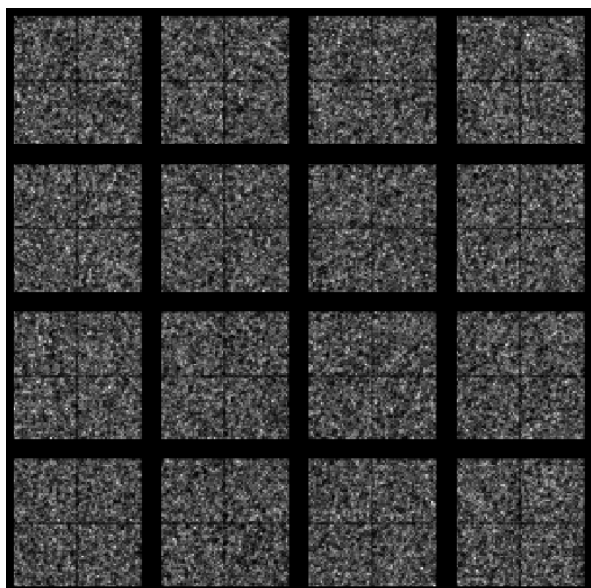


Figure 4.16: At higher count rates also the small gaps between two DCU's are visible. They are still smaller than one pixel, but since that exact pixel row or column is more often 'not hit' at higher count rates, they appear as thin black lines.

mirrored positions, which is due to the FFTW having their zero frequency in the zero-pixel position, not in the middle of the array¹⁴.

Since the detection plane is significantly smaller than the mask plane, the event array is placed in the middle of its respective quarter of the whole padded version of it. Again the leftover pixels are set to zero (see Fig. 4.17 and Fig. 4.18).

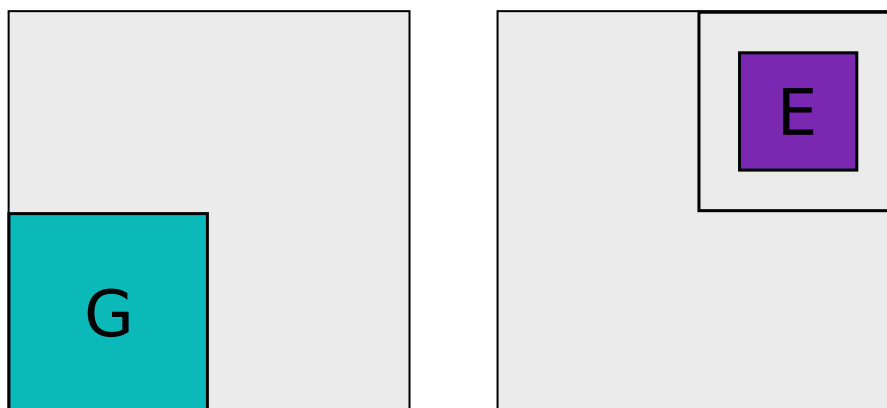


Figure 4.17.: Schematic illustration of the arrangement of the E and G array in their newer enlarged versions. The gray shaded areas are filled up with zeros. For same sized mask and detection planes, E would reach to the black borders in the right image. The placing does not matter, E and G could easily be switched or placed in the top left and bottom right corners.

Re-pixelization

For the different pixel sizes of aperture and detector, two different approaches were used. The first one applies the re-pixelization to the mask array only and bins it to the size of the

¹⁴In general FFTW arranges the positive frequencies starting with zero, in the first half of the array and the negative ones in the second half, but in backwards order. This fact can also be seen in Fig. 4.12.

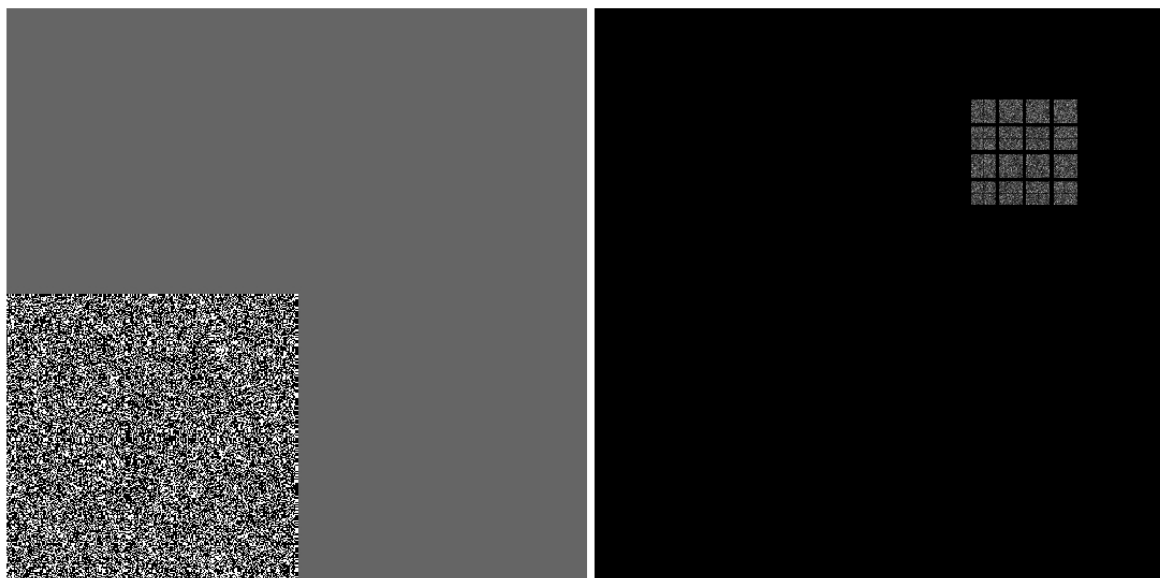


Figure 4.18.: Padding of the real arrays. The proportions fit those of the HXI and the gray area in the left image and the black area in the right one correspond to the padded zeros. The difference in color is due to the fact that the G array also comprises negative values and the color-coding is orientated at the lowest value as to equal the darkest.

detector pixels that is, in the case of MIRAX, 11 mm sized pixels had to be rescaled to 6 mm sized ones. Thus the former $436 \times 436 = 190\,096$ pixels were increased to $799 \times 799 = 638\,401$ ones. Since the mask pixel size of 11 mm is not divisible without remainder by the 6 mm sized detector pixels, the re-pixelized mask grid has to comprise intermediate values and is hence only an approximation. The re-pixelization is performed after the decoding array is build and contains therefore values between the minimum entry of G and ‘1’. The minimum entry of G depends on the OF of the aperture and is for a total of 40% transparent pixels ‘ -0.6 ’.

The function `getReconArray` (see Appendix B) first determines the length of the new re-pixelized reconstruction array, by multiplying the width of the mask (in pixels) with the width of one mask pixel (in meters) and then dividing it by the detector pixel-width (also in meters) and doubling the whole, since G has to be as twice as large due to padding. It then initializes all entries to the minimum value resulting from Eq. 2.14 (-0.6 for the HXI) and determines the absolute difference between it and the value ‘1’ for transparent pixels. `getReconArray` then scans over all former big mask pixels and within each of them, over the new introduced smaller detector pixels. Each of the small pixels can either lie completely within a big pixel, or only partially. If it lies completely in a big one and the big one corresponds to a mask hole, it is set to ‘1’. If only some part of it lies within the current big pixel, the percentage of that part with respect to a whole small pixel is determined and then multiplied with the difference value mentioned above, in the case the big pixel is again transparent. The negative initialized small pixel is then increased by that value, which ensures that only that part of a small pixel that actually lies within a transparent big mask pixel contributes to the transparency. Thus each new small pixel lying at the border(s) of a big one, comprises contributions from all its split-areas and the whole value of it is weighted with the total percentage of transparent area contained in it.

The described scanning is illustrated in Fig. 4.19 and the result can be seen in Fig. 4.20.

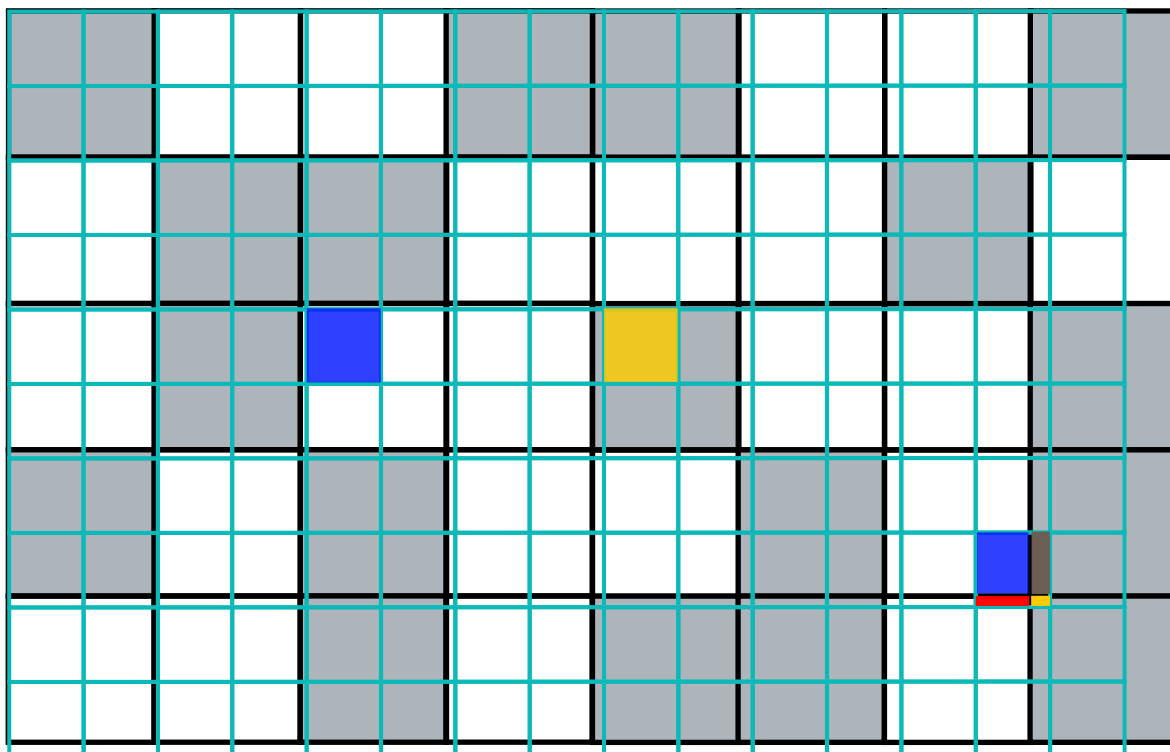


Figure 4.19.: Illustration of the re-pixelization problem, if the mask is re-pixelized to detector size pixels with the current HXI-proportions. The bigger black framed areas show the mask pixels and the smaller light blue framed ones equal those of the detector. Gray shaded regions illustrate opaque aperture elements. The scanning described above starts at the first big pixel and determines all the small split areas lying within it. For a situation like depicted by the yellow one in the middle of the figure the small pixels' value is left unchanged to the negative initialization value, since it lies completely in the bigger opaque one. The blue one left handed from the yellow in contrast, is set to '1', since it is embedded fully in a bigger transparent element. The small colored element at the bottom right corner, is a more problematic case, because it is divided in four split-areas, where the dark gray and yellow parts do not change the opaqueness, but the blue and red parts add with their respective percentage to the negative value and therefore make the whole small pixel more but not completely transparent.

The second approach rescales both arrays E and G to the size of their pixels' greatest common divisor, which is for MIRAX 0.1 mm. That results in $1738 \times 1738 = 3\,104\,644$ pixels for the detector (compared to its former $289 \times 289 = 83\,521$) and whole $4796 \times 4796 = 23\,001\,616$ for the new G array.

The process of re-pixeling the two arrays works much like the one described above, except that no split areas of small pixels inside the bigger pixels have to be determined, since a number of small pixels fits exactly into the big ones now. It has to be kept in mind that when changing the pixel sizes, one has to further change the sky image setup, because the system's angular resolution as given by Eq. 2.1.1 is defined as the angle one mask element subtends at the detection plane.

The resulting sky images of both methods are compared in Fig. 4.21 and show both the correct source positions. The first method has the advantage of being much faster, while the

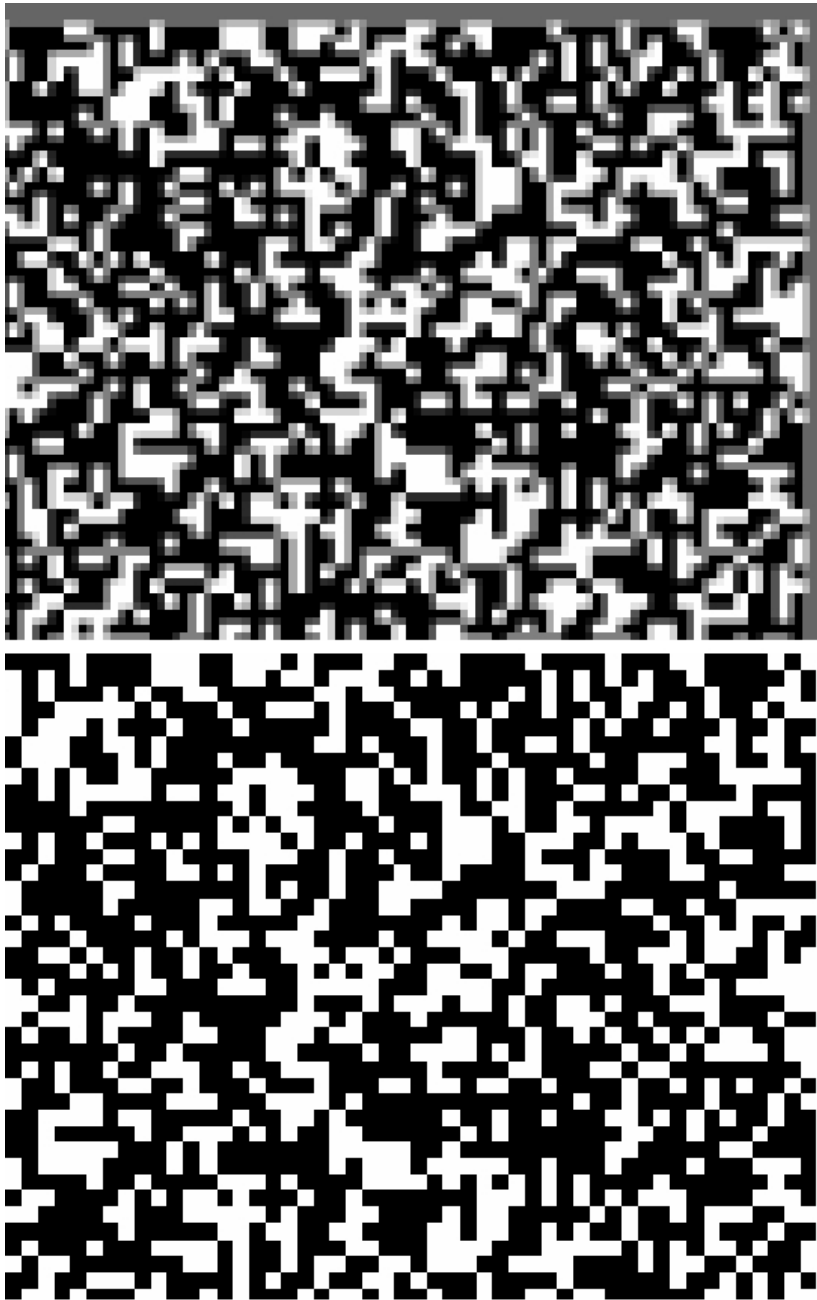


Figure 4.20.: Approach one: mask pattern re-pixelated to the size of one detector pixel (top). The pattern still is very well recognizable, when comparing for example the top right corners of both versions and further the smaller pixel grid is visible. The blurring is due to the fact that the top only resembles an approximation of the real aperture (bottom).

second one produces less pixelated source positions. For a 387 MB photon list file, the first approach needed on average half a minute and the second five and a half minutes, which is more than 10 times longer.

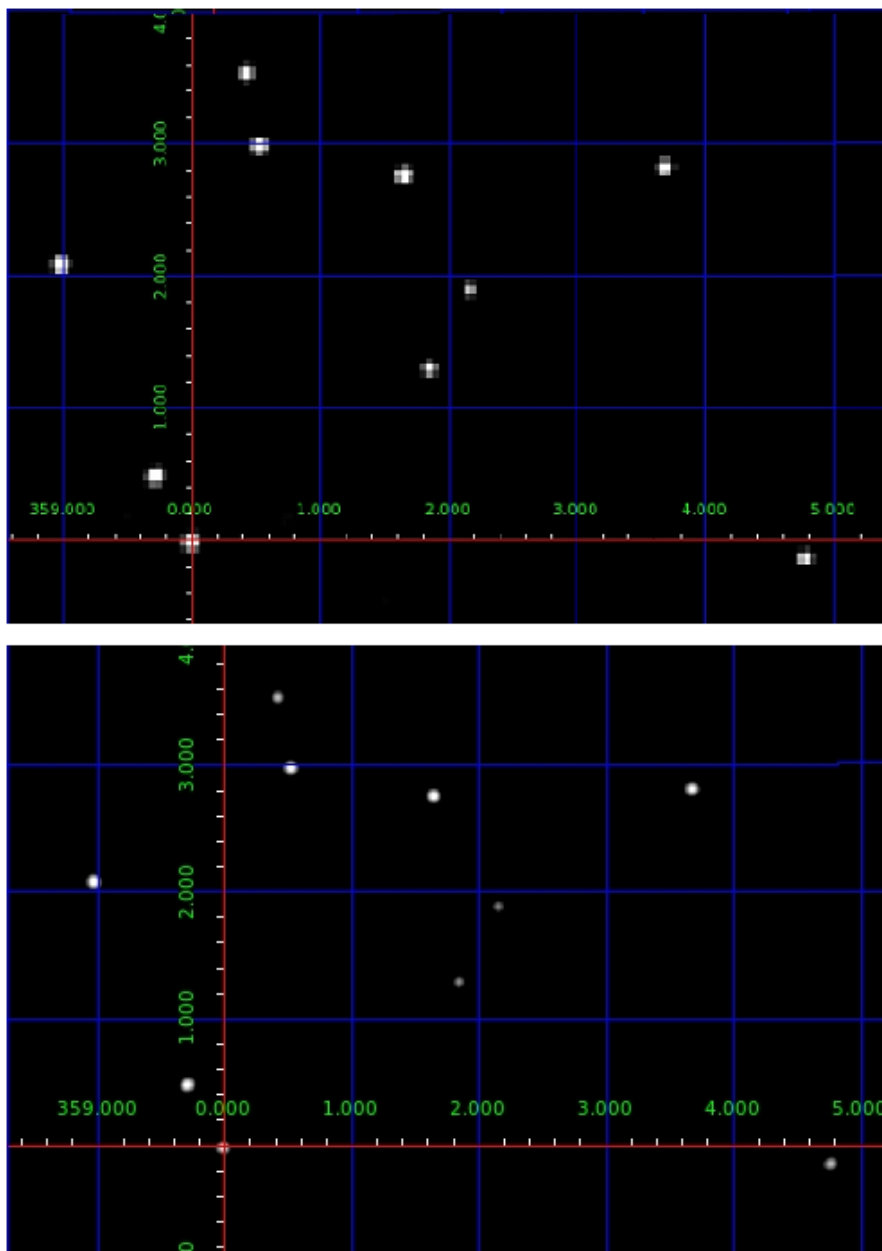


Figure 4.21.: Top: reconstructed sky image with arbitrary chosen source positions via approach one: only the mask pattern is re-pixelated to the detector pixel width. Bottom: both arrays have been re-pixelated to their pixels' greatest common divisor. The source positions are the same, only the top variant shows more pixelated positions, but makes up for that, by far less computation time.

4.3. Results

The event list produced by the first three modules has already been used to do some preliminary estimations on the expected count rates, when observing the Galactic center. Fig. 4.22 and 4.23 show the count rates for different time intervals and binning and were used by Tobias Beuchert from the Remis observatory to do first telemetry studies for MIRAX. The depicted count rates do not include the background yet (see chapter 5) and are therefore estimated too

low. Fig. 4.22 illustrates one 97 min orbit of MIRAX and is binned to one minute intervals. The clearly visible peak in count rates is due to MIRAX passing the Galactic center once every orbit. Fig. 4.23 illustrates one third of a day of MIRAX observations with 5 passages of the Galactic center. The smaller peaks may correspond to the passage of the Southern Galactic plane.

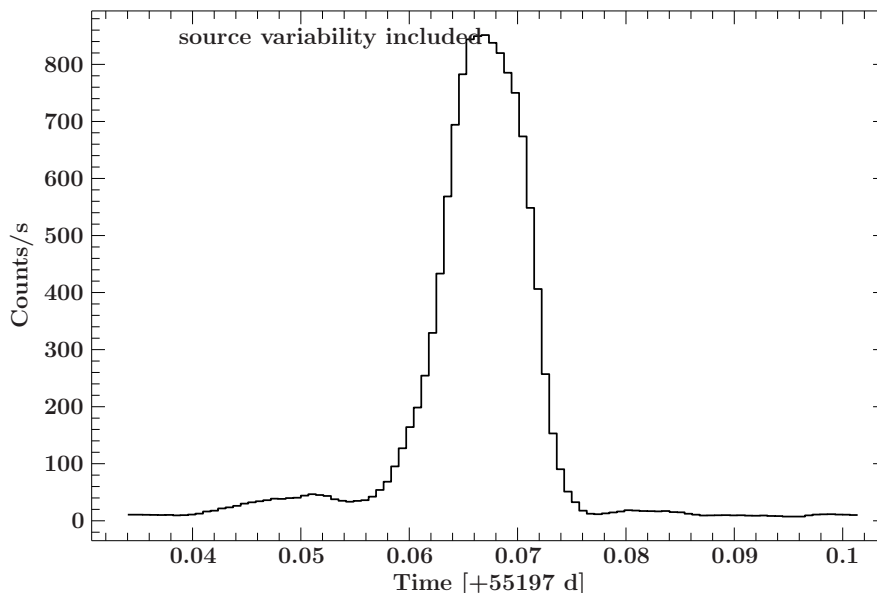


Figure 4.22.: Count rate estimation based on the produced event-files, during one MIRAX orbit of 97 min or 5820 seconds. The peak corresponds to MIRAX passing the Galactic center with its huge amount of sources (credits: T. Beuchert).

In order to get more realistic results, the BAT catalog¹⁵ was used to feed the simulation with input. Fig. 4.24 depicts a pointed observation of the Galactic center with a right ascension of 266° and a declination of -29° . As the reconstructed image shows all kinds of different features in the background, which depend mainly on the mask pattern used, as well as on the detector setup (for example, the gaps influence the image) and the simulated exposure time, the contrast was changed in almost all shown figures to make the bright points of high count rates (i. e. the sources) easier to distinguish.

With an increased exposure, more counts are detected, and hence more sources are visible, as illustrated in Fig. 4.25, which compares an 1000s, a 3000s and a 10000s exposure time around the same region of the Galactic center.

Figure 4.26 identifies exemplarily some of the sources according to their position in the BAT catalog. The center of the shown coordinate grid is not the 0.0/0.0-position as stated, but the pointing direction of the telescope of $RA = 267^\circ$ and $DEC = -28^\circ$. The sources' respective names are labeled around them, and two names indicate that both sources could contribute to the detected flux, since their positions are so close together that they could not be resolved individually.

For evaluation of the source position accuracy, not so crowded regions were chosen, far away from the Galactic center. Fig. 4.27 illustrates MIRAX' orbits, as the light gray lines, in

¹⁵A catalog based on the sources found by BAT/*SWIFT* and generated by C. Grossberger.

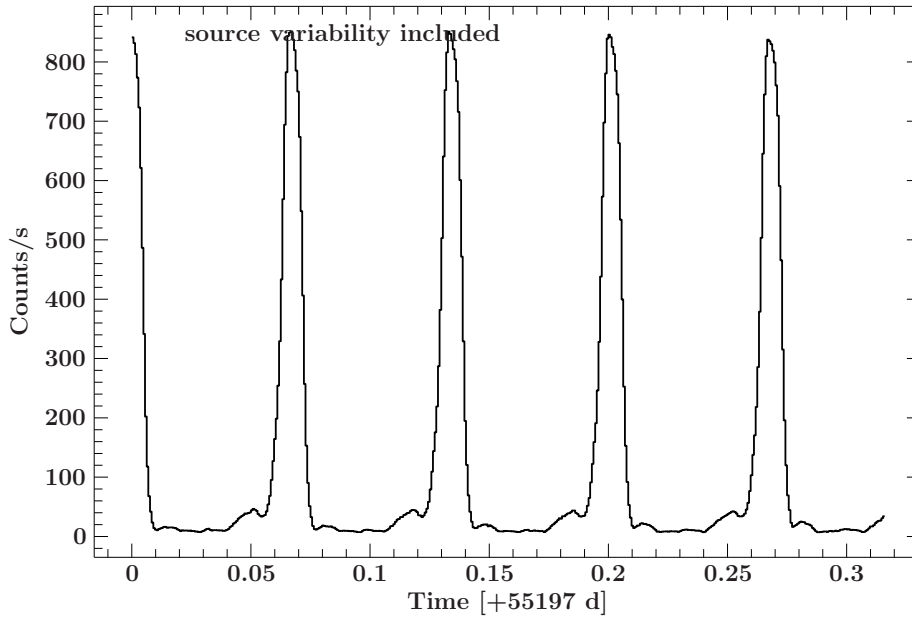


Figure 4.23.: Count rate estimation during one third of a day of MIRAX observations with 5 passages of the Galactic center. The smaller peaks are presumably due to the passage of the Southern Galactic plane (credits: T. Beuchert).

equatorial coordinates and displays the strongest BAT-sources. The Galactic center resides at the lower right part and corresponds to the most populated region. Also the different pointings used in this section are displayed as colored dots. Fig. 4.28 and 4.29 are not within MIRAX’ real orbits and were chosen arbitrarily as regions with few sources. It has to be pointed out that, in general, not all sources lying within the respective simulated FOV are visible in the sky images, which is due to their differences in intensity and due to the low kept reasonable exposure times.

Further, the evaluation of the source position accuracy can not be provided with accurate errors, since the sources’ positions are read directly from the sky pictures via positioning the cursor above them, which can not be too precise. In addition the source’s positions are extended from one to five pixels, where one pixel corresponds to $\theta = 0.049^\circ$ in extension, which is determined by Eq. 2.1.1 as:

$$\theta = \arctan\left(\frac{0.0006 \text{ m}}{0.7 \text{ m}}\right) = 0.049^\circ, \quad (4.11)$$

since for all pictures presented in this section, the first approach for re-pixelization as described in Sec. 4.2 was used. Hence for sources extended over five pixels the position read off the picture can already vary within 0.25° . Nevertheless, one can see a pattern in deviation of the determined positions compared to the real positions, as described in the following.

Table 4.2 illustrates that for sources close the telescope pointing direction, the position given by the reconstructed image is very close to the sources’ real position. Sources with larger off axis angles are determined worse, and those whose two coordinates differ significantly in their off axis values further show large deviations. It can not be excluded that some of the dedicated sources are wrongly assigned, because of the huge amount of sources listed in the catalog.

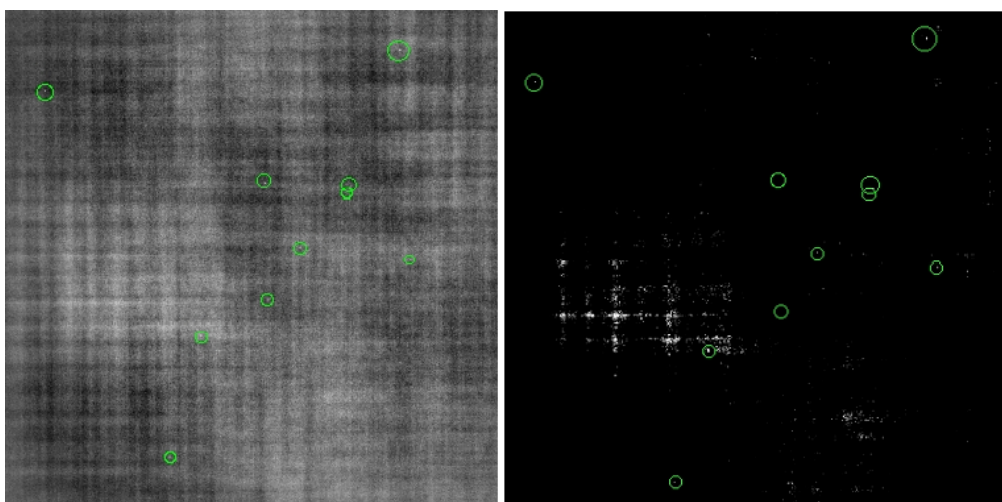


Figure 4.24.: Pointed observation of the Galactic center as given by the BAT catalog, with coordinates of $RA = 266^\circ$ and $DEC = -29^\circ$ and a low exposure of 500 seconds. Both show the same reconstructed sky image, but with changed contrast on the right, in order to make the bright pixels of high count rates easier to distinguish. Only a few sources are found, which is due to the relatively low exposure time and the influence of the very bright sources that are dominating the whole picture.

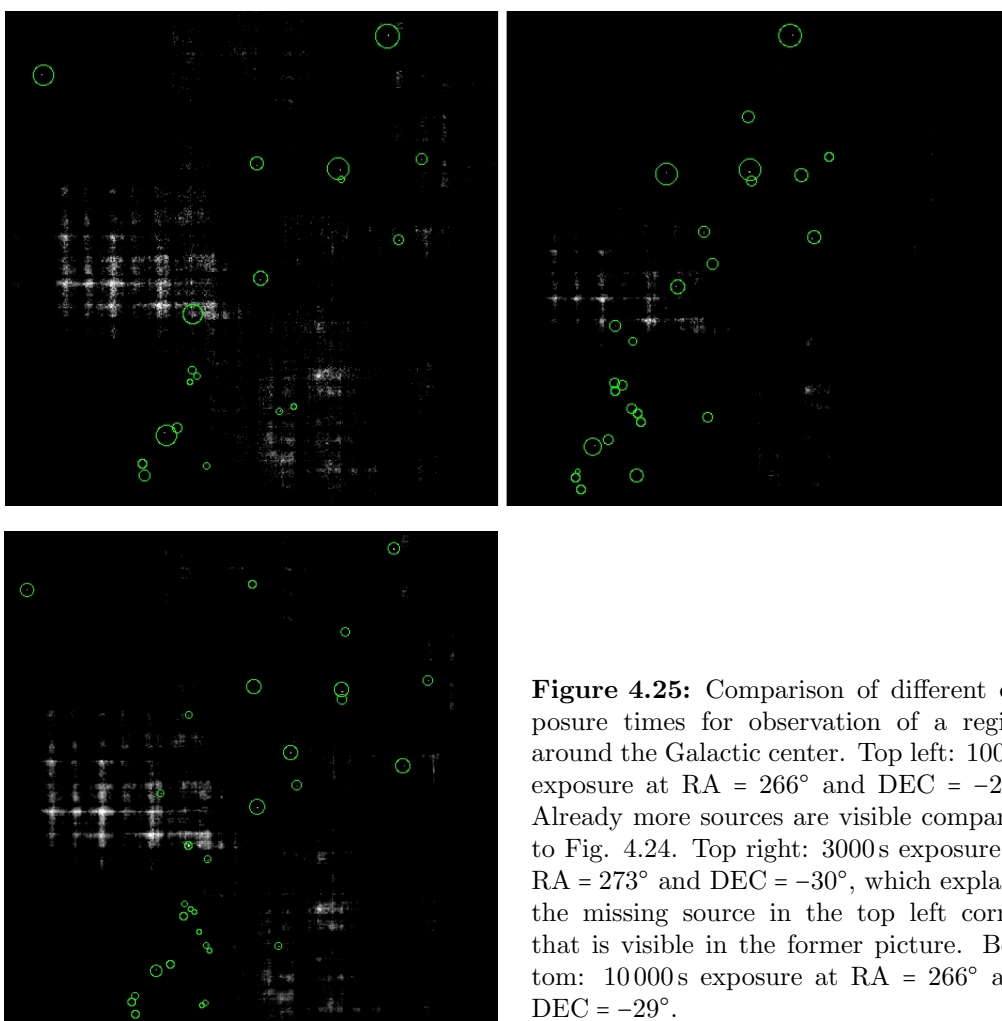


Figure 4.25: Comparison of different exposure times for observation of a region around the Galactic center. Top left: 1000 s exposure at $RA = 266^\circ$ and $DEC = -29^\circ$. Already more sources are visible compared to Fig. 4.24. Top right: 3000 s exposure at $RA = 273^\circ$ and $DEC = -30^\circ$, which explains the missing source in the top left corner that is visible in the former picture. Bottom: 10000 s exposure at $RA = 266^\circ$ and $DEC = -29^\circ$.

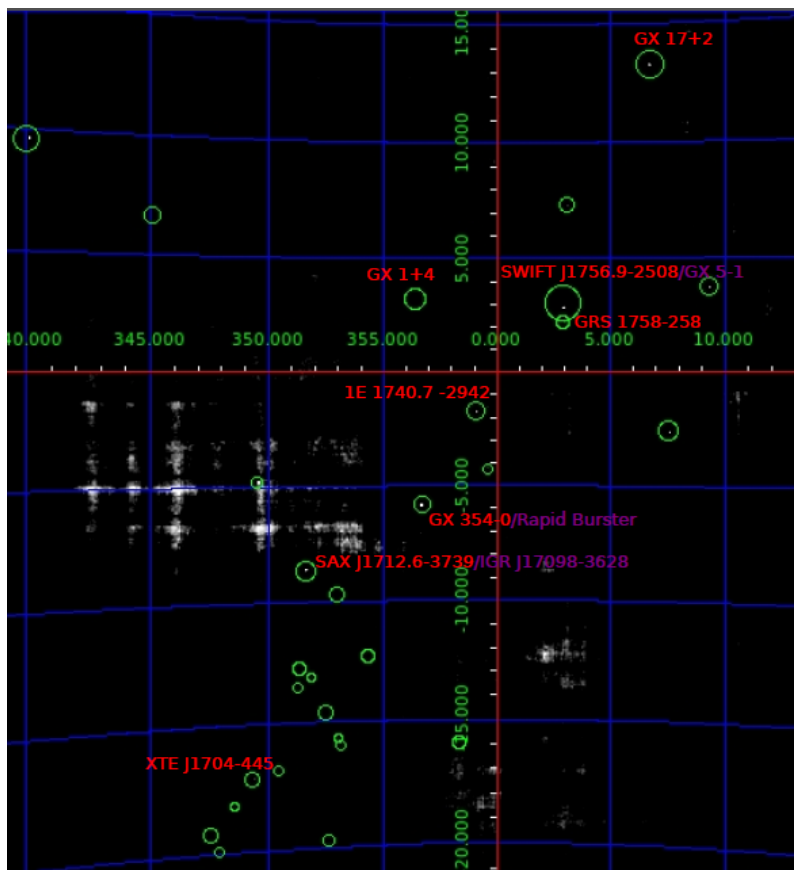


Figure 4.26: Sky image of Galactic center with 8000s exposure at RA = 267° and DEC = -28°. Some of the source positions have been compared to the BAT catalog and their respective names are labeled around them. Sources with two names may have contributions from both of them, since their positions are too close together to be resolved individually. When comparing to the catalog’s positions, it has to be kept in mind that the origin of the illustrated grid corresponds to the pointing direction of the telescope.

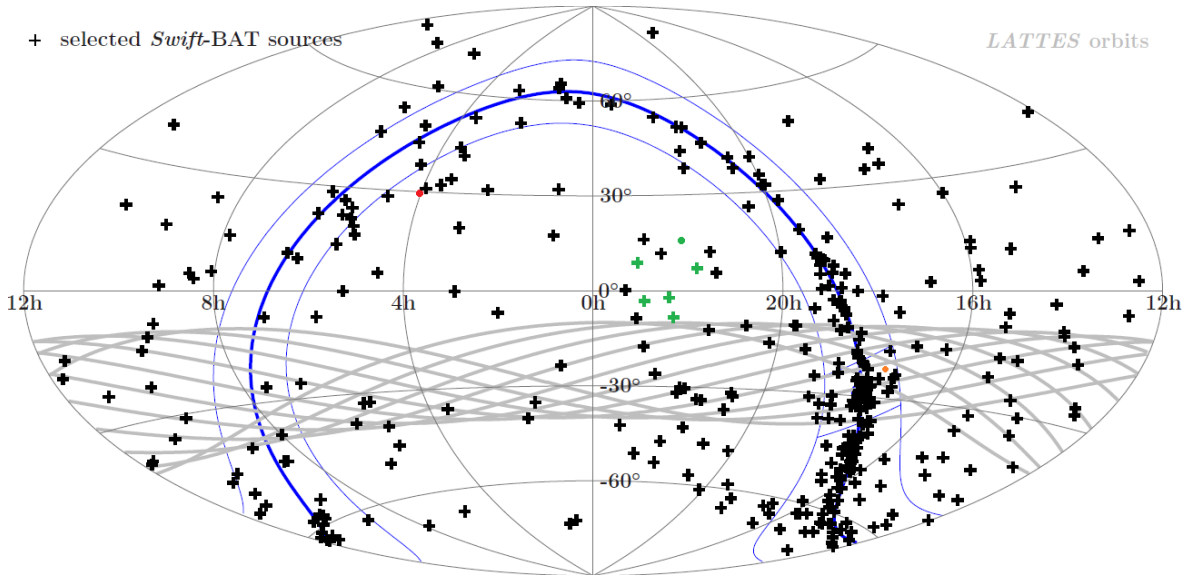


Figure 4.27.: Some of BAT’s strongest sources (black crosses) in equatorial coordinates to get an impression of their distribution along MIRAX’ orbit, which is denoted by the light gray lines. The lower right corner displays the Galactic center and the small orange dot corresponds approximately to the coordinates of the telescope’s pointing direction used for the figures 4.24, 4.25 and 4.26. The green dot at around RA = 340° (or 22.6 h) and DEC = 20° corresponds to the origin used for Fig. 4.28 and the red one around RA = 60° (or 4 h) and DEC = 30° displays the pointing for Fig. 4.29. The green colored crosses symbolize the best guesses for the association with the in Fig. 4.28 identified sources (credits: T. Beuchert).

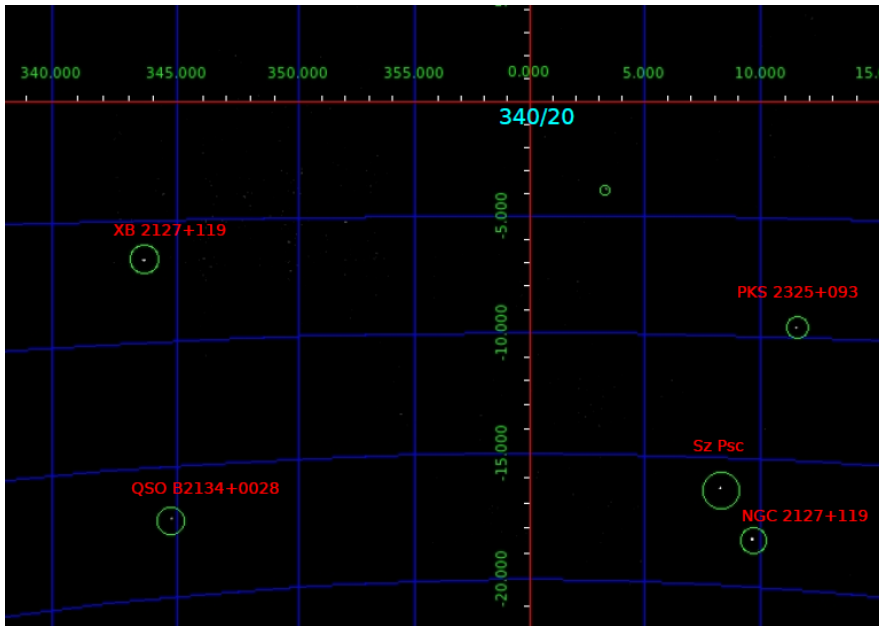


Figure 4.28: 1000 s exposure at RA = 340° and DEC = 20° (green dot in Fig. 4.27). The green crosses in Fig. 4.27 correspond to the best guesses for the association with the shown sources. Their positions are analyzed in Tab. 4.2.

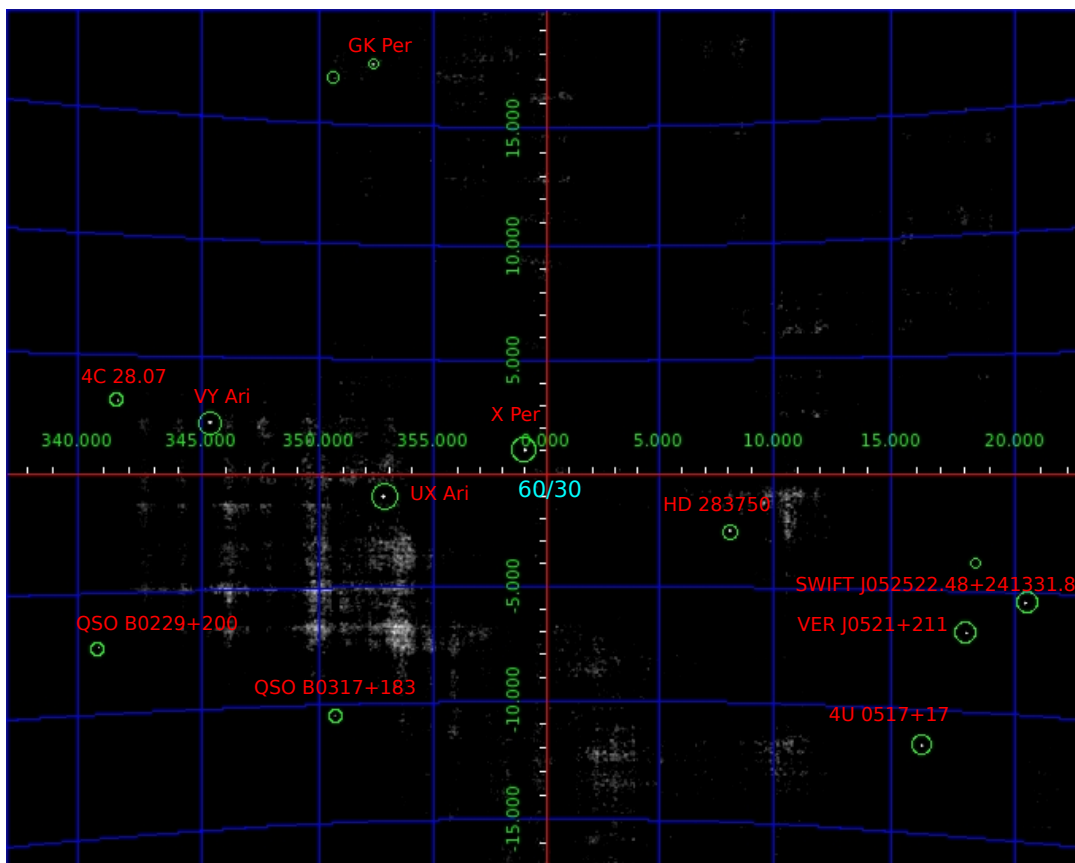


Figure 4.29: 10000 s exposure at RA = 60° and DEC = 30° (red dot in Fig. 4.27). The source positions are analyzed in Tab. 4.2.

Table 4.2.: Top: data corresponding to Fig. 4.28, bottom: values taken from Fig. 4.29. The measured positions in the reconstructed image are given for each source, which are not too accurate as described before (simply the arithmetic mean was used), followed by the catalog position. The last two columns give the off axis angle with respect to the measured position and the angular separation between measured and catalog position. The first three columns give first the RA value and then the DEC coordinate. It can be seen that for larger off axis angles the deviation gets worse and further that for sources with considerably different off axis angles, one coordinate is mostly more off than the other. ‘X Per’ for example is very close to the respective pointing direction and hence its deviation is very small. ‘QSO B0229+200’ has significantly different off axis angles and also shows larger deviations.

source	measured position	catalog position	off axis angle	angular sep.
PKS 2325+093	351.47/10.38	351.89/9.67	11.47/-9.62	0.82
SZ Psc	348.30/3.77	348.35/2.66	8.30/16.23	1.11
NGC 7603	349.57/1.82	349.74/0.24	9.57/-18.18	1.59
XB 2127+119	323.60/13.40	322.50/12.17	-16.40/-6.60	1.63
QSO B2134+0028	324.73/2.97	324.16/0.70	-15.27/-17.03	2.34
SWIFT J052522.0	80.40/24.60	81.34/24.23	20.40/-5.40	0.93
VER J0521+211	78.07/23.26	80.48/21.19	18.07/-6.74	3.04
4U 0517+17	76.23/18.53	77.69/16.50	16.23/-11.47	2.46
HD 283750	68.08/27.49	69.20/27.13	8.08/-2.51	1.06
X Per	59.00/31.03	58.85/31.05	-1.00/1.03	0.13
GK Per	52.32/47.47	52.28/43.90	-7.68/17.47	3.57
UX Ari	52.73/28.98	51.65/28.72	-7.27/-1.02	0.98
VY Ari	45.33/32.21	42.18/31.12	-14.67/2.21	2.89
4C 28.07	41.55/33.02	39.47/28.80	-18.45/3.02	4.58
QSO B0317+183	50.64/19.48	49.97/18.76	-9.38/-10.20	0.96
QSO B0229+200	40.81/22.10	38.20/20.29	-19.19/-7.29	3.03

The mean angular separation between measured and catalog position as listed in Table 4.2 is 1.95° with a standard deviation of 1.19° , which is due to some of the larger off axis angle positions showing a bigger angular separation. The overview given by Table 4.2 only serves for getting a feeling of source recognition and to show that an algorithm is needed to determine the reconstructed positions more accurately and with correct error values. This is part of, what has to be developed next. Additionally a procedure is needed to find the brightest source in a sky image and then remove their complete contribution to the picture, in order to make less bright overshadowed sources also visible (see Cha. 5). Fig. 4.30 shows such a situation, where a too bright source causes a weaker one to vanish. This is the main reason for only finding a few sources even within the highly populated region of the Galactic center as depicted in Fig. 4.26.

It is further possible, as assumed for some sources in Fig. 4.26 that positions too close together may not be resolved and appear to be only one source instead of two or even more. Fig. 4.31 displays such a situation, where for decreasing distance two sources seem to merge and could be falsely identified for being one and the same source.

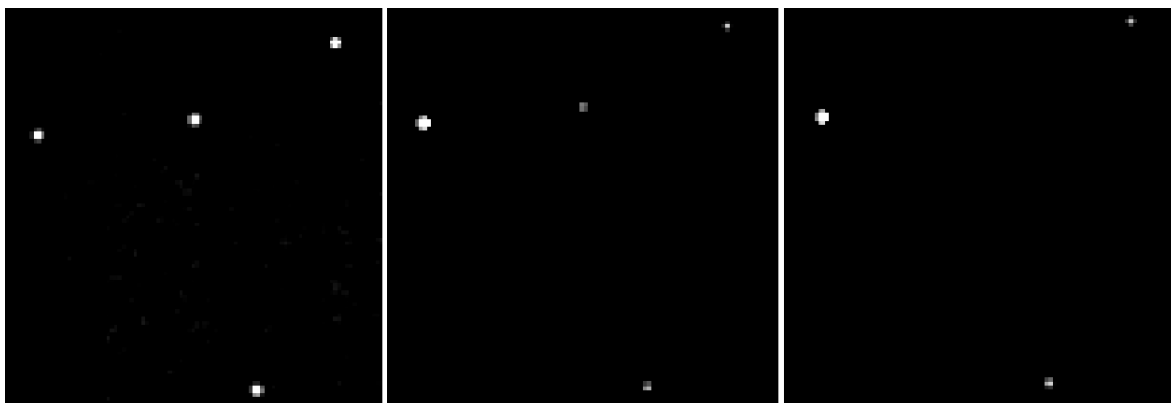


Figure 4.30.: Comparison of different intensities for the same source positions. Left: all four sources have equal intensities with a flux value of $\text{flux} = 2.0 \cdot 10^{-7} \text{ erg}/(\text{s cm}^2)$. Middle: the left sources' flux was increased to $\text{flux} = 9.0 \cdot 10^{-7} \text{ erg}/(\text{s cm}^2)$, and therefore appears brighter, compared to the others. Right: the middle sources' flux was decreased to $\text{flux} = 5.0 \cdot 10^{-8} \text{ erg}/(\text{s cm}^2)$, which caused it to disappear, since a far stronger source is present in the image.

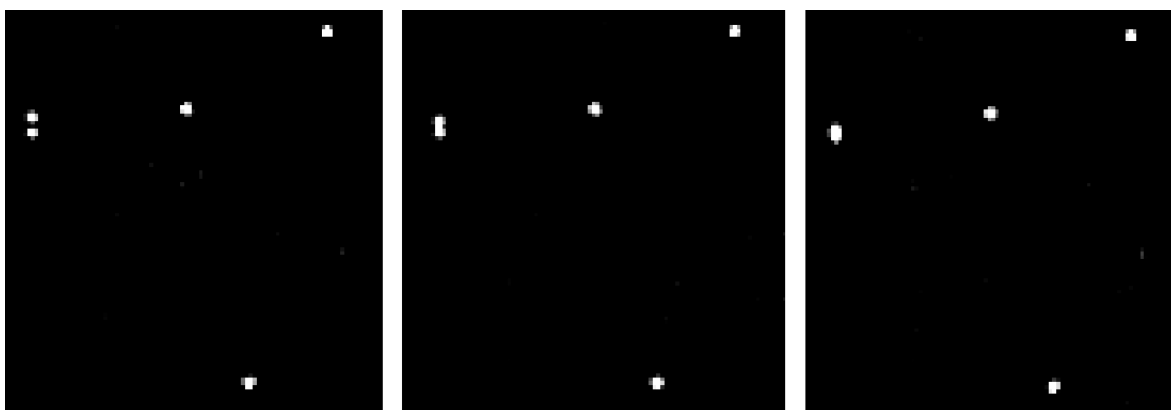


Figure 4.31.: The upper left corner shows in all three images two different sources closely together. Left: the vertical separation of the two sources is 0.2° , which leads to a well distinguishable image. Middle: the separation is decreased to 0.15° and the two sources seem to merge. Right: the distance is further decreased down to 0.1° and the two sources appear as one.

As stated before, the implementation of the Fast Fourier Transform algorithm saves a lot of computation time compared to the direct cross correlation variant. For a ~ 4 MB sized event file, the direct cross correlation needed on average 1 minute and 15 seconds, while the FFT approach only took around 8 seconds, even though the re-pixelization and padding is only implemented in the latter one and needs further processing time. Thus, the reconstruction via FFT is 9 times faster than the former method. It has also been mentioned that, for all the pictures produced in the last chapter, the faster re-pixelization approach with only detector sized pixels has been used, since no deterioration in determining the sources' positions could be found and its save in computation time is also significant.

Chapter 5

Outlook

The main task during this thesis was to understand an existing software package and to obtain the ability to further develop its functionality. During that process, the imaging and detection module have been refined to meet the requirements of the MIRAX HXI. As the main subject of this thesis, most of the work has been done for the image reconstruction, which is now fully operational and allows a first impression of what MIRAX will be able to see. The whole simulation pipeline builds a sound basis for developing a more sophisticated test setup for MIRAX (and other coded mask projects as well).

The future prospects shall be outlined in the following.

More realistic detector setup

As described before, the currently implemented detector setup already models some of MIRAX's characteristics very well, but shall be extended in the future. First of all, the ARF (Sec. 4.1.1) will regard the detector entrance window and the photons absorbed by it and also the RMF has to be modeled in more detail. A variety of effects have to be considered further, such as partial absorption at the detection plane or at transparent mask pixels, which may not be completely transparent at all. The opposite holds too: opaque mask pixels may not be fully blocking and a small amount of radiation may transmit. Further charge cloud splitting may occur at the detection plane, which means one event could be distributed over two or more pixels, and therefore be registered as different events with less intensity each. Also detector inherent parasitics influence the detection process, like for example, dead or hot pixels, which produce no or too much signal, or the dead time during the pixels' read out process, when no photon can be detected at all.

It also has to be decided, where these effects are regarded best, as some of them may be handled within an input function like the ARF or RMF and some may be implemented optimally in one of the modules directly.

Moreover the mask plane may not be fully congruent with the detection plane, thus it has to be rotated slightly above the detector and to get a full impression of MIRAX's FOV, the four sub-detectors have to be combined with their respective tilting, as they are canted away from each other.

Background

The particle induced ever present background also influences the performance of any detector exposed to it in space. MIRAX does have several shielding layers to prevent radiation from entering through the sides, but they cannot be fully impermeable and the detector's entrance

window surely isn't. Therefore the background has to be modeled in detail according to the telescope geometry and setup and to the regarded time interval as well as the attitude. The background count rate comprises different contributions from Earth' atmosphere, solar activity and from space. Thus it varies over time and with changing position and it induces 'false' X-ray events, as their origin are not the desired sources. A realistic simulation of these events is currently carried out by our collaborators at the IAAT and will be included in our simulation pipeline in near future.

Scanning survey

As MIRAX does not do pointed observations, but operates in a scanning survey mode, the slew of the attitude has to be considered at the image reconstruction module. This implies that the registered events contain source positions which are slowly changing over time. Thus the detected shadowgram would look different for the same source and different observation times and could not be resolved with the currently implemented algorithm. The idea is to decompose the survey into different small pointing units, for which the source positions can be reconstructed correctly, and to then add up all the contributions for a whole reconstructed image. Therefore the observed part of the sky has to be the same within the regarded time interval and with respect to a coordinate system, which' origin must not be the optical axis of the telescope.

Comparison to backprojection

The for the slew corrected version of the image reconstruction, will be compared to the completely different approach, of recovering the sources' positions via backprojection. Sebastian Falkner of the Remeis observatory is currently developing the required algorithm. The two reconstruction concepts will be analyzed with respect to their source position accuracy and computational effort. It remains to be seen which one fits the requirements of the MIRAX-HXI best.

Source position accuracy

In order to determine the sources' position more accurately, an algorithm is needed to find the exact reconstructed position in the sky image and to assign a proper error value to it. The current method simply places the cursor above the respective position which can obviously not be too accurate, but sufficient for testing purposes and for showing the behavior described by table 4.2.

Iterative Removal Of Sources (IROS)

As described in Sec. 4.3, bright sources may completely be overshadowed by weaker ones. It is therefore essential to develop an algorithm, which identifies the strongest source in the picture and removes their contribution fully. The remaining distribution will then again include a brightest, but less intense source that can again be identified and removed. In this way the weaker sources may subsequently be found. A similar approach may further be used to clean the image from already well known sources, such that the search will continue only for yet undiscovered new source positions.

Appendix A

Overview of used functions

In the following an overview of some of the functions used to write the coded mask simulation modules in the language C, is given. The first column corresponds to the data type of the return value, the second to the functions' name and the third one to its arguments. The last column explains the functions' purpose.

int ('3': photon outside FOV, '0': photon inside)	<code>check_fov</code>	vector of photon direction; vector of telescope pointing; minimum cos value for photons inside FOV	checks, whether photon is inside FOV
int ('1': valid photon, '0': photon hits the walls)	<code>getImpactPos</code>	structure to save photon's position; vector of photon direction; mask data and telescope setup; status parameter	assigns photon with pixel in mask plane, it passes; determines impact position in detection plane; discards photons that would hit the walls
int ('1': valid pixel, '0': invalid pixel)	<code>getSquarePixel</code>	pointer to structure SquarePixels, which gives the telescope setup; structure of type Point2d, which gives the photon's position in meters; integer-type pointers, in which the pixel position is stored	determines pixel position an incoming photon hits at the detection plane and discards those photons that would meet a gap
ReconArray* (pointer to type for storing all necessary data for the G array)	<code>getReconArray</code>	pointer to mask data; pointer to detector setup; status parameter	creates reconstruction array from mask; checks, whether pixel size differs for detector and mask and re-pixels accordingly

ReadEvent* (pointer to type for storing all necessary data for the E array)	getEventArray	pointer to mask data; pointer to detector setup; status parameter	creates empty event array object to store all detected events by summing up each pix- els' counts
fftw_complex* (pointer to FFTW inherent data type)	FFTOfArray_1d	pointer to array stored in row major order; length and width of input array; type of FT, where '-1' is forward, '1' is backwards	computes the FT of the input array with its real and imaginary part accessible, like de- scribed in Sec. 4.1.4, p.42)
fftw_complex*	FFTOfArray	pointer to array which already is of type fftw_complex; rest, same as above	as above, needed for backwards transforms of arrays that already are of FFTW's type
void	testFitsImage1d	pointer to row major order array; filename of output FITS-file; array dimensions; status parameter	gives a FITS image of the 1d-input array; used to test Fourier transformed arrays

Appendix B

Example code

Listing B.1: Function `getSquarePixel` which determines the pixel coordinates hit by a photon and discards photons that would meet a gap.

```
int getSquarePixel(SquarePixels* sp, struct Point2d position,
                  int* x, int* y)
{
    if(sp->DCU_length!=0.){

        //position.x and .y is with reference to a corner of the detector [m]
        //first: check, whether impact position lies within one of the DCU's
        //second: determine position in terms of pixels
        //third: ensure that there will be no error with the type-cast
        //(int rounds to lower value)

        double DCA_length=(2.*sp->DCU_length)+sp->DCU_gap;
        double DCA=DCA_length+sp->DCA_gap;

        int ratio_x=(int)((position.x)/DCA);
        int ratio_y=(int)((position.y)/DCA);

        if(position.x < (ratio_x*DCA+sp->DCU_length))
        {*x = (int)(position.x/sp->xpixelwidth +1.)-1;}
        else{if(position.x > (ratio_x*DCA+sp->DCU_length+sp->DCU_gap)
                && position.x < (ratio_x*DCA+DCA_length))
            {*x = (int)(position.x/sp->xpixelwidth +1.)-1;}
            else{return(0);}
        }

        if(position.y < (ratio_y*DCA+sp->DCU_length))
        {*y = (int)(position.y/sp->ypixelwidth +1.)-1;}
        else{if(position.y > (ratio_y*DCA+sp->DCU_length+sp->DCU_gap)
                && position.y < (ratio_y*DCA+DCA_length))
            {*y = (int)(position.y/sp->ypixelwidth +1.)-1;}
            else{return(0);}
        }

    }else{
        *x = (int)(position.x/sp->xpixelwidth +1.)-1;
        *y = (int)(position.y/sp->ypixelwidth +1.)-1;
    }
}
```

```

if ((*x>=0) && (*x<sp->xwidth) && (*y>=0) && (*y<sp->ywidth)) {
    return (1); // Valid pixel.
} else {
    return (0); // Invalid pixel.
}
}
}

```

Listing B.2: Function `getReconArray` that creates the reconstruction array from the mask pattern and decides whether pixelsize of the mask differs from that of the detector and if so, re-pixels to the given value via the chosen approach.

```

ReconArray* getReconArray(const CodedMask* const mask,
                          SquarePixels* detector_pixels, int* const status)
{
    ReconArray* recon=NULL;
    int x,y; //count for memory allocation
    int xcount, ycount; //count for getting Rmap: same pix-size
    int xpixelcount=0, ypixelcount=0; //count for getting Rmap: diff pix-size
    double leftsmall=0., leftbig=0.; //left border small(detector) & big(mask) pix
    double topsmall=0., topbig=0.; //top border small(detector) & big(mask) pix
    double w, h; //width/height of part of small pix inside
                    //current big pix

    //Get empty reconstruction array-object
    recon=newReconArray(status);
    if (EXIT_SUCCESS!=*status) return(recon);

    //in order to get same pixelsize as detector:
    //[[naxis1 in maskpixels]*[pixelsize of mask]->absolut size of mask in meters
    //divided by [detector pixelsize]
    recon->naxis1=2*(mask->naxis1*mask->cdelt1/detector_pixels->xpixelwidth);
    recon->naxis2=2*(mask->naxis2*mask->cdelt2/detector_pixels->ypixelwidth);

    //memory-allocation for Rmap
    recon->Rmap=(double**) malloc(recon->naxis1*sizeof(double*));
    if(NULL!=recon->Rmap){
        for(x=0; x < recon->naxis1; x++){
            recon->Rmap[x]=(double*) malloc(recon->naxis2*sizeof(double));
            if(NULL==recon->Rmap[x]) {
                *status=EXIT_FAILURE;
                HD_ERROR_THROW("Error: could not allocate memory to store the "
                               "ReconstructionArray!\n", *status);
                return(recon);
            }
            //Clear the pixels
            for(y=0; y < recon->naxis2; y++){
                recon->Rmap[x][y]=0.;
            }
        }
        if (EXIT_SUCCESS!=*status) return(recon);
    } else {
        *status=EXIT_FAILURE;
        HD_ERROR_THROW("Error: could not allocate memory to store the "
                       "ReconstructionArray!\n", *status);
        return(recon);
    } //end of memory-allocation
}

```

B. Example code

```
recon->open_fraction = mask->transparency;

// decide whether pixelsize is different for det and mask
if(mask->cdelt1 == detector_pixels->xpixelwidth){

//Scanning over all mask-elements
for(xcount=0; xcount < mask->naxis1; xcount++){
  for(ycount=0; ycount < mask->naxis2; ycount++){
    if(mask->map[xcount][ycount]==1){
      recon->Rmap[xcount][ycount]=1.;
    }else if(mask->map[xcount][ycount]==0){
      recon->Rmap[xcount][ycount]=
        (recon->open_fraction)/(recon->open_fraction - 1.);
    }else{
      *status=EXIT_FAILURE;
      HD_ERROR_THROW("Error while scanning mask-elements!\n", *status);
    }
  }
}
} //End of scanning over mask-elements
} //End equal pixelsize

else{//begin diff pixelsize
  //initialize all to max neg value (depending on DF)
  for(xcount=0; xcount < (recon->naxis1/2); xcount++){
    for(ycount=0; ycount < (recon->naxis2/2); ycount++){
      recon->Rmap[xcount][ycount]=(recon->open_fraction)/
        (recon->open_fraction - 1.);
    }
  }
}

//distance between max neg value and 1 (which has to be distributed
// accordingly to new smaller pixels)
double diff=1.-(recon->open_fraction)/(recon->open_fraction - 1.);

//Scanning over all mask-elements to get Rmap with same pix-size as detector
for(ycount=0; ycount<mask->naxis2;ycount++){
  for(xcount=0; xcount<mask->naxis1;xcount++){

    topbig=ycount*mask->cdelt2; //top of current big pixel
    ypixelcount=topbig/detector_pixels->ypixelwidth;
    //count for small pixel (new pixels in Rmap)
    //current y-pix: top border of big pix/width of one small pix
    //->determines 1st small in curent big

    do{//as long as in current big pixel in y-direction
      topsmall=ypixelcount*detector_pixels->ypixelwidth;
      //top border of small pix:
      //current small pix*width of one
      if(topsmall<topbig){//1st small in current big starts
        //with part of it in former pix
        h=detector_pixels->ypixelwidth-(topbig-topsmall);
        //height that lies in current big:
        //smallwidth-(part of height that lies in former big pix)
      }else{
        if((topsmall+detector_pixels->ypixelwidth) <= (topbig+mask->cdelt2)){
          //small pix lies completely in big

```

```

        h=detector_pixels->ypixelwidth;
    }else{//small pix is at border of curent big->part of it in next big
        h=topbig+mask->cdelt2-topsmall;//part of height in current big:
        //top of next big - top of current small
    }
}

leftbig=xcount*mask->cdelt1;
xpixelcount=leftbig/detector_pixels->xpixelwidth;
do{//as long as in current big pixel in x-direction
    leftsmall=xpixelcount*detector_pixels->xpixelwidth;
    if(leftsmall<leftbig){
        w=detector_pixels->xpixelwidth-(leftbig-leftsmall);
    }else{
        if((leftsmall+detector_pixels->xpixelwidth) <= (leftbig+mask->cdelt1)){
            w=detector_pixels->xpixelwidth;
        }else{
            w=leftbig+mask->cdelt1-leftsmall;
        }
    }
}
if(mask->map[xcount][ycount]==1){//all small transparent pixel-areas
    //contribute as percentage
    recon->Rmap[xpixelcount][ypixelcount]+{//one small pix can have
        //contributions from parts lying in diff big pix
        h*w/(detector_pixels->xpixelwidth*detector_pixels->ypixelwidth)*diff;
        //percentage of area with respect to area of whole small pix
    }//multiplied with max diff occuring in Rmap values, in order
    //to distribute them accordingly
    xpixelcount++;
}while(leftsmall+detector_pixels->xpixelwidth <= (leftbig+mask->cdelt1));
    //end current big pixel x-direction

    ypixelcount++;
}while(topsmall+detector_pixels->ypixelwidth <= (topbig+mask->cdelt2));
    //end current big pixel y-direction
}
}

return(recon);
}
}

```

Listing B.3: Function `FFTOfArray_1d` transforms the input array given in 1d-row major order in Fourier space and returns the transformed array with its real and imaginary part.

```

fftw_complex* FFTOfArray_1d(double* Image1d, int ImageSize1, int ImageSize2, int type)
{
    fftw_complex* Input;
    fftw_complex* Output;
    fftw_plan plan;
    int ii, jj;

    //Memory-Allocation
    Input=(fftw_complex*) fftw_malloc(sizeof(fftw_complex)*ImageSize1*ImageSize2);
    Output=(fftw_complex*) fftw_malloc(sizeof(fftw_complex)*ImageSize1*ImageSize2);

    //Copy Image1d of type double to Input-Array of type fftw_complex

```

```
for(ii=0; ii<ImageSize1; ii++){
    for(jj=0; jj<ImageSize2; jj++){
        Input[ii+ImageSize1*jj][0]=Image1d[ii+ImageSize1*jj];
        Input[ii+ImageSize1*jj][1]=0.;
    }
}

plan=fftw_plan_dft_2d(ImageSize1, ImageSize2, Input, Output, type, FFTW_ESTIMATE);

fftw_execute(plan);

fftw_destroy_plan(plan);
fftw_free(Input);

return(Output);
}
```

Acknowledgments

I am very thankful for having had the possibility to write this thesis at the Dr. Karl Remeis Sternwarte in Bamberg. All the people working there welcomed me with open arms and provided such a friendly atmosphere and were always being very supportive for all kinds of problems. I especially want to thank Christoph Grossberger, who helped me a lot getting started with the reconstruction module and of course my advisor Christian Schmid, who endured all my questions and always answered them patiently (and will have to do so in the future). He helped me indispensably to orient myself in the completely new field of programming. Also Fritz Schwarm and Thomas Dauser were great help with the observatories computer system. Tobias Beuchert always has a tip to all my questions and was also great support for parts of this thesis.

Most and deeply, I have to thank my supervisor Jörn Wilms, for reminding me, why I even studied physics in the first place and for giving me the possibility of working in a completely new field, without bringing any specific prior knowledge. He woke up my fascination again and pointed me in the right future direction.

Eventually I want to thank my father for all his great support and my significant other for all his infinite patience with my mood and my very best friend for all her cheering me up.

List of Figures

1.1. Overview of X-ray sources	6
1.2. The Sun's hot corona in X-rays	7
1.3. CXB diffuse all-sky maps and individual resolved sources	9
1.4. Absorption of electromagnetic radiation by Earth's atmosphere	10
1.5. Wolter type I configuration	12
2.1. Detection principle of a coded mask system	14
2.2. Illustration of FCFOV and PCFOV	15
2.3. Example of a SPSF with side-lobes that appear as artifacts	16
2.4. Mask patterns	18
2.5. Attenuation length for X-rays in a CCD and its pixels structure	20
2.6. Correlation vs. convolution	25
2.7. The BAT coded mask telescope and <i>ProtoEXIST</i> balloon gondola	26
3.1. Sensitivity map for 1 year of scanning operation mode of MIRAX	28
3.2. The <i>Lattes</i> spacecraft and its characteristics	28
3.3. Structure of the HXI and of its shielding layers	30
3.4. Components of a DM	31
4.1. Software simulation pipeline	33
4.2. ARF as used for MIRAX	34
4.3. Schematic of photon generation module	34
4.4. Schematic of imaging module	35
4.5. Maximum allowed angle for incoming photons	36
4.6. Randomly distributed impact positions within one mask pixel	37
4.7. Schematic of detection module	38
4.8. RMF as used for MIRAX	38
4.9. Schematic of reconstruction module	39
4.10. Test of intensity distribution	42
4.11. Examples of different stages during reconstruction: E	43
4.12. Examples of different stages during reconstruction: G	43
4.13. Examples of different stages during reconstruction: sources	44
4.14. Schematic of gaps in detection plane	45
4.15. Gaps in event-file as produced by the detection module	45
4.16. Small gaps between two DCU's	46
4.17. Schematic of padding of E and G	46
4.18. Padding of the real arrays	47
4.19. Schematic of mask pattern re-pixeled to detector size pixels	48
4.20. Re-pixeled mask pattern to the size of one detector pixel	49
4.22. Count rate estimation during one MIRAX orbit	51
4.23. Count rate estimation during one day of MIRAX observations	52
4.24. Reconstructed image of Galactic center with low exposure and changed contrast	53

4.25. Comparison of different exposure times for observation of Galactic center . . .	53
4.26. Identified BAT-sources at Galactic center	54
4.27. Selection of BAT sources and illustration of MIRAX' orbit	54
4.28. Example 1 for analyzing the source position accuracy	55
4.29. Example 2 for analyzing the source position accuracy	55
4.30. Comparison of sources with different intensities	57
4.31. Illustration of two sources close together	57

List of Tables

2.1. Maths of convolution and correlation	24
3.1. Overview of MIRAX's science objectives	29
4.1. Arbitrary chosen source positions for testing	44
4.2. Comparison of source position accuracy	56

References

- Allen B., Hong J., Grindlay J., et al., 2010, Proceedings of SPIE 7732
- Arnaud K.A., Smith R.K., 2011, Data reduction and calibration. In: Arnaud K.A., Smith R.K., Siemiginowska A. (eds.) Handbook of X-ray Astronomy. Cambridge University Press
- Ballesteros F.J., Sanchez F., Reglero V., et al., 1997, In: Proceedings of the 2nd INTEGRAL Workshop, 16-20 September 1996.
- Barrett H.H., DeMeester G.D., 1974, Appl. Opt. 13, 1100
- Barthelmy S.D., Barbier L.M., Cummings J.R., Fenimore E.E., 2005, Space Sci. Rev. 120, 143
- Bhardwaj A., Elsner R.F., Randall G.G., Cravens T.E., 2007, Planet. Space Sci. 55, 1135
- Boyle W.S., Smith G.E., 1970, Bell Sys. Tech J. 49, 587
- Busboom A., Elders-Boll H., Schotten H.D., 1998, Exp. Astron. 8, 97
- Caroli E., Stephen J.B., Di Cocco G., et al., 1987, Space Sci. Rev. 45, 349
- Castro M., Braga J., D'Amico F., et al., 2012, Proc. of Science 143
- Charles P.A., Seward D.S., 1995, Exploring the X-ray Universe, Cambridge University Press
- Cohen-Tannoudji C., Diu B., Laloe F., 2007, Quantenmechanik, de Gruyter, Berlin
- Cameron F., Neuhäser R., Kaas A.A., 1998, Messenger 94, 28
- Cooley J.W., Tukey J.W., 1965, Math. Comp. 19, 297
- Demtröder W., 2005, Experimentalphysik 3, Springer, Berlin, Heidelberg
- Demtröder W., 2006, Experimentalphysik 2, Springer, Berlin, Heidelberg
- Edgar R.J., 2011, Detectors. In: Arnaud K.A., Smith R.K., Siemiginowska A. (eds.) Handbook of X-ray Astronomy. Cambridge University Press
- Einstein A., 1905, Ann. Phys. 17, 132
- Fenimore E.E., 1980, Appl. Opt. 19, 2465
- Fenimore E.E., Cannon T.M., 1978, Appl. Opt. 17, 337
- Fenimore E.E., Cannon T.M., 1981, Appl. Opt. 20, 1858
- Fürst F., Wilms J., Rothschild R.E., et al., 2009, Earth Planet. Sci. Lett. 281, 125
- Garson A., Krawczynski H., Weidenspointner G., et al., 2006, In: Proc. SPIE 6319, Hard X-Ray and Gamma-Ray Detector Physics and Penetrating Radiation Systems VIII.
- Giacconi R., Gursky H., Paolini F.R., Rossi B.B., 1962, PhRvL 9, 439
- Giacconi R., Gursky H., Vanspeyck L.P., 1968, ARA&A 6, 373
- Giacconi R., Zirm A., Wang J., et al., 2002, ApJS 139, 369
- Giovannelli F., Sabau-Graziati L., 1993, In: Frontier Objects in Astrophysics and Particle Physics, Vulcano Workshop 2008.
- Giovannelli F., Sabau-Graziati L., 2004, Space Sci. Rev. 112, 1
- Golay M.J.E., 1971, J. Opt. Soc. Am. A 61, 272
- Goldwurm A., David P., Foschini L., et al., 2003, A&A 411, 223
- Goldwurm A., Goldoni P., Gros A., et al., 2001, In: Exploring the gamma-ray universe. Proceedings of the Fourth INTEGRAL Workshop.
- Gottesman S.R., Fenimore E.E., 1989, Appl. Opt. 28, 4344
- Grant C.E., 2011, Charge-coupled devices. In: Arnaud K.A., Smith R.K., Siemiginowska A. (eds.) Handbook of X-ray Astronomy. Cambridge University Press
- Grindlay J., 2011, The Hard X-ray Imager for MIRA-X, NASA Proposal Number 08-EXPMO11-0017
- Groeneveld H.A., 1999, Ph.D. thesis, Eberhard-Karls-Universität Tübingen
- Grupen C., 2005, Astroparticle Physics, Springer
- Güdel M., Naze Y., 2009, Astron. Astrophys. Rev. 17, 309
- Gunson J., Polychronopoulos B., 1976, MNRAS 177, 485
- Hasinger G., Burg R., Giacconi R., et al., 1998, A&A 329, 482
- Hong J., Grindlay J., Allen B., et al., 2010, In: SPIE Conf. "Astronomical Telescopes and Instrumentation 2010", California.
- in't Zand J., 1992, Ph.D. thesis, SRON Netherlands Institute for Space Research
- Karttunen H., Kröger P., Oja H., et al., 2000, Fundamental Astronomy, Springer
- Krimm H., 2003, Am. Astr. Soc. 35, 623

- Kutner M.L., 2003, *Astronomy*, Cambridge University Press
- Leverington D., 2000, *New Cosmic Horizons*, Cambridge University Press
- Markwardt C., Gehrels N., 2004, *Am. Phys. Soc.*
- Mertz L., Young N.O., 1961, In: *Optical Instruments and Techniques*, K. J. Habell. London: Chapman and Hall Ltd, p. 305
- Mewe R., van Paradijs J., Bleeker J.A.M., 1999, *X-Ray Spectroscopy in Astrophysics*, Springer
- Nolting W., 2004, *Grundkurs Theoretische Physik* 5,1, Springer
- Planck M., 1901, *Ann. Phys.* 309, 553
- Ramsey B.D., 2001, In: *Nuclear Science Symposium Conference Record, 2001 IEEE*.
- Rana V.R., Cook w.R., Harrison F.A., 2009, In: *Proc. SPIE 7435, UV, X-Ray, and Gamma-Ray Space Instrumentation for Astronomy XVI*, Vol. 7435.
- Schmid C., 2008, *Friedrich-Alexander-Universität Erlangen-Nürnberg, diploma thesis*
- Schmid C., 2012, *Ph.D. thesis, Friedrich-Alexander-Universität Erlangen-Nürnberg*
- Schwartz D.A., 2011, *Optics*. In: Arnaud K.A., Smith R.K., Siemiginowska A. (eds.) *Handbook of X-ray Astronomy*. Cambridge University Press
- Shin J., Sakurai T., 2003, *J. Korean Astron. Soc.* 36, 117
- Skinner G.K., 2003, In: *Proceedings of the 22nd Moriond Astrophysics Meeting "The Gamma-Ray Universe"*.
- Skinner G.K., Nottingham M.R., 1993, *Nucl. Instrum. Methods Phys. Res., Sect. A* 333, 540
- Wien W., 1896, *Ann. Phys.* 294, 662
- Willingale R., 1981, *MNRAS* 194, 359
- Winkler C., Diehl R., Ubertini P., Wilms J., 2011, *Space Sci. Rev.* 161, 149
- Wolter H., 1952, *Ann. Phys.* 445, 94
- Worsley M.A., Fabian, A. C. and Bauer F.E., Alexander D.M., et al., 2005, *MNRAS* 357, 1281

Declaration

Hiermit erkläre ich, dass ich die Arbeit selbstständig angefertigt und keine anderen als die angegebenen Hilfsmittel verwendet habe.

Bamberg, 11.07.2013

Mirjam Oertel